TUM School of Life Sciences

Molecular characteristics and treatment strategies for neuroendocrine tumors

Sebastian Gulde

Vollständiger Abdruck der von der TUM School of Life Sciences der Technischen Universität München zur Erlangung des akademischen Grades eines Doktors der Naturwissenschaften genehmigten Dissertation.

Vorsitzende:		Prof. Dr. Angelika Schnieke
Prüfende/-r der Dissertation:	1.	Prof. Dr. Gabriele Multhoff
	2.	apl. Prof. Dr. Natalia S. Pellegata
	3.	Prof. Dr. Martin Fassnacht

Die Dissertation wurde am 23.08.2021 bei der Technischen Universität München eingereicht und durch die TUM School of Life Sciences am 13.12.2021 angenommen.

Abstract

Pheochromocytomas (PCCs) and paragangliomas (PGLs), together PPGLs, as well as pancreatic neuroendocrine tumors (pNETs), arise from neuroendocrine cells. They share similar molecular pathogenesis and treatment limitations. Indeed, for both PPGLs and pNETs, the only curative treatment is the surgical removal of the tumor, and inoperable cases due to size, location, or metastases have a poor prognosis. We aimed to find novel treatment strategies for both tumor entities and further characterize the molecular features of PPGLs.

Investigating the molecular characteristics of PPGLs and pNETs, we found that the PI3K/AKT and the CDK4/6 pathways are dysregulated in both tumor types and could be used as therapeutic targets. Therefore, we treated PPGL and pNET cells grown as 2D or 3D cultures with BKM120, a PI3K inhibitor, and LEE011, a CDK4/6 inhibitor. We saw a good response of both PPGL and pNET cells upon treatment with these drugs. Furthermore, we could show a stronger anti-tumor effect upon treatment with the combination of BKM120 and LEE011 compared with the single drug treatments. Altogether, our treatment approach was highly effective at reducing cell growth and inducing apoptosis in both PPGL and pNET cell lines and primary rat/human tumor cells. Furthermore, in PPGL cells we could show the inhibition of migration and invasion, especially after treatment with the drug combination. Importantly, an *in vivo* study showed the great potential of our strategy for the treatment of PPGLs by allowing us to drastically reduce the concentrations of BKM120 and LEE011 administered in combination and still improving anti-tumor effects when compared to the single drugs.

The MENX rat model develops multiple NETs, including PCCs and PGLs. Analyzing the expression profile of PCCs and PGLs that developed in the same animals enabled us to compare these two tumor types directly. Additionally, we compared the rat dataset with a human PPGL dataset. Our analysis revealed that PCCs and PGLs in rats share common features with their human counterparts and that PGLs have a signature compatible with a more aggressive nature. This gene expression data can be of great importance for understanding the genes leading to aggressive tumors and identifying future therapeutic strategies.

Overall, we identified a novel and effective treatment strategy for PPGLs and pNETs by combining PI3K and CDK4/6 inhibition. Furthermore, we showed that PGLs in humans and MENX rats express markers of aggressiveness, which helps to improve our understanding of tumor progression.

Zusammenfassung

Sowohl Phäochromozytome (PCCs) und Paragangliome (PGLs), gemeinsam als PPGLs bezeichnet, sowie pankreatische neuroendokrine Tumore (pNETs) entstehen aus neuroendokrinen Zellen. Sie ähneln sich in ihrem molekularen Ursprung und der Tatsache, dass Behandlungsmöglichkeiten stark eingeschränkt sind. Die chirurgische Entfernung des Tumors ist sowohl für PPGLs als auch für pNETs die einzige kurative Behandlung und inoperable Fälle haben aufgrund von Größe, Lage oder metastatischem Status eine schlechte Prognose. Unser Ziel war es neue Behandlungsstrategien für beide Tumorentitäten zu finden und die molekularen Eigenschaften von PPGLs weiter zu charakterisieren.

Bei der Untersuchung der molekularen Eigenschaften von PPGLs und pNETs stellten wir fest, dass die PI3K/AKT- und CDK4/6-Signalwege in beiden Tumorarten fehlreguliert sind und als therapeutische Ziele verwendet werden können. Daher behandelten wir PPGL- und pNET-Zellen in 2D- und 3D-Systemen mit BKM120, einem PI3K-Inhibitor und LEE011, einem CDK4/6-Inhibitor. Sowohl PPGL also auch pNET Zellen haben auf die Behandlung mit diesen Medikamenten sehr gut angesprochen. Darüber hinaus konnten wir zeigen, dass eine Behandlung mit der Kombination von BKM120 und LEE011 einen verstärkten anti-tumoralen Effekt zeigt im Vergleich zu den Einzelbehandlungen. Unser Behandlungsansatz zeigte eine hohe Wirksamkeit und konnte sowohl das Zellwachstum reduzieren als auch den Zelltod einleiten. Diese Effekte konnten wir in PPGL und pNET Zelllinien sowie in primären Zellen von Ratten und Patienten nachweisen. Zusätzlich zeigte die Behandlung von PPGL Zelllinien mit BKM120 und LEE011 und insbesondere mit einer Kombination aus beiden Wirkstoffen auch eine Hemmung der Migration und Invasion. Mithilfe einer *in vivo* Studie konnten wir zudem nachweisen, dass unsere Strategie zur Behandlung von PPGLs ein großes klinisches Potential hat, indem wir die Konzentrationen von BKM120 und LEE011, die in Kombination verabreicht wurden, drastisch reduzieren konnten bei gleichzeitiger Verbesserung der anti-tumoralen Wirkung im Vergleich zu den Einzelwirkstoffen.

Ratten des MENX-Modells entwickeln mehrere NETs, einschließlich PCCs und PGLs. Die Analyse des Genexpressionsprofils von PCCs und PGLs, die sich in denselben Tieren entwickelten, ermöglichte es uns diese beiden Tumorarten direkt miteinander und mit einem human Datensatz zu vergleichen. Unsere Ergebnisse ergaben, dass die PCCs und PGLs der Ratten gemeinsame Merkmale mit den humanen Tumoren aufweisen. Zudem zeigte sich, dass PGLs eine Genexpressionssignatur haben, die auf einen maligneren Tumortypen schließen lässt. Diese Genexpressionsdaten können von großer Bedeutung für zukünftige therapeutische Strategien sein und vertiefen das Wissen über maligne Tumore.

Zusammenfassend konnten wir eine neuartige und wirksame Behandlungsstrategie für PPGLs und pNETs durch die Kombination von PI3K- und CDK4/6-Inhibitoren demonstrieren. Darüber hinaus haben wir gezeigt, dass PGLs bei Menschen und MENX-Ratten Marker für Aggressivität exprimieren, was zu einem besseren Verständnis der Tumorprogression beiträgt.

Acknowledgments

First of all, I would like to thank my supervisor Natalia Pellegata. She gave me the opportunity to work in her lab – already before the PhD – and I am grateful for her constant support, guidance and scientific advice.
I want to thank the members of my Thesis Committee, Gabriele Multhoff and Susan Richter, for their help, support and positive feedback.

Thank you to Stephan Herzig and the whole IDC for the warm welcome in the institute and the nice working atmosphere. Also, thank you to Adriano Maida for the help with all the smaller and bigger issues around the lab.

In our group, I would like to say thank you to all the former and current members for their help and the nice working atmosphere. Thank you to Eva-Maria Bogner, Ninelia Minaskan, Hermine Mohr, Isabel Valenca, Ivo Hartlieb and Katyayni Ganesan. Also, I am grateful to Elke Pulz for her constant technical support.
I am especially thankful to Tobias Wiedemann for his constant help and support whenever needed, starting from the first internship I did in the lab throughout all the years of the PhD.
A special thanks goes to Swapna Satam for all her help in the lab, for all the entertaining WG-evenings and for the amazing food.

I would like to thank the members and organizing people of the adrenal SFB/TRR 205 and of the imaging SFB 824. And thank you to all the SFB205 young scientists for the nice time we had on retreats and workshops. Thank you to Svenja Nölting for providing us with the human PPGL tissue and to Martin Irmler for the array analysis.

Zu guter Letzt möchte ich mich ganz besonders bei meiner Familie und Freunden bedanken , ganz besonders bei meinen Eltern, Großeltern und meiner Schwester. Vielen Dank für eure Unterstüzung in so vielen Bereichen, nicht nur während der letzten vier Jahre sondern während meines gesamten Studiums.

Declaration

I confirm that this assignment is my own work and that I have not sought or used inadmissible help of third parties to produce this work and that I have clearly referenced all sources used in the work. I have performed all the experiments by myself with minor support for genotyping from Elke Pulz (technical staff) and for NuSAP immunohistochemical stainings from Katyayni Ganesan (Master student).

This work has not yet been submitted to this or any other examination institution.

Table of Contents

List of Abbreviations

ANOVA	Analysis of variance
ATP	Adenosine triphosphate
BCA	bicinchoninic acid
BSA	Bovine Serum Albumin
CDK	Cyclin-dependent kinase
CI	Combination index
CIP	CDK-interacting protein
CT	threshold cycle
ctrl	control
DAXX	Death-associated protein 6
DMSO	Dimethyl sulfoxide
DNA	Deoxyribonucleic acid
ECM	Extra-cellular matrix
ELISA	enzyme-linked immunosorbent assay
EMA	European Medicines Agency
FBS	fetal bovine serum
FDA	Food and Drug Administration
FFPE	Formalin-fixed paraffin-embedded tissue
GOBP	Gene Ontology Biological Process
GSIS	Glucose stimulated insulin secretion
H&E	Hematoxylin and eosin
HBSS	Hanks' Balanced Salt solution
HS	horse serum
IC50	half-maximal inhibitory concentration
IHC	immunohistochemistry
LMD	Laser Microdissection
MEN	Multiple endocrine neoplasia
MRI	Magnetic resonance imaging
MTC	Medullary thyroid cancer

NECs	neuroendocrine carcinomas
NENs	neuroendocrine neoplasias
NETs	Neuroendocrine tumors
PBS	Phosphate-buffered saline
PCA	Principal component analysis
PCC	Pheochromocytomas
PCR	Polymerase chain reaction
PET	Positron emission tomography
PGL	Paragangliomas
PHPT	Primary hyperparathyroidism
PI3K	Phosphoinositide 3-kinases
PIP	Phosphatidylinositol phosphate
pNETS	pancreatic neuroendocrine tumors
PP	Pancreatic polypeptide
PPGLs	Pheochromocytomas and Paragangliomas
qPCR	quantitative polymerase chain reaction
qRT PCR	quantitative real time polymerase chain reaction
RNA	Ribonucleic acid
RT	Room temperature / reverse transcription
SD	standard deviation
SSTRs	Somatostatin receptors
TBS-T	Tris-Buffered Saline - Tween
TCA cycle	citric acid cycle
TH	tyrosine hydroxylase
TSC	Tuberous sclerosis complex
ULA	Ultra-low attachment
UV	Ultraviolet
VHL	Von Hippel–Lindau tumor suppressor
WB	Western blot
WHO	World Health Organization

List of Figures

List of Tables

1. Introduction

1.1 Neuroendocrine System and its tumors

The neuroendocrine system is composed of cells of neuronal origin that have the ability to secrete hormones. It plays an important role in the human body by regulating processes as stress, basal metabolism, growth, reproduction, and lactation [1].

Neuroendocrine cells are located in various parts of the body and exist in two different compositions. They either display a diffused distribution in membranes of mucosal origin, e.g., in the digestive system or are organized as clusters of cells or whole organs like the adrenals, pituitary, pancreas, thyroid and others. [2]. Figure 1 illustrates the organs belonging to the neuroendocrine system. Common to all neuroendocrine cells is the ability to secrete hormones and the expression of markers such as chromogranin A and synaptophysin [2].

The origin of the neuroendocrine cells can be either epithelial or neuroectodermal, and they give rise to the neuroendocrine cells in the different organs. Cells of epithelial origin are mainly found in the gastrointestinal tract, the lungs, the thyroid and parathyroids, and the pancreatic islets. In contrast, cells of neuroectodermal origin are present in the paraganglia of the body, the adrenals, and the olfactory system [2].

Neoplasms arising from neuroendocrine cells are commonly described as neuroendocrine neoplasms (NENs). They can be further divided into well-differentiated neoplasms defined as neuroendocrine tumors (NETs), accounting for 80-90% of the NENs, and poorly-differentiated neoplasms defined as neuroendocrine carcinomas (NECs), as proposed by the latest World Health Organization (WHO) classification [3, 4].

As neuroendocrine cells are located all over the body, NENs can also be found in various tissues and organs of the body, with the most common ones occurring in the pancreas, the lungs and the gastrointestinal tract [4-6]. They can be divided into functioning or non-functioning according to their hormone secretion status [3].

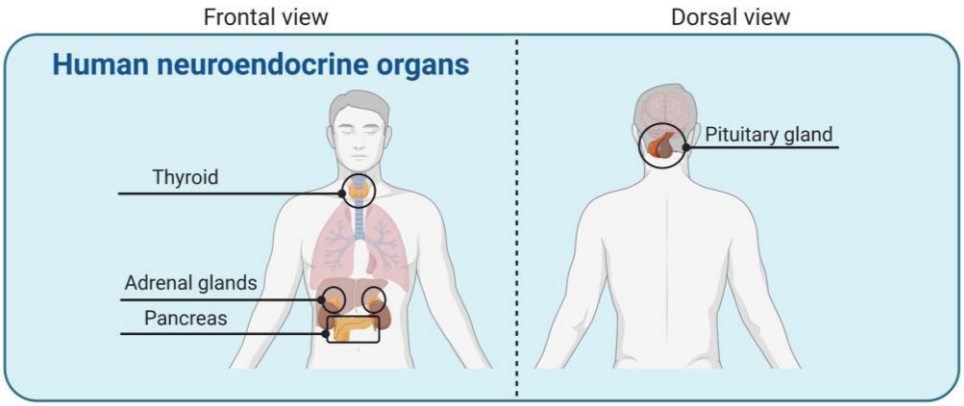

Figure 1: Neuroendocrine organs of the human body
Neuroendocrine cells are found in almost every organ of the body. Mayor neuroendocrine organs of the body involve the pineal and pituitary gland, thyroid, thymus, adrenal glands, pancreas, ovaries or testis. Created with BioRender.com

1.2 Adrenals and adrenal tumors

1.2.1 Adrenal glands and their function

The adrenals are small, triangular glands located on top of the kidneys, surrounded by an adipose capsule. They are made up of two different structures, the adrenal cortex and the medulla. The cortex produces steroid hormones and is divided into three zones: zona glomerulosa, zona fasciculata and zona reticularis.

The zona glomerulosa produces aldosterone and other mineralocorticoids, regulating electrolyte balance and blood pressure [7]. Glucocorticoids like cortisol and corticosterone are produced in the zona fasciculata. They regulate glucose homeostasis, immune response and stress response [8-10]. Androgens, such as dehydroepiandrosterone, are synthesized in the zona reticularis and play an important role in sex hormone levels [11, 12].

The medulla is composed of chromaffin cells derived from sympathoadrenal progenitor cells of neural crest origin. These progenitor cells populate the adrenal medulla and extra-adrenal sympathetic paraganglia during development and differentiate into hormone-producing cells [13].

These chromaffin cells produce catecholamines, namely epinephrine, norepinephrine and dopamine, which are stored in secretory vesicles and are released in the bloodstream after stimulation.

1.2.2 Pheochromocytoma and Paraganglioma (PPGLs)

Tumors arising from the chromaffin cells of the body are called pheochromocytomas (PCCs) and paragangliomas (PGLs), together referred to as PPGLs. According to the fourth edition of the WHO classification of endocrine tumors in 2017, pheochromocytoma is defined as intra-adrenal paraganglioma and paragangliomas as tumors of extra-adrenal sympathetic or para-sympathetic paraganglia [14]. The symptoms of PPGLs can be diverse and are based on the underlying hormonal profile of the tumors. The most common symptoms include hypertension, hypotension, headache, sweating, pallor, anxiety, tremulousness, nausea and vomiting [15].

PCCs account for up to 80%-85% of PPGLs, whereas PGLs make up 15%-20% [16, 17]. Each PPGL can spread to distant sites, and there is currently no highly effective medical therapy for metastatic tumors. Although less common, PGLs show a higher metastatic potential than PCCs, which is up to 35% and 5%-20%, respectively [18-20]. This highly affects the prognosis of these tumors, as metastases are the determining factor for mortality [21], so that metastatic patients have a 5-year survival rate of 45%-95% [22-24].

The main-stay treatment for localized PPGLs is surgery with perioperative medical management to prevent cardiovascular complications [25]. Unfortunately, surgery is not an option in many metastatic cases, and the treatment for these patients is suboptimal and needs further improvement [17]. The elucidation of the molecular mechanisms associated with PPGLs development and progression is a necessary step to new therapy options and more personalized treatments.

The biochemical diagnosis of PPGLs relies on the detection of increased catecholamine levels in blood or urine [26]. Additionally, imaging studies are carried out to identify the localization of the primary tumor and to detect possible metastases using CT, MRI or PET/CT with tracers like ^{18}F-dihydroxyphenylalanine ^{18}F-fluorodeoxyglucose and ^{68}Ga-DOTATATE [26]. Somatostatin analogs as DOTATATE or DOTATOC take advantage of the common expression of somatostatin receptors (SSTRs) in neuroendocrine cells and are also used in the diagnosis and treatment of other neuroendocrine tumors [27, 28].

PCCs are diverse in their biochemical profile, they normally all produce epinephrine but show differences in their norepinephrine secretion. Therefore, half of the PCCs are adrenergic,

whereas the other half are noradrenergic [29]. PGLs, on the other hand, are primarily noradrenergic with high and/or exclusive norepinephrine production. The only exceptions are head and neck PGLs that, except for low levels of dopamine, do not produce any catecholamines [30].

In general, PPGLs show considerable genetic heterogeneity; up to date, 15 driver genes have been identified, together with 12 different genetic syndromes and multiple genes that can potentially influence the disease [21, 31, 32]. In recent years it has become common to group PPGLs in two or more subgroups based on their molecular profile, their behavior and treatment potential. Based on their genetic signature, PPGLs can be divided into three clusters: the first is the pseudohypoxic, the second the Wnt-signaling, and the third the kinase-signaling cluster (Figure 2) [21, 32].

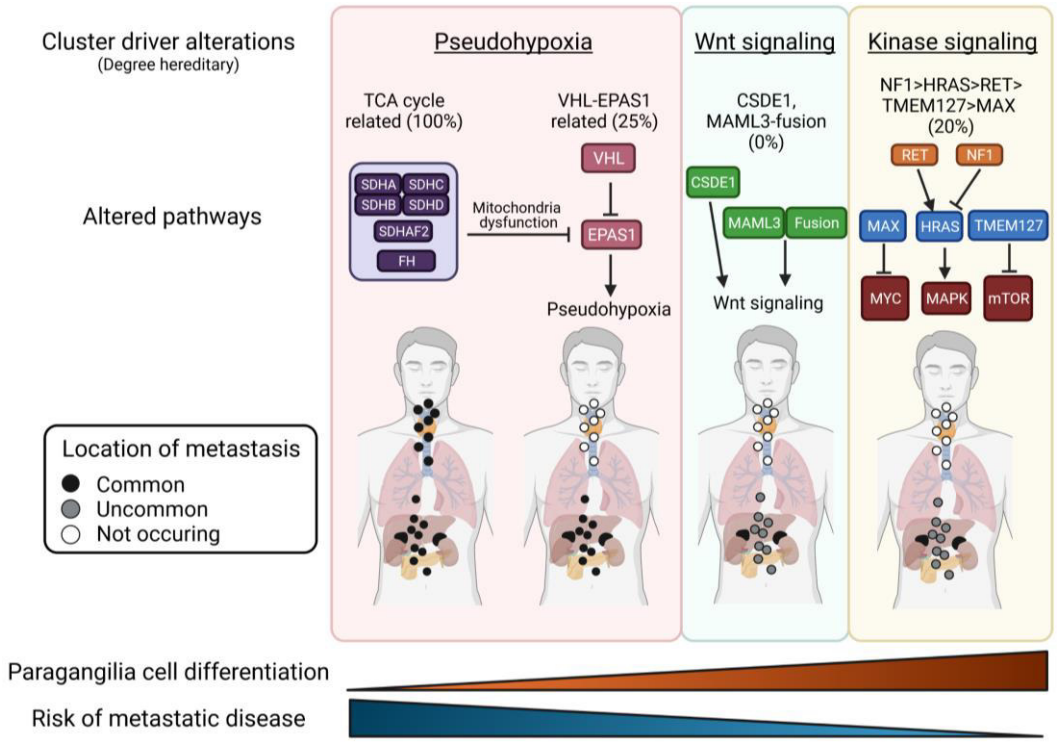

Figure 2: Molecular subgroups of PPGLs
Shown are the three main molecular subgroups of PPGLs with their respective driver mutations, altered pathways and the location of the tumors. Additionally, cell differentiation and metastatic risk are shown. Created with BioRender.com

The pseudohypoxic cluster is characterized by a stabilization of hypoxia-inducible factors (HIFs), even though these tumors do not lack oxygen. This pseudohypoxic cluster can be further divided into two groups: TCA cycle-related oncometabolite accumulation and VHL/EPAS1-related direct disturbance of HIF turnover [21, 32]. The TCA cycle group is associated with mutations in the *SDHx* and *FH* genes [33-38]. On the other hand, the VHL/EPAS1 group is characterized by increased transcription of HIF-2α target genes due to mutations in *VHL* or *EPAS1* that lead to a stabilization of HIF and result in increased proliferation, angiogenesis and decreased apoptosis [39-44].

The Wnt-signaling cluster includes only sporadic cases bearing mutations in *CSDE1* or somatic gene fusions involving *UBTF-MAML3*. These alterations cause activation of Wnt and Hedgehog signaling [32].

The kinase-signaling cluster comprises both sporadic and familial cases and predominantly shows PCCs [32]. The most common hereditary mutation affects the *RET* proto-oncogene and is associated with the MEN2 multi-tumor syndrome (see below). Further mutated genes in this cluster include *NF1*, *TMEM127*, *FGFR1*, *KIF1B*, *MET*, and *HRAS [32, 45-49]*.

1.3 Pancreas and pancreatic tumors

1.3.1 Pancreas and its function

The pancreas is an oblong-shaped organ located in the upper abdomen behind the stomach and functions both as an exocrine and endocrine gland. Anatomically, it can be divided into five parts: head, uncinate process, neck, body and tail (Figure 3).

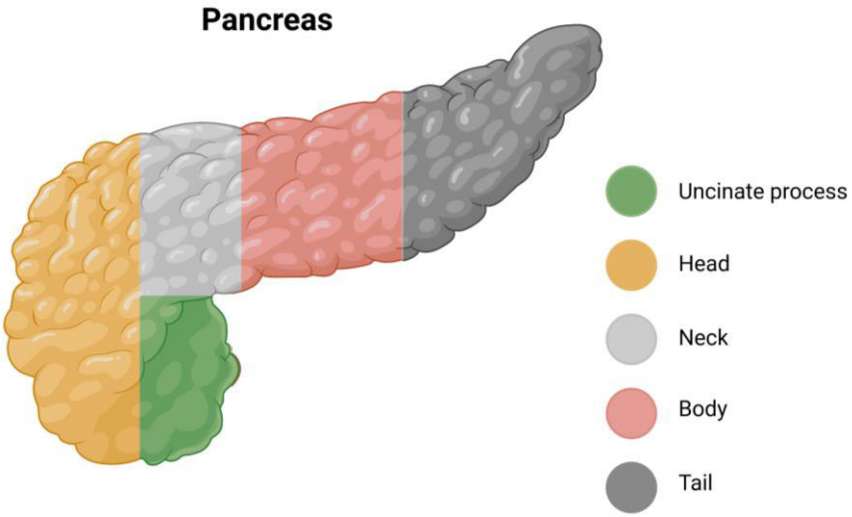

Figure 3: Structure of the pancreas
The pancreas is an oblong-shaped organ and can be divided into head, uncinate process, neck, body and tail. Created with BioRender.com

To exert its function as an exocrine gland, the pancreas has a duct system that is connected with the bile duct to form the hepatopancreatic duct in order to release digestive enzymes into the duodenum. The exocrine pancreas, being composed of acinar tissue and secreting digestive enzymes like trypsin, lipase and amylase, makes up the majority of this organ.
The endocrine part of the pancreas is composed of the islets of Langerhans. The islets are distributed in the pancreas and lie within the exocrine tissue. They secrete hormones that are directly released into the bloodstream. Five different cell types make up the islets of Langerhans and are called alpha-, beta-, delta-, epsilon- and PP-cells (Figure 4).
The majority of the pancreatic cells are the insulin-producing beta cells, followed by the glucagon-producing alpha cells and the somatostatin-producing delta cells. The epsilon cells, which produce ghrelin and the PP cells, which produce pancreatic polypeptide, make up only a small part of the total cell mass. It has to be noted that the organization of these cell types within the islets differs between rodents and humans. Whereas in rodents, the islets have a

structured phenotype with the beta cells in the center and alpha and delta cells in the periphery, in humans, the different cell types are evenly distributed within the islets (Figure 4).

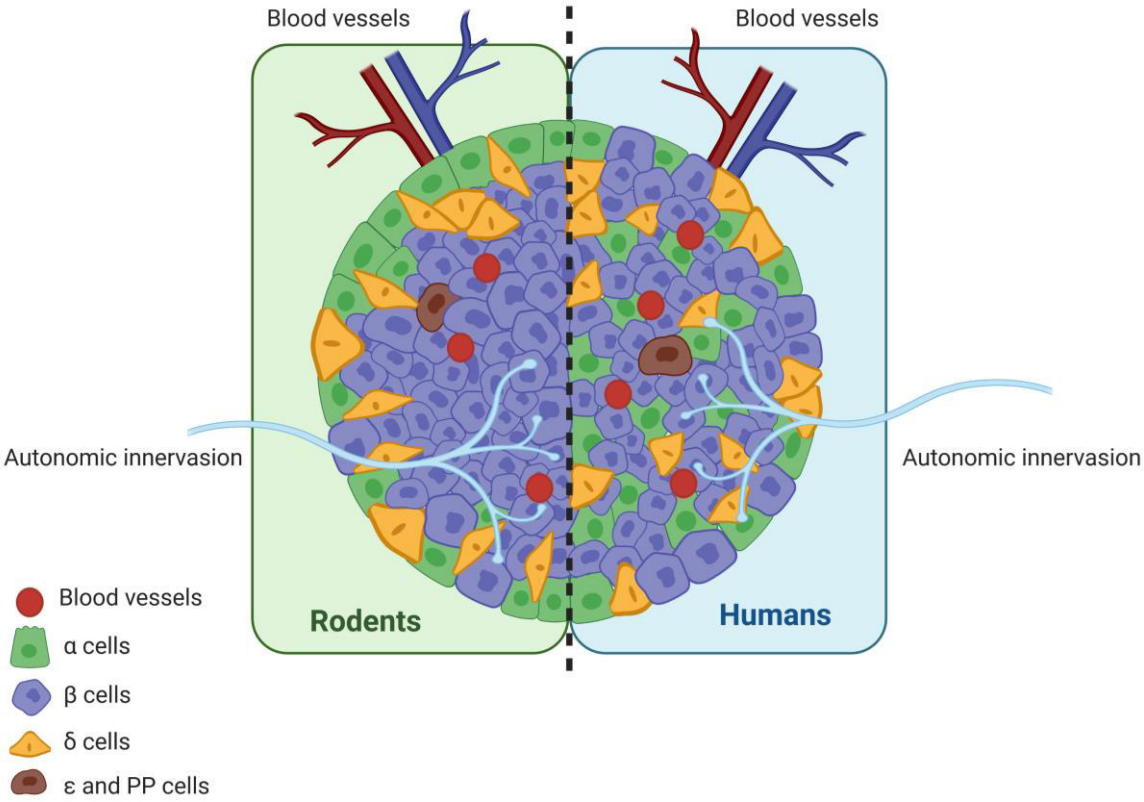

Figure 4: Composition of pancreatic islets in rodents and humans
Pancreatic islets consist of five different cell types that exert different functions. The three most common cell types are the insulin-producing beta-cells, the glucagon-producing alpha-cells and the somatostatin-producing delta-cells. Additionally, also epsilon-cells secreting ghrelin and PP-cells producing pancreatic polypeptide are found in the pancreatic islets. The distribution of these cell types in the islets is different between humans and rodents. While rodents show a more organized structure with centered beta-cells, in humans, the five cell types are evenly distributed within the islets. Created with BioRender.com

1.3.2 Pancreatic tumors

The vast majority of pancreatic tumors arise from the exocrine parts, with adenocarcinomas being the most common ones within this group. Pancreatic neuroendocrine tumors (pNETs) only account for 1%-2% of all pancreatic cases, even though the incidence increased over the last decades [50-54].

In general, pNETs can be divided into functioning or non-functioning tumors depending on their hormone secretion status. Most of the pNETs are of non-functioning nature, and their prognosis is worse than that of the functioning tumors. This might be related to the fact that they are usually discovered at a more advanced stage [54-56]. Functioning pNETs are classified by the hormones they release. The most common groups are gastrinomas, insulinomas, glucagonomas, and somatostatinomas. Due to hormone overproduction and the associated symptoms, these tumors are often diagnosed earlier than the non-functioning ones [55].

Most of the pNETs occur as sporadic cases. The hereditary cases are associated with syndromes such as MEN1, von Hippel-Lindau (VHL) disease, neurofibromatosis 1 (NF-1), and tuberous sclerosis (TSC). Interestingly, genes associated with these diseases are also mutated in sporadic cases. It has been shown that 44% of sporadic pNETs have inactivating mutation in the *MEN1* gene and another 43% of cases have alterations affecting the DAXX (death-domain associated protein) and ATRX (alpha thalassemia/mental retardation syndrome X-linked) complex [57].

Besides a biochemical hormone profile, imaging plays an important role in the diagnosis of pNETs. CT and MRI are used as conventional imaging methods, whereas functional imaging is carried out by exploiting the elevated SSTR (somatostatin receptor) expression of NETs and employs radiolabeled SSTR agonists such as DOTATATE [55].

The first-line treatment for localized tumors is surgery. For lesions that are small (<2cm) a "watch-and-wait" approach is an option [55, 58, 59]. Treatment of advanced tumors often relies on SSTR expression: somatostatin analogs are used to both suppress hormone secretion and inhibit tumor growth [55]. Furthermore, radiolabeled SSTR analogs are not only used for imaging but also for radiotherapy upon conjugation with yttrium-90 (^{90}Y) or lutetium-177 (^{177}Lu) [55].

Even though new treatment strategies have been proposed over the last few years, there is still a need to find more effective therapy options for malignant and especially metastatic

cases. A broader option of treatment choices would also allow for more personalized treatment in the future.

1.4 Multiple endocrine neoplasias (MEN)

Multiple endocrine neoplasias (MEN) are a group of autosomal dominant disorders that lead to tumors in more than one neuroendocrine-derived tissue. To date, three different types of MEN are distinguished in humans, namely MEN1, MEN2 and MEN4.

MEN1

MEN1 (OMIM #131100) is the most common MEN syndrome and shows high penetrance of the tumor phenotype. It is caused by inactivating germline mutations in the tumor suppressor gene *MEN1* [60]. The most common organs affected by this syndrome are the parathyroid, the enteropancreatic tract and the anterior pituitary gland. Furthermore, tumors can occur as foregut carcinoids and gastric enterochromaffin-like tumors[61]. The *MEN1* gene is located on chromosome 11q13 and encodes for the protein menin [60, 62]. Menin is a highly conserved and ubiquitously expressed protein, mainly found in the nucleus, exerting many functions [61]. Indeed, it is involved in transcriptional regulation, genome stability, cell division, cell proliferation, apoptosis and repression of telomerase expression [60-67].

MEN2

Another MEN syndrome is MEN2, a familial cancer syndrome characterized by mutations in the *RET* proto-oncogene [68]. The MEN2 syndrome is characterized by the occurrence of medullary thyroid carcinoma (MTC). MEN2 can be further divided into subgroups, of which the two most important ones are MEN2a (OMIM #171400) and MEN2b (OMIM #162300) [69]. Accounting for 55% of the cases, MEN2a is the more common type. It is associated with the development of MTC and additionally of PCCs plus primary hyperparathyroidism(PHPT). MEN2a shows a better prognosis than MEN2b [70, 71]. With 5%-10% of all cases, MEN2b is rarer and it is characterized by an aggressive form of MTC together with PCC and marfanoid habitus. MEN2b is associated with early death (before 30 years of age) [70, 72].

MEN4

MEN4 is a MEN syndrome that was recently discovered by analyzing samples from patients that showed symptoms similar to MEN1 but had no mutation in the *MEN1* gene. Upon further examination, mutations of the *CDKN1B* gene encoding for the protein p27 (Kip1) were found to be the causative genetic alteration [73-75]. The p27 protein is a cell cycle regulator, important for the G1 to S phase transition and a tumor suppressor [74, 76, 77].

Due to a relatively small number of cases, the disease phenotype of MEN4 is not as defined as for the other MEN syndromes. Parathyroid and pituitary adenomas are the most commonly affected tissues [74, 78, 79].

Table 1: MEN diseases in humans

Shown are the four different types of MEN diseases in humans, namely MEN1, MEN2a, MEN2b and MEN4, with their respective tumor spectrum. PHTP= primary hyperparathyroidism; MTC= medullary thyroid cancer; PPGL= pheochromocytomas and paragangliomas; pNET= pancreatic neuroendocrine tumors

Tumor type	MEN1	MEN2a	MEN2b	MEN4
Pituitary Adenoma	x		x	x
PHPT	x	x		x
MTC		x	x	
PPGL	x	x	x	
pNET	x			x

1.5 Signaling pathways in neuroendocrine tumors

1.5.1 PI3K Pathway

1.5.1.1 The PI3K pathway – an overview

The PI3K/AKT pathway is one of the most important intracellular signaling pathways as it is involved in several important processes such as metabolism, growth, proliferation, survival, transcription and protein synthesis [80]. The lipid phosphoinositide 3-kinases (PI3Ks) are conserved kinases that phosphorylate the 3'-hydroxyl group of phosphoinositides. An important product of this reaction is the second messenger PIP3 (phosphatidylinositol-3,4,5-trisphosphate) that recruits the AKT-Kinase to exert further signaling, as shown in Figure 5 [81, 82].

PIP3 is produced by class I subclass of PI3Ks that can be further divided into class IA and class IB. In detail, class IA enzymes are heterodimers that consist of regulatory and catalytic subunits. The p110 catalytical subunit is repressed by the p85 regulatory subunit in non-activated cells. Upon activation, the regulatory subunit activates p110 by interaction with phosphotyrosine residues. The activated p110 subunit of PI3K then phosphorylates PIP2 to generate PIP3. It is important to note that four different p110 subunits (α, β, γ, δ) exist and they are thought to have an impact on different downstream signaling pathways. After generation of PIP3, downstream signaling proteins that harbor pleckstrin-homology (PH) domain are recruited and bind to PIP3. Amongst the most important of these proteins are the kinases AKT and PDK1. Due to the association to PIP3, these two kinases are brought into proximity, which enables AKT to be phosphorylated by PDK1 or by PIP3 directly. By this, AKT is activated and can now phosphorylate numerous other proteins, including BAD, mTOR, AP-a, NFκB and FKHR1, affecting growth, survival, and many other functions (Figure 5).

To date, only class IA of PI3Ks has been associated with human cancer. Nevertheless, the PI3K pathway is amongst the most frequently altered signaling pathways in cancer and is dysregulated in up to 50% of cases [83, 84].

Dephosphorylation of PIP3 is carried out by PTEN, a well-described tumor suppressor that is also altered in many cancers [81, 85, 86]. PTEN dephosphorylates PIP3 to PIP2 and thereby inhibits the recruitment and activation of AKT and the downstream PI3K pathway [86].

PIP3 production by PI3Ks is induced by stimulation of receptor tyrosine kinases, integrins, B and T cell receptors, cytokine receptors, G-protein-coupled receptors and other stimuli [87-91].

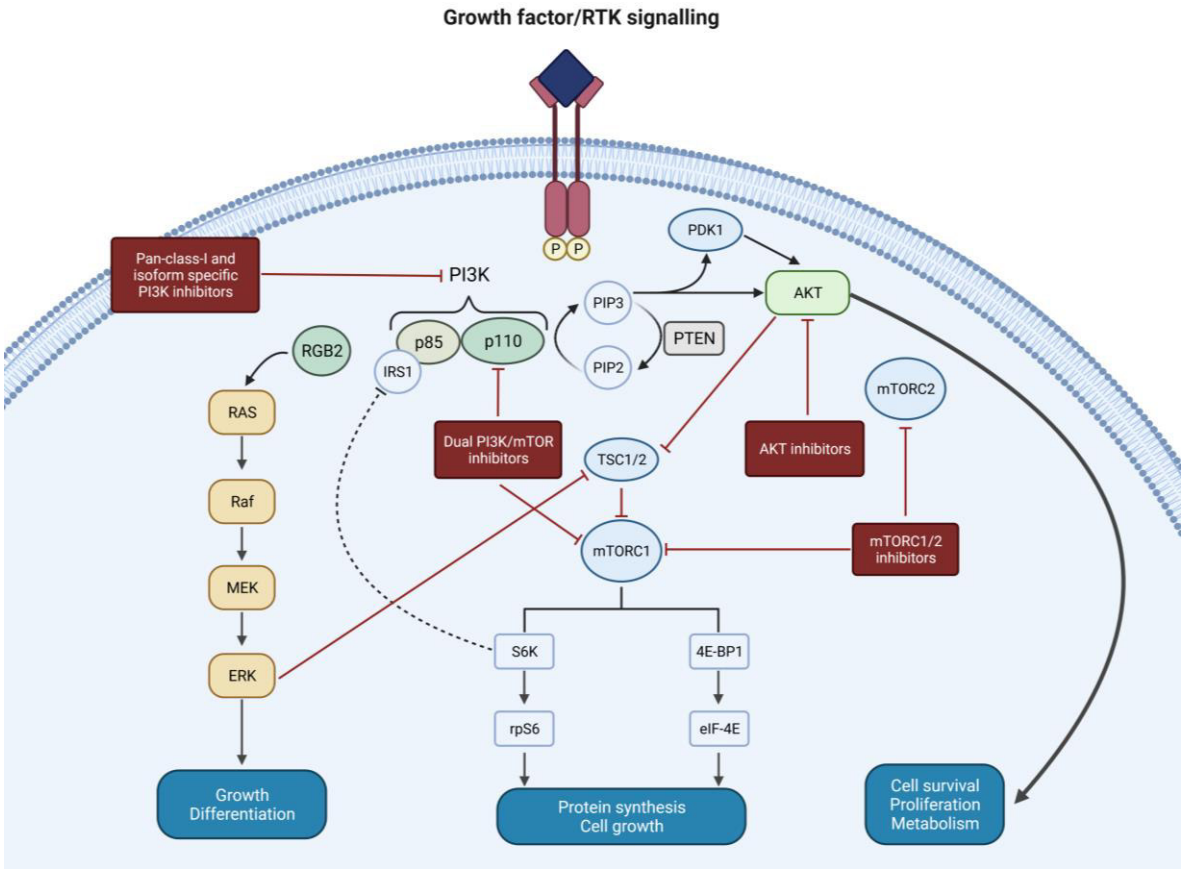

Figure 5: PI3K signaling pathway
Being one of the most important signaling pathways in cells, the PI3K pathway is involved in many processes associated with proliferation and survival. Upon stimulation, the activated p110 subunit phosphorylates PIP2 to PIP3. The second-messenger PIP3 then phosphorylates AKT, which is thereby activated and further activates many proteins involved in cell growth, survival and other mechanisms. This chain of events is prohibited by the tumor-suppressor PTEN that dephosphorylates PIP3 to PIP2. Created with BioRender.com

1.5.1.2 Drug targeting of the PI3K/AKT pathway

Due to the importance of the PI3K/AKT pathway in the development and progression of cancer, many drugs targeting this pathway at different levels have been developed. Amongst these is the PI3K inhibitor BKM120 (Buparlisib).

BKM120 belongs to the class of pan-PI3K inhibitors, inhibiting all four catalytic subunits of p110 [92]. It has not yet been approved by FDA or EMA but is used in several clinical trials.

1.5.1.3 The role of the PI3K/AKT pathway in PPGLs

The PI3K/AKT pathway is known to be upregulated in the rat pheochromocytoma PC12 cell line, used for many studies in PPGLs, and protects this cell line in vitro against cytotoxic agents [93, 94]. Furthermore, studies of human cancer material revealed high levels of phosphorylated AKT by Western Blot and immunohistochemistry stainings [94, 95]. In addition to this, MENX rats carrying a frameshift mutation in the gene encoding for p27 develop bilateral PCCs [73, 96]. p27 is a cell cycle inhibitor and a direct target of AKT. In addition, reduced p27 expression was found in human PCCs [97]. Despite the evidence of PI3K/AKT involvement in PPGLs, not many drugs targeting this pathway have been evaluated for use in PPGLs and so far, mainly mTOR inhibitors and BYL719, a PI3K inhibitor, were used for clinical studies [98, 99].

1.5.1.4 The role of the PI3K/AKT pathway in pNETs

In pNETs, a downregulation of PTEN has been shown, suggesting an involvement of the PI3K/AKT pathway in these tumors [100, 101]. Additionally, studies have shown mutations in other parts of the PI3K pathway and also that AKT is often overexpressed in pNETs [57, 102, 103]. Similar to the situation in PPGLs, also in pNETS primarily mTOR inhibitors are used for therapy in the clinics to downregulate the PI3K/AKT pathway [104-106].

1.5.2 CDK4/6 pathway

1.5.2.1 The CDK4/6 pathway – an overview

CDK4 and CDK6 are two important enzymes that promote cell cycle progression from G1 to S phase by phosphorylating key downstream target proteins [107, 108]. Upon mitogenic stimuli through various signaling pathways, CDK4 and CDK6 together with D-type cyclins (D1, D2, D3) form the so-called cyclin D-CDK4/6 complexes. The catalytically active cyclin D-CDK4/6 complexes further phosphorylate and thereby inactivate members of the pRB protein family as p107, p110 and p130 [109]. In quiescent cells, pRB proteins are bound to E2F proteins, a family of transcription factors involved in cycle progression, DNA replication, and mitotic progression [110, 111]. When pRB is bound to E2F, transcription is repressed through the recruitment of repressive chromatin marks, histone modifiers, and chromatin remodeling proteins [112]. Phosphorylation of pRB decreases its affinity for E2F, resulting in the release of E2F and the disruption of the entire repressive complex, leading to the transcription of E2F target genes required for S phase entry [109, 112]. As this process represents a crucial step in cell cycle progression, it is tightly regulated and there are several known inhibitors of CDK4/6 kinase activity such as p21, p27, p57 belonging to the CDK-interacting protein/kinase inhibitory protein (CIP/KIP) family and p16, p14, p18, members of the inhibitor of CDK4 (INK4) family [109]. CDK4/6 are major players in the control of cell cycle progression, and are therefore upregulated in many types of cancers [109].

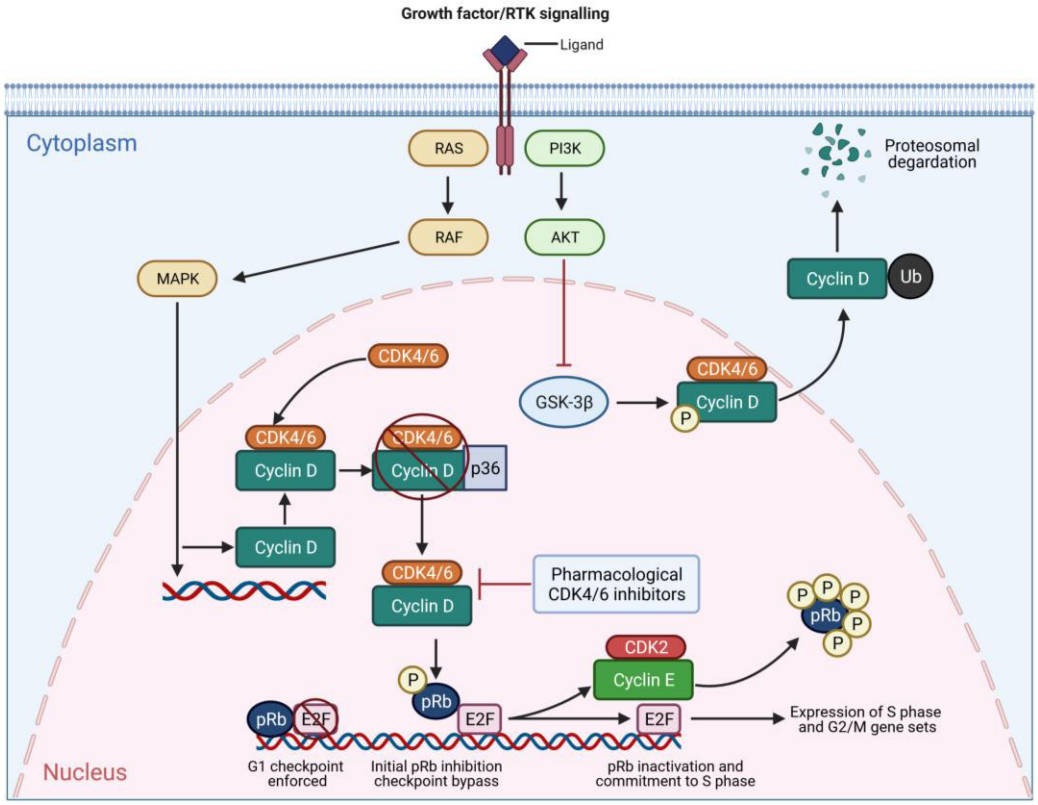

Figure 6: The CDK4/6 pathway
The CDK4/6 pathway is an important signaling pathway involved in the progression of the cell cycle from G1 to S phase. Being activated by various mitogenic stimuli, CDK4/6 form complexes with cyclin D. The so-obtained cyclin D-CDK4/6 complex then phosphorylates the tumor-suppressor pRB, resulting in an inactivation of pRB. This enables E2F transcription factors to promote gene transcription and the production of proteins necessary for the G1 to S progression. Created with BioRender.com

1.5.2.1 Drug targeting of the CDK4/6 pathway

Ribociclib is a potent CDK4/6 inhibitor approved for the treatment of hormone receptor-positive, HER2-negative advanced breast cancer treatment by the FDA and EMA in 2017 [113]. Since then, Ribociclib has been used in many studies to investigate its role as a potential new drug in other cancer types, including NETs [114-116].

Even though a combination of CDK4/6 inhibitors – including Ribociclib – with aromatase inhibitors or ER inhibitors showed great effects and increased progression-free survival, the cancer relapsed and disease progressed, showing the importance of overcoming resistance when using CDK4/6 inhibitors [117].

1.5.2.2 The role of the CDK4/6 pathway in PPGLs

In general, it has been reported that the CDK4/6 pathway – involving pRB- is dysregulated in various NETs, including pNETs and PPGLs [118]. Furthermore, a trend for an association between a shorter overall survival and loss of *CDKN1B* expression was observed in these NET patients [118]. Additional data also suggests a moderate to high expression of CDK4, CDK6 and Rb in patients with PPGLs [119, 120].

Involvement of a dysregulated cell cycle via the CDK4/6-Rb axis has been reported in the MENX rat model, in which affected animals harbor a mutation in p27 and therefore develop PPGLs [96, 121]. p27 is a well-described tumor suppressor and inhibits cyclin-dependent kinase (Cdk) inhibitors that regulate G1 to S phase cell cycle transition [76].

1.5.2.3 The role of the CDK4/6 pathway in pNETs

It has been shown in human patients that normal islets express neither CDK4 nor pRB [122]. Interestingly, in patients with pNETs, CDK4, pRB, and CDK1 are highly expressed, suggesting an activation of the CDK4/6 axis in these tumors [122].

In support of this, different animal models like the Men1(+/-); Cdk4(-/-) double knockout mice and the MENX rats showed the direct involvement of CDK4 and the cell cycle axis in the tumorigenesis of pNETs [123, 124].

1.6 Animal models of NETs

Animal models recapitulating human diseases, including cancer, have been instrumental in improving our understanding of tumor biology, evaluate novel medications, and test treatment strategies.

Despite ongoing efforts to identify *in vitro* models that can mimic the in vivo situation, higher organisms are very complex. The crosstalk of cells in the microenvironment and the interplay of physiological functions and organs is of great importance for cancer development, progression, and especially for cancer treatment studies. Representative cancer models allow testing the effect of novel therapies before their clinical implementation. Therefore, animal models are still important and needed in research today.

1.6.1 MENX rats

In 2002 a new, hereditary syndrome was described that causes the development of multiple endocrine tumors in a Sprague-Dawley rat strain [96]. It was called MENX and was found to be caused by a homozygous tandem duplication of eight nucleotides in exon 2 of the *Cdkn1b* gene. This causes a frameshift mutation leading to a mutant p27 protein that is highly unstable [73, 125]. Tissues of the affected animals show a reduction or loss in p27 expression. MENX affected rats develop bilateral PCCs, abdominal PGLs, multifocal pituitary adenoma, multifocal thyroid C-cell hyperplasia and endocrine pancreatic hyperplasia [96]. This syndrome has features overlapping with those of both human MEN1 and MEN2 syndromes. Furthermore, the genetic of the MENX rats is similar to that of human MEN4 patients with mutations in *CDKN1B* [121].

Both homozygous and heterozygous mutant MENX rats develop the same endocrine tumors but with different kinetics. In general, tumors in homozygous rats develop faster than those in heterozygous animals, and consequently, homozygous rats die at eight months of age, whereas heterozygous rats live up to 18 months (Figure 7) [126].

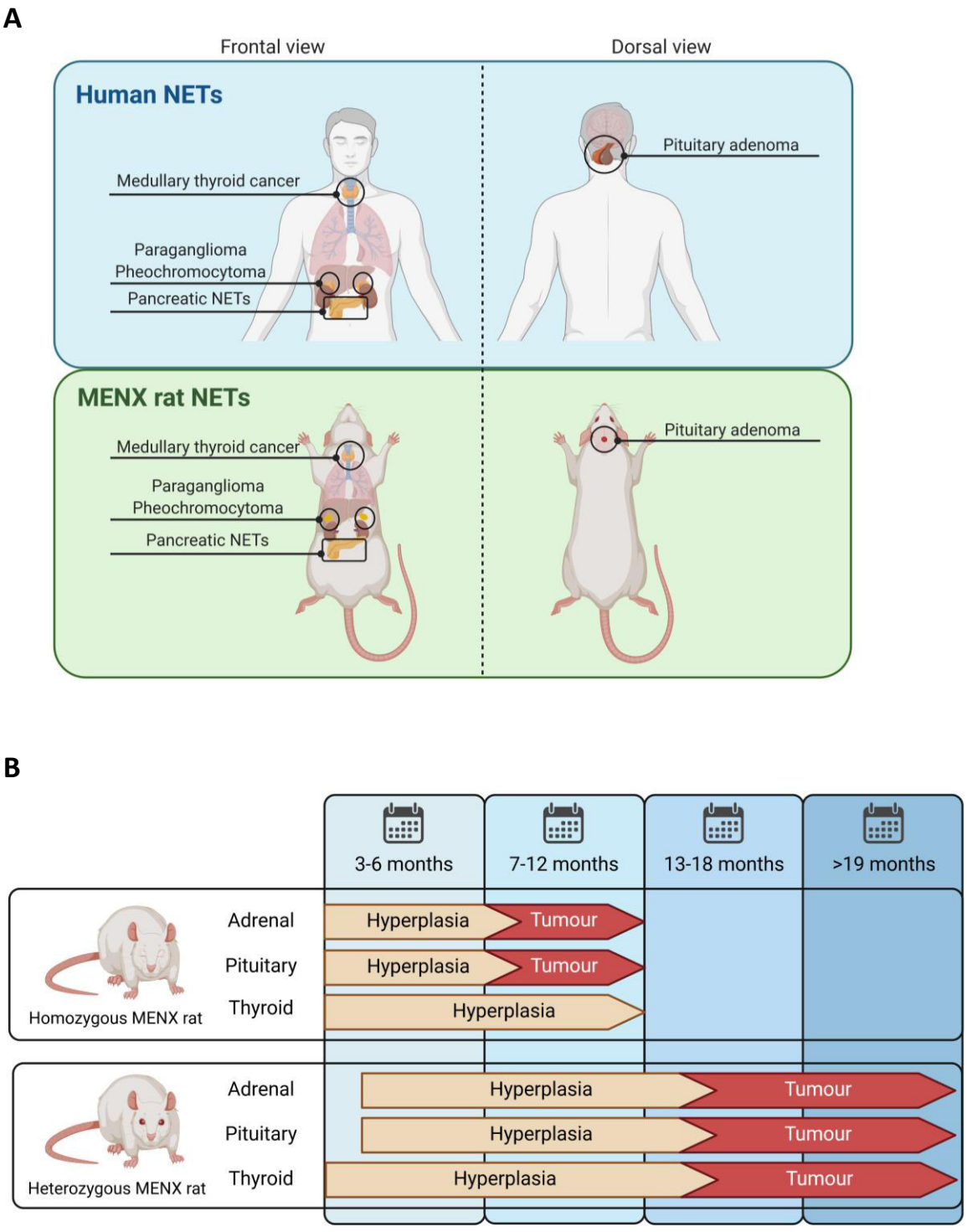

Figure 7: Tumors and corresponding timeline in MENX rats
Shown are the NETs arising in MENX rats (A, B), humans (A) and the timeline in MENX rats (B). Hyperplasia can be seen from a young age, whereas tumors arise starting from 7 months in the homozygous and from 15 months on in the heterozygous animals. Created with BioRender.com

PPGLs in MENX

Homozygous (mut/mut) MENX rats develop bilateral PCCs with complete penetrance. Hyperplasia in the adrenals starts at two months of age and progresses over time to PCCs, which replace the medulla and compress the cortex after eight months of age [73, 125]. PNMT expression was not found in these tumors, indicating that they are noradrenergic, which was confirmed by biochemical catecholamine profiles. In heterozygous (wt/mut) animals, adrenal tumors are detectable at 5-6 months of age, and they progress further to be visible nodules by 12 months and develop to PCCs, that replace the medulla and compress the cortex with 16 months of age [126]. Additionally, the rats also develop PGLs with a lower penetrance. Several studies in the lab investigated genes and pathways upregulated in tumors of homozygous animals. Amongst others, upregulation and over-activation of the Bmp-Smad and the PI3K/AKT pathway were shown in tumors versus normal adrenal [125, 127-129].

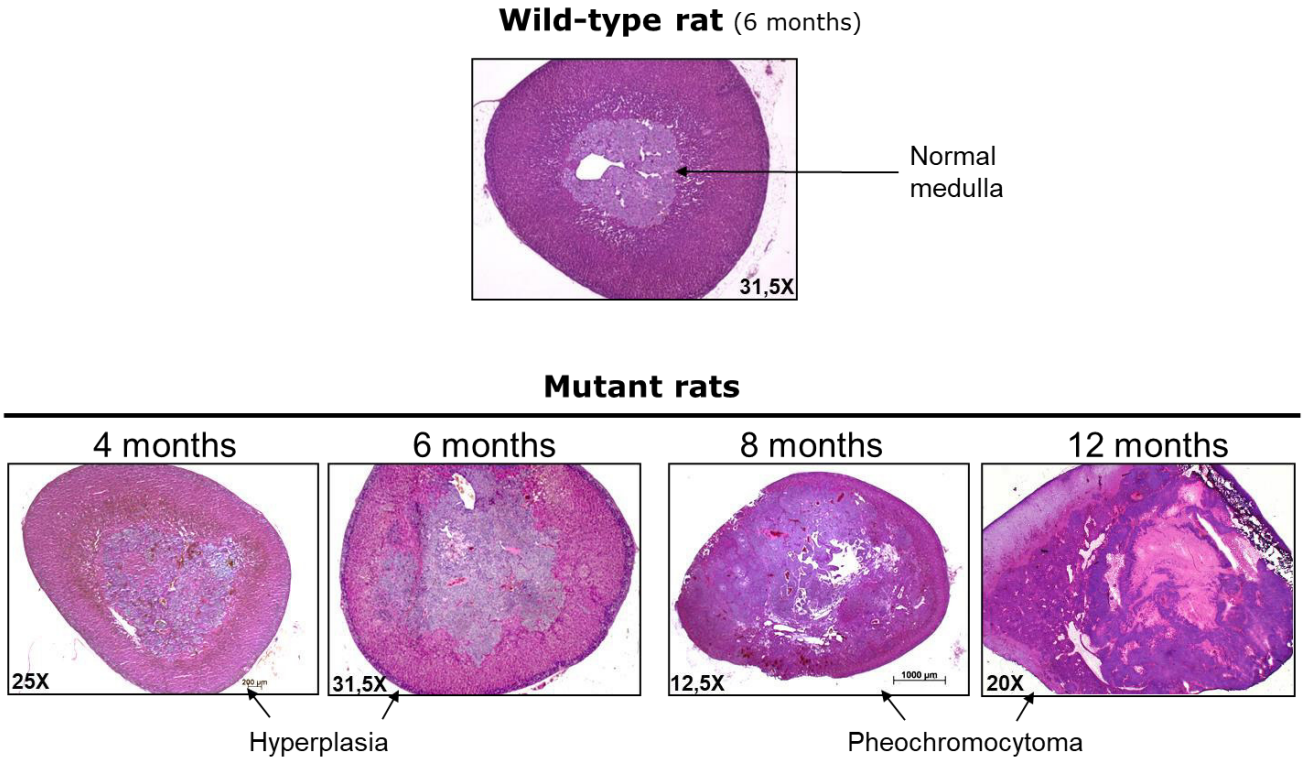

Figure 8: H&E of adrenal glands from MENX rats of different age
Shown are the adrenal H&E stainings from a 6 month old wild-type rat and 4-12 months old homozygous mutants. Hyperplasia of the adrenal medulla can be seen in 4 and 6 month old animals. From 8 months on, PCCs are observed in the adrenals that show a high medullary mass and less cortex compared to the wild-type gland.

Pancreatic lesions in MENX

Homozygous MENX rats show an increased islet cell mass both at 14 days and at 7.5 months of age. An increase in the number of all the different endocrine cell types (beta-cells, alpha-cells, delta-cells and PP-producing cells) was observed and additionally, adult animals also showed an increase in ghrelin-positive epsilon-cells [123].

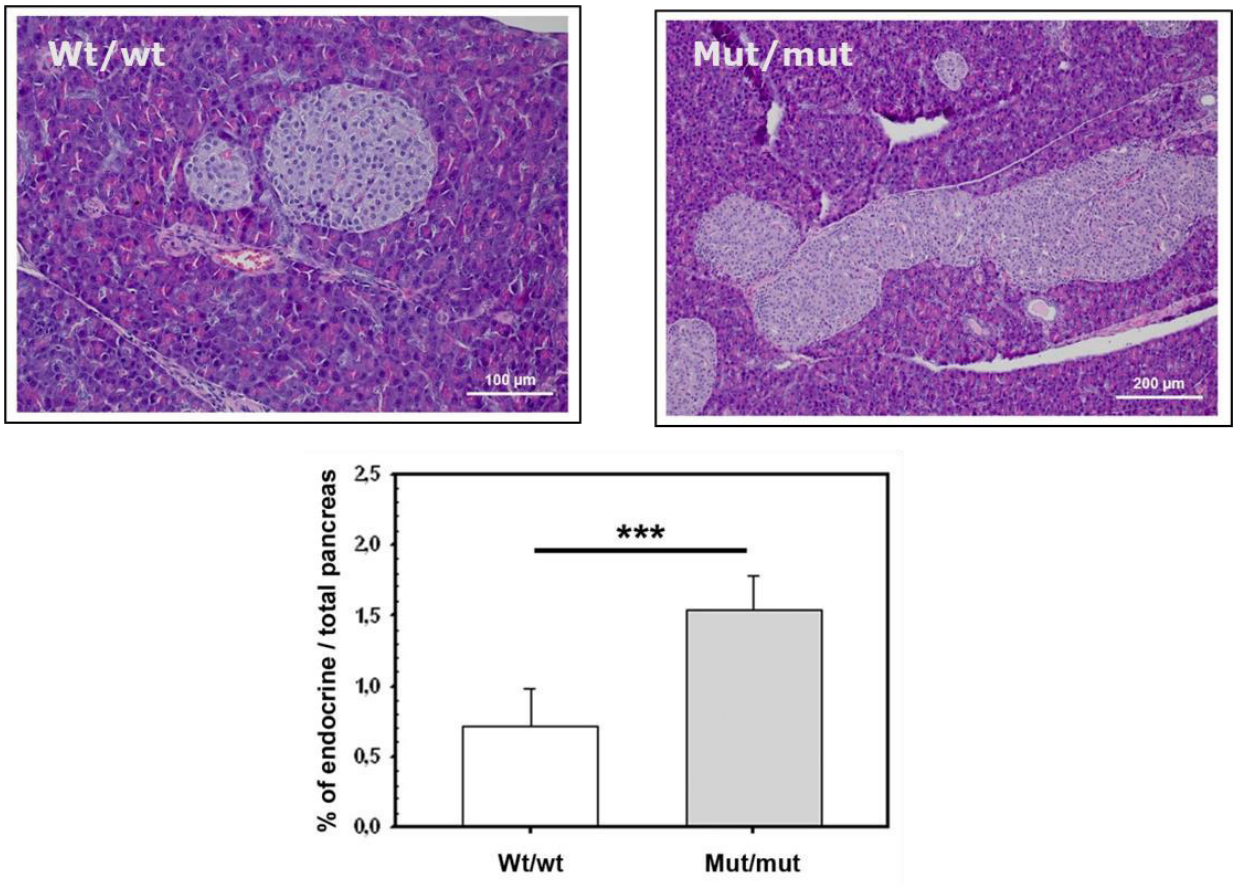

Figure 9: H&E of pancreatic tissue from MENX rats
Shown are pancreatic H&E stainings of a wild-type and a homozygous mutant. It can be seen that the islets in the mutants show a bigger mass. Quantification of islet mass revealed a significantly increased islet mass in mutant animals.

1.6.2 Men1+/- mice

As explained above, the *MEN1* gene is the gene responsible for the MEN1 syndrome, and it is often mutated in sporadic pNETs.

Various mouse models of the MEN1 syndrome have been generated in order to study its genetics and the development of the associated tumors. It was found that Men1+/- mice develop multiple NETs similar to MEN1 patients. In contrast, homozygous deficiency of *Men1* is embryonic lethal [130]. Almost all of these mice develop multiple tumors that can develop in the thyroid, pancreas, pituitary, adrenals and other organs from 13 months onwards [130].

The strain that is available in our lab was generated using a conditional approach, deleting the third exon and inserting a neoTK cassette into intron 2 of the *Men1* gene [131]. Mice that are homozygous for the mutant *Men1* gene (Men1-/-) die between E11.5 and E13.5, whereas heterozygous mice (Men1+/-) develop normally with tumors being detectable from 12-13 months on [130, 131]. These mice represent closely the endocrine tumors that occur in MEN1 patients, as illustrated in Table 2 [130].

Table 2: Tumors arising in Men1 +/- and +/+ mice

Shown are the tumors arising in Men1+/- and wild-type mice of different age and their incidence.

Organ/Tissue Type of pathology	8–12 Months		13–18 Months		19–26 Months	
	Wild type (n = 9)	$Men1^{+/T}$ (n = 23)	Wild type (n = 12)	$Men1^{+/T}$ (n = 36)	Wild type (n = 22)	$Men1^{+/T}$ (n = 61)
Parathyroid						
Dysplasia	0/5	0/5	0/12	1/17 (5.9%)	2/20 (10%)	0/33
Adenoma	0/5	1/5 (20%)	0/12	7/17 (41.2%)	0/20	21/33 (63.6%)
Carcinoma	0/5	0/5	0/12	0/17	0/20	1/33 (3%)
Extrapancreatic gastrinoma						
Adenoma	0/8	1/12 (8.3%)	0/5	2/20 (10%)	0/6	3/17 (17.6%)
Carcinoma	0/8	0/12	0/5	1/20 (5%)	0/6	1/17 (5.9%)
Pancreatic islets						
Hyper/dysplasia	0/9	15/23 (65.2%)	2/13 (15.4%)	13/34 (38.2%)	0/21	7/61 (11.5%)
Adenoma	0/9	5/23 (21.7%)	0/13	4/34 (11.7%)	0/21	12/61 (19.7%)
Carcinoma	0/9	2/23 (8.7%)	0/13	13/34 (38.2%)	0/21	37/61 (60.6%)
Pituitary						
Adenoma	0/7	1/23 (4.3%)	0/8	2/31 (6.4%)	0/20	10/60 (16.6%)
		F = 1/11; M = 0/12		F = 1/15; M = 1/16		F = 8/35; M = 2/25
Carcinoma	0/7	1/23 (4.3%)	0/8	4/31 (12.9%)	0/20	12/60 (20%)
		F = 1/11; M = 0/12		F = 3/15; M = 1/16		F = 8/35; M = 4/25
Adrenal glands						
Nodular hyperplasia	0/9	2/23 (8.7%)	0/11	7/31 (22.6%)	0/21	5/61 (8.2%)
Adenoma	0/9	3/23 (13%)	0/11	4/31 (12.9%)	0/21	17/61 (27.8%)
Carcinoma	0/9	0/23		0/31	0/21	11/61 (18%)
Testis Leydig cells						
Hyper/dysplasia	0/5	9/12 (75%)	1/7 (14.3%)	5/17 (29.4%)	0/9	2/25 (8%)
Tumor	0/5	3/12 (25%)	0/7	10/17 (58.8%)	1/9 (11.1%)	22/25 (88%)
Sex-cord stromal cells						
Tumor	0/4	0/9	0/5	5/16 (31.2%)	0/13	14/28 (50%)
Thyroid glands						
Hyper/dysplasia	0/9	0/23	0/12	0/36	0/22	4/61 (6.5%)
Tumor	0/9	0/23	0/12	0/36	0/22	4/61 (6.5%)
Mammary glands						
Carcinoma	N.D.	N.D.	N.D.	N.D.	0/13	3/36 (8.3%)

1.6.3 Xenograft models

Xenograft models obtained by injecting tumor cells from different species (e.g. human or rat) into immunodeficient mice have been extensively used in cancer research. These studies can examine the tumorigenic potential of the injected cells and evaluate novel treatment approaches. Many different strains of immunodeficient mice have been generated. One of them is the CD-1® Nude Mouse (Crl:CD1-Foxn1nu, Immunodeficient Outbred) from Charles River. These mice lack a thymus and are unable to produce T-cells. This lack of a functioning immune system allows the implantation of cancer cells into these mice that otherwise would be destroyed. Furthermore, this mouse strain has no fur, and this allows for optimal tumor growth monitoring and enables the use of different imaging techniques.

1.7 Aim of the thesis

NETs are a heterogeneous group of malignancies as they arise in different organs and locations and have a variable clinical behavior. Despite the great efforts that have been made in recent years to gain a better understanding of these tumors, which resulted in better diagnostic possibilities, therapy options are still limited. For both PPGLs and pNETs, surgery is still the main and only curative therapy option [132-135]. In cases where surgery is not an option due to the location of the primary tumor or to the spread to distant organs, novel treatment strategies that can replace surgery or have the potential to be used as pre- or postoperative therapies would be highly beneficial.

The aim of this thesis was to exploit the molecular characteristics of PPGLs and pNETs in order to develop novel targeted treatment options and evaluate their efficacy in clinically relevant models.

The PI3K and the CDK4/6 signaling pathways are essential for cell survival and proliferation. Given their important role in these processes, they are dysregulated in many tumors. As stated above, it has been shown by our group and by others that the PI3K and the CDK4/6 signaling pathways play an important role in NETs, and specifically in PPGLs and pNETs and represent a possible target for cancer therapy.

We hypothesize that the PI3K and the CDK4/6 pathway are essential pathways in the tumorigenesis and progression of PPGLs and pNETs and therefore are promising therapeutic targets for cancer therapy. Moreover, combining drugs that target these two pathways might result in increased treatment response, thereby allowing the use of lower doses to reduce the side effects. The results of this thesis could lead to novel therapeutic options for patients with PPGLs and pNETs.

2. Materials and Methods

2.1 Materials

2.1.1 Instruments

4D-Nucleofector™ System (core and X-unit)	Lonza, Basel, Switzerland
accu-jet®, pipettor	Brand, Weetheim, Germany
Adhesive seal Applicator	3M Deutschland, Neuss, Germany
Agilent 2100 Bioanalyzer	Agilent, Santa Clara, CA, USA
Allegra X15R Centrifuge (Rotor SX4750)	BeckmanCoulter, Brea, CA, USA
Automated immunostainer, Discovery XT	Ventana Medical System, Inc., Tucson, AZ, USA
Axiovert 135, Microscope	Carl Zeiss, Jena, Germany
BX 43, microscope	Olympus, Hamburg, Germany
Cell Freezing Container (Biocision, CoolCell)	Brooks Life Sciences, Griesheim, Germany
Centrifuge 5427 R (Rotor FA-45-48-11 5427 R)	Eppendorf, Hamburg, Germany
Centrifuge 5702 (Rotor A-4-38)	Eppendorf, Hamburg, Germany
Centrifuge Heraeus Pico17 (Rotor 75003424)	Thermo Scientific, Waltham, MA, USA
CLSM FluoView FV1200, microscope	Olympus, Hamburg, Germany
Countess II Cell Counter	Invitrogen, Darmstadt, Germany
Cryostat CM3050 S	Leica, Wetzlar, Germany
Dispenser Multipette® plus	Eppendorf, Hamburg, Germany
E4 XLS+ Multichannel pipette, 20-200µl	Mettler Toledo, Gießen, Germany
Eppendorf 5415D, centrifuge	Eppendorf, Hamburg, Germany
EVOS xl, microscope	Thermo Fischer Scientific, Langenselbold, Germany
Finnpipette™ Multichannel pipette 50-300µl	Thermo Fischer Scientific, Langenselbold, Germany
Freezer -20°C Liebherr Comfort	Liebherr, Biberach an der Riss, Germany
Freezer -80°C TSX Series	Thermo Scientific, Waltham, MA, USA

Fridge +4°C Liebherr Premium	Liebherr, Biberach an der Riss, Germany
Fuego SCS basic gas burner	WLD-TEC, Göttingen, Germany
Gel Documentation System	Vilber Lourmat, Eberhardzell, Germany
GeneAmp™ PCR System 9700, PCR cycler	Applied Biosystems, Darmstadt, Germany
gentleMACS Octo Dissociator with heaters	Milteny Biotec, Bergisch Gladbach, Germany
GFL Shaking Water Bath 1083	G. f. Labortechnik, Burgwedel, Germany
Heraeus Instruments, Osterode, Germany	Thermo Fischer Scientific, Waltham, MA, USA
Heraeus Instruments, Osterode, Germany	Thermo Fischer Scientific, Waltham, MA, USA
HERAsafe KS sterile hood	Thermo Scientific, Waltham, MA, USA
Ice Machine	Ziegra, Isernhagen, Germany
Incubator HERAcell 240 i	Thermo Scientific, Waltham, MA, USA
Incubator Innova CO-170	New Brunswick Sci., Edison, NJ, USA
Incubator shaker Model G25	New Brunswick Sci., Edison, NJ, USA
Infinite M200 plate reader	Tecan, Crailsheim, Germany
inoLab pH Level 1, pH-meter	WTW, Weilheim, Germany
L29, test-tube rotator	A. Hartenstein, Würzburg, Germany
Laser Capture Microdissection BCA DM6000 B	Leica, Wetzlat, Germany
Light Microscope MFA33500	Nikon, Minato, Japan
LUNA™ Automated Cell Counter	Logos Biosystems, Waltham, MA, USA
Magnetic stir bars, various sizes	NeoLab, Heidelberg, Germany
Magnetic stirrer MR2000	Heidolph Instr., Schwabach, Germany
Mastercycler X50	Eppendorf, Hamburg, Germany
Maxwell 16	Promega, Mannheim, Germany
Microplate Reader Model 680	BioRad Lab., Munich, Germany
Microplate Reader Varioscan™ LUX	Thermo Fischer Scientific, Langenselbold, Germany
MilliQ water purification system	Sigma-Aldrich, Steinheim, Germany
Mini Trans-Blot® Electrophoretic Transfer Cell	BioRad Lab., Munich, Germany

Mini-Sub® Cell GT System	BioRad Lab., Munich, Germany
Model 200/2.0 Electrophoresis Power Supply	BioRad Lab., Munich, Germany
MSC-Advantage™ Class II Biological Safety Cabinet	Thermo Fischer Scientific, Waltham, MA, USA
Nalgene® Mr. Frosty® Cryo 1°C Freezing Container	Thermo Fischer Scientific, Rosklide, Denmark
NanoDrop™ 2000,spektrophotometer	Thermo Fischer Scientific, Langenselbold, Germany
Nano-Drop™ ND-1000, spektrophotometer	Thermo Fischer Scientific, Langenselbold, Germany
PIPETBOY acu, pipettor	Integra Biosciences, Fernwald, Germany
PIPETBOY Easypet 3	Eppendorf, Hamburg, Germany
Pipetman Classic P10, 1-10 µl, pipette	Gilson, Limburg-Offheim, Germany
Pipetman Classic P100, 20-100 µl, pipette	Gilson, Limburg-Offheim, Germany
Pipetman Classic P1000, 200-1000 µl, pipette	Gilson, Limburg-Offheim, Germany
Pipetman Classic P2, 0,2-2 µl, pipette	Gilson, Limburg-Offheim, Germany
Pipetman Classic P20, 2-20 µl, pipette	Gilson, Limburg-Offheim, Germany
Pipetman Classic P200, 50-200 µl, pipette	Gilson, Limburg-Offheim, Germany
Pipetus®-akku, pipettor	Hirschmann Laborg., Eberstadt, Germany
PowerPac™ 300, Power Supply	BioRad Lab., Munich, Germany
Pressure cooking pot tender cooker	Nordic Ware, Frankfurt, Germny
Privileg 1034 HGD, Microwave	Otto, Hamburg, Germany
QuantStudio 7 Flex	Applied Biosystems, Darmstadt, Germany
Quietek CO2 indcution system QTK1	Nextadvance, NY, USA
Rainin Pipet-Lite XLS+ Multichanel pipette	Mettler Toledo, Gießen, Germany
Research plus Single-Channel Pipette, Blue; 100-1000 µL	Eppendorf, Hamburg, Germany
Research plus Single-Channel Pipette, Gray; 0.5-10 µL	Eppendorf, Hamburg, Germany
Research plus Single-Channel Pipette, Yellow; 10-100 µL	Eppendorf, Hamburg, Germany

Research plus Single-Channel Pipette, Yellow; 20-200 µL	Eppendorf, Hamburg, Germany
Research plus Single-Channel Pipette, Yellow; 2-20 µL	Eppendorf, Hamburg, Germany
Sartorius Universal U3100D, scale	Sartorius, Götttingen, Germany
SW21, water bath shaker	Julabo Labortechnik, Burgwedel, Germany
Thermomixer® comfort 1.5mL, heating block	Eppendorf, Hamburg, Germany
Thermomixer® compact 1.5mL, heating block	Eppendorf, Hamburg, Germany
ThermoStat™ plus 1,5mL, heating block	Eppendorf, Hamburg, Germany
T-Personal Thermocycler, PCR cycler	Biometra, Göttingen, Germany
Trans-Blot Turbo Transfer System	Bio-Rad, Hercules, CA, USA
Tweezers No.5	A. Dumont&Fils, Montignez, Switzerland
UM 300, universal oven	Memmert, Schwabach, Germany
Uniflow UVUB 1800, hood	UniEquip, Planegg, Germany
Unitwist RT, rocking table shaker	UniEquip, Planegg, Germany
Variofuge 3.0R, centrifuge (Rotor 8074)	Heraeus Sepatech, Osterode, Germany
Vortex-Genie 2, vortexer	Scientific Industries, Bohemia, NY, USA
Whirlpool ProMicro 825, microwave	Bauknecht Hausg., Stuttgart, Germany
XCell SureLock™ Mini-Cell Electrophoresis System	Invitrogen, Darmstadt, Germany
X-ray cassette	Carl Roth, Karlsruhe, Germany

2.1.2 Consumables

Adhesive seal films MicroAMPTM	Applied Biosystems, Darmstadt, Germany
Agilent RNA 6000 Pico Kit	Agilent, Santa Clara, CA, USA
Arcturus PEN Membrane Glass slides	Applied Biosystems, Life Technologies, Foster City, CA, USA
Amersham™ Hybond™-ECL, Membrane for western blotting	GE Healthcare, Munich, Germany
Amersham™ Hyperfilm™-ECL, photographic film	GE Healthcare, Munich, Germany
Arcturus PENMembrane Glass Slides	Applied Biosystems, Foster City, CA, USA
Blotting paper grade 3m/N 65g/m2	Munktell&Filtrak, Bärenstein, Germany
Cell Counting Chamber Countess	Thermo Fischer Scientific, Waltham, MA, USA
Cell culture inserts for 24-well plates, 8.0µm pores, transparent PET membrane, BD BioCoat™	BD Biosciences, Heidelberg, Germany
Cell culture microplate 96 well, PS, F-bottom, white	Greiner BioOne, Frickenhausen, Germany
CELLSTAR®, serological pipettes 10mL	Greiner BioOne, Frickenhausen, Germany
CELLSTAR®, serological pipettes 25mL	Greiner BioOne, Frickenhausen, Germany
CELLSTAR®, serological pipettes 5mL	Greiner BioOne, Frickenhausen, Germany
Combitips® for Multipette® 12.5mL	Eppendorf, Hamburg, Germany
Corning® syringe filters, Nylon membrane, pore size 0.45 µm	Sigma-Aldrich, Steinheim, Germany
Coverslips 12mm round	Carl Roth, Karlsruhe, Germany

Cryogenic vials sterile 2mL freestanding Falcon™	BD Biosciences, Heidelberg, Germany
Falcon® 12-well Clear Flat Bottom TC-treated Multiwell Cell Culture Plate, sterile	Corning, Corning, NY, USA
Falcon® 24-well Clear Flat Bottom TC-treated Multiwell Cell Culture Plate, sterile	Corning, Corning, NY, USA
Falcon® 6-well Clear Flat Bottom TC-treated Multiwell Cell Culture Plate, sterile	Corning, Corning, NY, USA
Falcon® 96-well Clear Flat Bottom TC-treated Multiwell Cell Culture Plate, sterile	Corning, Corning, NY, USA
Falcon® reaction tubes Blue Max 15mL	BD Biosciences, Heidelberg, Germany
Falcon® reaction tubes Blue Max 50mL	BD Biosciences, Heidelberg, Germany
Falcon™ Cell Culture Inserts PET track-etched membrane (8 µm pore size)	BD Biosciences, Heidelberg, Germany
Gel cassettes 1.5mm	Life Technologies, Carlsbad, Germany
gentleMACS C Tubes	Milteny Biotec, Bergisch Gladbach, Germany
gentleMACS M Tubes	Milteny Biotec, Bergisch Gladbach, Germany
Glass slides SuperFrost® 76x26mm	Carl Roth, Karlsruhe, Germany
Hanging drop system IPS-06-010	InSphero, Schlieren, Switzerland
MACS Smart Strainer 70µM	Milteny Biotec, Bergisch Gladbach, Germany
Microplates, TC well, clear bottomed, white walled	Lonza, Basel, Switzerland
Millex® syringe-driven filter unit 0.22µm	Merck, Darmstadt, Germany
Nitrocellulose membrane	Bio-Rad, Hercules, CA, USA
NORM-Ject Tuberkulin 1ml	HENKE SASS WOLF, Tuttlingen, Germany

Novex WedgeWell 10% Tris-Glycine Gel	Invitrogen, Thermo Fischer Scientific, Waltham, MA, USA
Omnifix® syringe, single-use 50mL	B. Braun, Melsungen, Germany
Parafilm®	Carl Roth, Karlsruhe, Germany
Pasteur pipettes glass 3.2mL	Carl Roth, Karlsruhe, Germany
PCR SingleCap 8er-SoftStripes 0.1ml	Biozym Sci Hessisch Oldendorf, Germany
PCR tube stripes 0,2mL	Eppendorf, Hamburg, Germany
Petri dishes 100 * 15, 56.7cm2 Nunclon™ Δ	Nunc, Rosklide, Germany
pH indicator stripes	Merck, Darmstadt, Germany
Rainin Bioclean-Tips, Pipette tips	Mettler Toledo, Gießen, Germany
Reaction tubes 1.5mL	Eppendorf, Hamburg, Germany
Reaction tubes 2mL	Eppendorf, Hamburg, Germany
Reaction tubes, RNase free 1.5mL	Zymo Research, Freiburg, Germany
Scalpel, sterile, disposable	Aesulap, Tuttlingen, Germany
Sterican 30G needles	B.Braun, Melsungen, Germany
Sterican 26G needles	B.Braun, Melsungen, Germany
Sterican 24G needles	B.Braun, Melsungen, Germany
Thermo-Fast® PCR plates (0,2mL), 96-well, non-skirted	Abgene/Thermo Scientific, Rockford, IL, USA
TipOne® graduated filter tips, pipette tips, 0,1-10µl	Starlab, Ahrensburg, Germany
TipOne® graduated filter tips, pipette tips, 101-1000µl	Starlab, Ahrensburg, Germany
TipOne® graduated filter tips, pipette tips, 1-100µl	Starlab, Ahrensburg, Germany
TipOne® graduated filter tips, pipette tips, 1-200µl	Starlab, Ahrensburg, Germany
TipOne® graduated filter tips, pipette tips, 1-20µl	Starlab, Ahrensburg, Germany
Tissue culture flask 175cm2, filter cap	Greiner BioOne, Frickenhausen, Germany
Tissue culture flask 25cm2, filter cap	Greiner BioOne, Frickenhausen, Germany

Tissue culture flask 75cm2, filter cap	Greiner BioOne, Frickenhausen, Germany
Tissue culture plates 6-well Nunclon™ Δ	Nunc, Rosklide, Germany
Trans-Blot Turbo Midi-size Transfer Stacks	Bio-Rad, Hercules, CA, USA
ULA plates 7007	Corning, Amsterdam, Netherlands

2.1.3 Chemicals, reagents and kits

Agarose LE for gel electrophoresis	Biozym, Hessisch-Oldendorf, Germany
Albumin bovine Fraction V, Protease-free	Serva, Heidelberg, Germany
Ammonium Persulfate (APS) >98%	Sigma-Aldrich, Steinheim, Germany
Ampicilin sodium salt	Sigma-Aldrich, Steinheim, Germany
Ampuwa® water	Fresenuis KABI, Bad Homburg, Germany
Antibody Dilutent	Dako/Agilent, Santa Clara, CA, USA
BKM120	MedChemExpress, Monmouth Junction, NJ, USA
Blotting-Grade Blocker	BioRad Lab., Munich, Germany
Bovine Serum Albumin	Sigma-Aldrich, Steinheim, Germany
Butane Campinggaz® CV360	CampingGaz, Hungen-Inheiden, Germany
Calcium chloride	Carl Roth, Karlsruhe, Germany
Caspase-Glo 9 Assay System	Promega, Madison, WI, USA
Chloroform, min. 99% p.a.	Merck, Darmstadt, Germany
Citrate Buffer pH 6.0	Abcam, Cambridge, UK
Collagen from human placenta	Sigma-Aldrich, Steinheim, Germany
Collagenase P	Roche Diagnostics, Mannheim, Germany
Corning® BioCoat™ Matrigel® Invasion Chambers with 8.0 µm	Corning, Amsterdam, Netherlands
Corning® BioCoat™ Matrigel® Control Insertswith 8.0 µm	Corning, Amsterdam, Netherlands
Cresyl-Violett	Sigma-Aldrich, Steinheim, Germany
Cycloheximide 98 %	Sigma-Aldrich, Steinheim, Germany
CyQUANT NF Kit	Thermo Fischer Scientific, Waltham, MA, USA
D-(+)-Glucose	Sigma-Aldrich, Steinheim, Germany
DCS LabLine antibody dilutent	DCS, Hamburg, Germany
DMEM + GlutaMAX™, 4.5g/L D-glucose, pyruvate	Gibco, Thermo Fischer Scientific, Waltham, MA, USA

DMSO	Sigma-Aldrich, Steinheim, Germany
dNTP Mix 10mM each	Fermentas, St. Leon-Rot, Germany
DTT 0.1M	Fischer Scientific, Schwerte, Germany
EDTA >99% p.a.	Carl Roth, Karlsruhe, Germany
Eosin Y alcoholic solution	Bio-Optica, Milano, Italy
Epoxomicin	Enzo Life Sciences GmbH, Lörrach, Germany
Ethanol, ASC, ISO	Merck, Darmstadt, Germany
Ethidium bromide	Sigma-Aldrich, Steinheim, Germany
Fast Advanced Master Mix	Thermo Fischer Scientific, Waltham, MA, USA
FBS, Qualified, HI	Gibco, Thermo Fischer Scientific, Waltham, MA, USA
First strand buffer 5x	Fischer Scientific, Schwerte, Germany
Formaldehyde 35 wt. % in H2O	Sigma-Aldrich, Steinheim, Germany
Formalin ROTI Histofix 4%	Carl Roth, Karlsruhe, Germany
Fungizone™	Fischer Scientific, Schwerte, Germany
G153 A and B, photographic developer	Agfa Healthcare, Mortsel, Belgium
G354, photographic fixer	Agfa Healthcare, Mortsel, Belgium
Gel loading dye, 6x	New England Biolabs, Frankfurt, Germany
GeneChip Rat Gene 1.0 ST Array	Thermo Fischer Scientific, Waltham, MA, USA
Glycerol >99%	Sigma-Aldrich, Steinheim, Germany
Goat Serum	PAA, Pasching, Germany
GoTAq Colorless Master Mix	Promega, Madison, WI, USA
Ham's F-10 Nutrient Mix	Gibco, Thermo Fischer Scientific, Waltham, MA, USA
Ham's F-12K (Kaighn's) Medium	Gibco, Thermo Fischer Scientific, Waltham, MA, USA
HBSS 1x 14175-053	Gibco, Thermo Fischer Scientific, Waltham, MA, USA

Hematoxylin Solution (Mayer's Modified)	Abcam, Cambridge, UK
HEPES	Gibco, Thermo Fischer Scientific, Waltham, MA, USA
High-Capacity RNA-to-cDNA Kit	Thermo Fischer Scientific, Waltham, MA, USA
Hoechst 33258 bisBenzimide	Sigma-Aldrich, Steinheim, Germany
Horse Serum, HI	Gibco, Thermo Fischer Scientific, Waltham, MA, USA
Hydrochloric acid 1M	Sigma-Aldrich, Steinheim, Germany
Hydrochloric acid 5M	Neo-Lab, Heidelberg, Germany
Hydrogen peroxide 30%	Merck, Darmstadt, Germany
Isopropanol, ACS, ISO	Merck, Darmstadt, Germany
Kanamycin A monosulfate	Sigma-Aldrich, Steinheim, Germany
Laemmli sample buffer 1x	BioRad Lab., Munich, Germany
LEE011	MedChemExpress, Monmouth Junction, NJ, USA
Lipofectamine™ 2000 transfection reagent	Invitrogen, Darmstadt, Germany
Lipofectamine™ 3000 transfection reagent	Invitrogen, Darmstadt, Germany
Magnesium sulfate 7-hydrate	AppliChem, Darmstadt, Germany
Matrigel 356237	Corning, Amsterdam, Netherlands
Methanol, ACS, ISO	Merck, Darmstadt, Germany
Milk powder, blotting grade	Carl Roth, Karlsruhe, Germany
Mounting medium for ICH Aqueous	Abcam, Cambridge, UK
Novex Tris-Glycine SDS Running Buffer 10x	Invitrogen, Thermo Fischer Scientific, Waltham, MA, USA
NP-40 Tergitol®	Sigma-Aldrich, Steinheim, Germany
Opti-MEM® reduced serum media	Gibco, Thermo Fischer Scientific, Waltham, MA, USA
Oviation Pico WTA System V2	Nugen, Redwood City, CA, USA
Paraformaldehyde solution 4% in PBS	Thermo Fischer Scientific, Waltham, MA, USA

PBS solution, sterile 14190-094	Gibco, Thermo Fischer Scientific, Waltham, MA, USA
PBS powder pH 7.4	Sigma-Aldrich, Steinheim, Germany
PCR Mycoplasma Test Kit I/C	PromoKine, PromoCell, Heidelberg, Germany
PEG300	Sigma-Aldrich, Steinheim, Germany
Penicilin-Streptomycin	Gibco, Thermo Fischer Scientific, Waltham, MA, USA
PhosTOP	Roche Diagnostics, Mannheim, Germany
Pierce BCA Protein Assay Kit	Thermo Fischer Scientific, Waltham, MA, USA
Ponceau S, practical grade	Sigma-Aldrich, Steinheim, Germany
Potassium chloride	Carl Roth, Karlsruhe, Germany
Potassium dihydrogenphosphat	Carl Roth, Karlsruhe, Germany
ProLong Gold antifade reagent	Invitrogen, Thermo Fischer Scientific, Waltham, MA, USA
Protease inhibitor cocktail tablets complete mini	Roche Diagnostics, Mannheim, Germany
Quick-Load 100bp DNA ladder	New England Biolabs, Frankfurt, Germany
Rat Tail Collagen Solution	Sigma-Aldrich, Steinheim, Germany
Real Time Glo Annexin V Apoptosis and Necrosis Assay	Promega, Madison, WI, USA
Real Time Glo MT Cell Viability Assay	Promega, Madison, WI, USA
Recovery Cell Culture Freezing Medium	Gibco, Thermo Fischer Scientific, Waltham, MA, USA
Red Blood Cell Lysis Buffer	Sigma-Aldrich, Steinheim, Germany
Restore™ PLUS, stripping buffer for western blot	Gibco, Thermo Fischer Scientific, Waltham, MA, USA
RIPA buffer	Sigma-Aldrich, Steinheim, Germany
RNaseZAP®	Sigma-Aldrich, Steinheim, Germany
RNeasy Micro Kit	Qiagen, Hilden, Germany

RNeasy Mini Kit	Qiagen, Hilden, Germany
Roti®-Stock 10x TBS	Carl Roth, Karlsruhe, Germany
RPMI 1640 + GlutaMAX™	Gibco, Thermo Fischer Scientific, Waltham, MA, USA
SDS 10% (w/v) solution	BioRad Lab., Munich, Germany
SDS-PAGE running buffer Rotiphorese®, 10x	Carl Roth, Karlsruhe, Germany
Sodium Azide >99%	Sigma-Aldrich, Steinheim, Germany
Sodium bicarbonate	Carl Roth, Karlsruhe, Germany
Sodium chloride >99.5%	Merck, Darmstadt, Germany
SuperSignal® West Femto, chemiluminescent substrate	Thermo Fischer Scientific, Darmstadt, Germany
SuperSignal® West Pico PLUS, chemiluminescent substrate	Thermo Fischer Scientific, Darmstadt, Germany
TaqMan® FastAdvanced Master Mix	Thermo Fischer Scientific, Waltham, MA, USA
TBE Tris/Boric Acid/EDTA, 10x	BioRad Lab., Munich, Germany
TBS-T, 10x	Carl Roth, Karlsruhe, Germany
TEMED 99%	Amresco, Solon, OH, USA
Toluidine blue	Sigma-Aldrich, Steinheim, Germany
Triton X-100, >10% in H2O	Sigma-Aldrich, Steinheim, Germany
Trizma® base	Sigma-Aldrich, Steinheim, Germany
TRIzol® reagent	Gibco, Thermo Fischer Scientific, Waltham, MA, USA
Trypan Blue solution 0.4%	Sigma-Aldrich, Steinheim, Germany
Trypsin, 0.05% with EDTA	Gibco, Thermo Fischer Scientific, Waltham, MA, USA
Tumor Dissociation Kit, human 130-095-929	Milteny Biotec, Bergisch Gladbach, Germany
Tumor Dissociation Kit, mouse 130-096-730	Milteny Biotec, Bergisch Gladbach, Germany
Tween 20	Carl Roth, Karlsruhe, Germany

Ultra Sensitive Insulin ELISA Kit	CrystalChem, Zaandam, Netherlands
VECTASHIELD® mounting medium	BIOZOL Diagnostica, Eching, Germany
Xylol >99%	Merck, Darmstadt, Germany
1-methyl-2-pyrrolidone	Sigma-Aldrich, Steinheim, Germany
2-mercaptoethanol >99% BioUltra	Sigma-Aldrich, Steinheim, Germany
2-mercaptoethanol 50mM	Gibco, Thermo Fischer Scientific, Waltham, MA, USA

2.2 Methods

2.2.1 Animals

2.2.1.1 Licensing

All animal experiments were performed in accordance with guidelines approved by the Government of Upper Bavaria, Germany. License numbers ROB-55.2-2532.Vet_02-16-117 and ROB-55.2-2532.Vet_02-15-11 were used for breeding MENX rats and MEN1 mice and for performing in vivo experiments.

To work with animals, I took internal training courses offered by the Helmholtz Zentrum München. Additionally, I hold certificates in animal handling and science basic and advanced courses (FELASA C).

2.2.1.2 Husbandry

Animals were kept in the animal facility in a controlled environment with 12 hours light and dark cycle at 22°C. Littermates were housed together (maximum of four mice or two rats per cage) and identified by ear punches. All animals were fed with a standard chow diet unless otherwise stated.

2.2.1.3 Organ withdrawal

Animals were euthanized by CO_2 inhalation for 5 minutes using a Quietek CO_2 Induction Systems (nextadvance, #QTK1) according to animal welfare regulation. Death was ensured by cervical dislocation or final blood withdrawal. Weight of animals and organs was taken, and blood for plasma was withdrawn directly from the vena cava if needed.

2.2.1.4 Tissue processing

For primary cell culture, tissues were dissected, weight was taken, and the tissue was placed in HBSS on ice. Otherwise, desired tissue was either snap-frozen in liquid nitrogen and later stored at -80°C or collected in formalin (ROTI®Histofix 4 %) for future analysis. Tissue was removed from formalin after 48h and either embedded in FFPE blocks or given in a storage solution (PBS + 0.1% NaN_3) for further storage.

2.2.1.5 MENX

The following rats were used in this theses:

Table 3: Rats used in the thesis

Rat No.	Gender	Age (mo)	Genotype	Used for
16/2193	M	17,0	wt/mut	Arrays
17/304	M	18,0	wt/mut	Arrays
17/35	F	18,5	wt/mut	Arrays
16/1968	M	18,5	wt/mut	Arrays
17/604	F	18,5	wt/mut	Arrays
17/193	F	20,0	wt/mut	Arrays
17/1092	M	20,0	wt/mut	Arrays
11/1538	F	23,0	wt/mut	Arrays
19/55	M	7,5	mut/mut	Primary cell culture
19/56	F	8,5	mut/mut	Primary cell culture
19/57	F	9,0	mut/mut	Primary cell culture
19/58	F	9,0	mut/mut	Primary cell culture
19/132	F	8,5	mut/mut	Primary cell culture
19/134	M	8,0	mut/mut	Primary cell culture
19/215	F	8,0	mut/mut	Primary cell culture
19/216	M	8,0	mut/mut	Primary cell culture
19/217	M	8,0	mut/mut	Primary cell culture

Genotyping of MENX rats

Genomic DNA isolated was amplified from rat ear clips, and the following primers were used to amplify targets by end-point PCR:

Fwd: CAA AAC AAA AGG GCC AAC AG

Rev: CCA GCT AGG GTG TCA GTT TTG

For genotyping, 25µl per reaction of GoTAq Colourless Master Mix (Promega) was used. 12 µl of Master Mix, 0.1µM of forward and reverse primers, and 2 µl of DNA template were used. The reaction mixture was placed into an Eppendorf® Mastercycler X50i (Eppendorf) with the following instructions:

Temperature [°C]	**Time [min]**	**cycles**
98	3:00	1
98	00:30	15
65 – 0.5/cycle	00:30	
72	2:00	
98	00:30	20
55	00:30	
72	2:00	
72	5:00	1
4	end	

The so obtained samples were run on a 2% agarose gel together with Quick-Load® 100 bp DNA Ladder (New England Biolabs, Frankfurt, Germany). The results were qualitatively analyzed by visualization under UV light through a gel documentation system.

2.2.1.6 Men1+/-

The following Men1 mice were used in this thesis.

Table 4: Men1 mice used in the thesis

Mouse No.	Gender	Age (mo)	Genotype
19/197	M	20	wt/mut
19/198	M	20	wt/mut
19/199	M	20	wt/mut
20/169	M	23	wt/mut
20/190	F	22	wt/mut
20/191	F	22	wt/mut
20/192	F	22	wt/mut
20/193	F	21	wt/wt
20/194	F	21	wt/wt
21/2	M	18	wt/mut
21/3	F	18	wt/mut
21/12	M	18	wt/wt
21/13	M	18	wt/wt
21/14	M	18	wt/wt
21/15	M	18	wt/wt

Genotyping of Men1 mice

Genomic DNA isolated was amplified from rat ear clips, and the following primers were used to amplified targets by end-point PCR:

Fwd: GGATTCTGCTCCCCAGGC

Rev. CACCTCCATCTTACGGTCG

For genotyping, 25µl per reaction of GoTAq Colourless Master Mix (Promega) was used. 12 µl of Master Mix, 0.1µM of forward and reverse primers, and 2 µl of DNA template were used. The reaction mixture was placed into an Eppendorf® Mastercycler X50i (Eppendorf) with the following instructions:

5 min	94°C	
30 s	94°C	
30 s	55°C	35 cycles
1 min	72°C	
5 min	72°C	

The so obtained samples were run on a 2% agarose gel together with Quick-Load® 100 bp DNA Ladder (New England Biolabs, #N0551). The results were qualitatively analyzed by visualization under UV light through a gel documentation system.

2.2.1.7 CD1® Nude mice

CD1® Nude mice (Crl:CD1-Foxn1nu) were purchased from Charles river with an age of 6 weeks. CD1® Nude mice do not have hair, lack a thymus and do not produce T-cells. Therefore, these immunodeficient mice are a well-known and commonly used model for xenograft studies.

Table 5: CD1 mice used in the thesis

Mouse No.	Gender	Group
20/124	F	control
20/125	F	control
20/126	F	control
20/127	F	control
20/128	F	control
20/129	F	control
20/130	F	control
20/131	F	control
20/132	F	BKM120
20/133	F	BKM120
20/134	F	BKM120
20/135	F	BKM120
20/136	F	BKM120
20/137	F	BKM120
20/138	F	BKM120
20/139	F	BKM120
20/140	F	LEE011
20/141	F	LEE011
20/142	F	LEE011
20/143	F	LEE011
20/144	F	LEE011
20/145	F	LEE011
20/146	F	LEE011

20/147	F	LEE011
20/148	F	BKM120 + LEE011 high
20/149	F	BKM120 + LEE011 high
20/150	F	BKM120 + LEE011 high
20/151	F	BKM120 + LEE011 high
20/152	F	BKM120 + LEE011 high
20/153	F	BKM120 + LEE011 high
20/154	F	BKM120 + LEE011 high
20/155	F	BKM120 + LEE011 high
20/156	F	BKM120 + LEE011 low
20/157	F	BKM120 + LEE011 low
20/158	F	BKM120 + LEE011 low
20/159	F	BKM120 + LEE011 low
20/160	F	BKM120 + LEE011 low
20/161	F	BKM120 + LEE011 low
20/162	F	BKM120 + LEE011 low
20/163	F	BKM120 + LEE011 low

2.2.2 In vivo experiments

2.2.2.1 PC12 Xenograft treatment

For in vivo xenograft treatments, 6 week old CD1® Nude mice were used. After arrival, mice were kept for 2 weeks in the husbandry to adopt.

For xenograft engrafting, mice were injected with $1x10^6$ PC12 cells in a 1:1 mixture of serum and antibiotic-free medium with Matrigel (Corning, #356237). Matrigel was kept on ice until use, and all used materials (syringe, needles, pipette tips) were cooled before use. 100µl of the cell-matrigel mixture was injected into the right flank of each animal.

Cells were resuspended in 50µl of serum-free and antibiotic-free RPMI. The cell solution was briefly mixed with 50µl of Matrigel and immediately injected into the mice. For Xenograft formation, cells were injected s.c. in the right flank.

A total of 40 mice were injected. After two weeks, when tumors reached a volume of 100-150mm^3, tumors were measured by caliper and mice were randomized into five different groups with eight animals per group. For the next 3 weeks, mice were daily treated with vehicle (1 volume of 1-methyl-2-pyrrolidone and 9 volumes of PEG300), BKM120 (25mg/kg), LEE011 (75mg/kg), combination (BKM120 25mg/kg + LEE011 75mg/kg) or combination low dose (BKM120 12.5 mg/kg + LEE011 25 mg/kg). Caliper measurement of tumors was done twice per week. Tumor volume was calculated using the formula tumor volume = 1/2 (length x $width^2$), as described in [136, 137]. After 21 days, mice were euthanized by CO_2. Tumors were measured, weighted and collected for further analysis. Depending on size, tumors were either cut, and one piece was snap-frozen in liquid nitrogen and later stored at -80°C while the other piece was given in formalin for later FFPE embedding. Small tumors were either used for snap freezing or formalin fixation, as displayed in Table 6.

Table 6: Tissues collected in Xenograft study

Mouse No.	Gender	Group	Formalin	-80°C
20/124	F	control	✓	✓
20/125	F	control	✓	✓
20/126	F	control	✓	✓
20/127	F	control	✓	✓
20/128	F	control	✓	✓
20/129	F	control	✓	✓
20/130	F	control	✓	✓
20/131	F	control	✓	✓
20/132	F	BKM120	✓	✓
20/133	F	BKM120	✓	✓
20/134	F	BKM120	✓	✓
20/135	F	BKM120	✓	✓
20/136	F	BKM120	✓	✓
20/137	F	BKM120	✓	✓
20/138	F	BKM120	✓	✓
20/139	F	BKM120	✓	✓
20/140	F	LEE011		
20/141	F	LEE011	✓	✓
20/142	F	LEE011	✓	✓
20/143	F	LEE011	✓	✓
20/144	F	LEE011	✓	✓
20/145	F	LEE011	✓	✓
20/146	F	LEE011	✓	✓
20/147	F	LEE011	✓	✓
20/148	F	BKM120 + LEE011 high	✓	
20/149	F	BKM120 + LEE011 high	✓	✓
20/150	F	BKM120 + LEE011 high	✓	✓
20/151	F	BKM120 + LEE011 high	✓	✓
20/152	F	BKM120 + LEE011 high	✓	✓

20/153	F	BKM120 + LEE011 high	✓	✓
20/154	F	BKM120 + LEE011 high		✓
20/155	F	BKM120 + LEE011 high	✓	✓
20/156	F	BKM120 + LEE011 low	✓	
20/157	F	BKM120 + LEE011 low	✓	✓
20/158	F	BKM120 + LEE011 low	✓	✓
20/159	F	BKM120 + LEE011 low	✓	✓
20/160	F	BKM120 + LEE011 low	✓	✓
20/161	F	BKM120 + LEE011 low	✓	✓
20/162	F	BKM120 + LEE011 low	✓	✓
20/163	F	BKM120 + LEE011 low	✓	✓

2.2.3 Primary Cell culture

2.2.3.1 Animal tissue handling

Animals were sacrificed using CO_2 in compliance with animal welfare standards. Organs were directly removed and put on ice in HBSS (gibco, #14175-053) in case of adrenals and paraganglioma or islet cell isolation was performed as described below.

2.2.3.2 Human tissue handling

The tumor samples were isolated immediately following tumor removal surgery. Each sample was placed into a falcon filled with PBS (gibco, #14190-094) solution and put into a cooling box for transport. Tissues were obtained in collaboration with clinical partners at LMU.

2.2.3.3 Adrenals

The tissue was cleared of blood with PBS (gibco, #14190-094). Primary cell isolation was carried out by using the gentleMACS™ Octo Dissociator with Heaters (Miltenyi Biotec, Germany) with the Tumor Dissociation Kit, human (#130-095-929, Miltenyi Biotec) for human tissue or the Tumor Dissociation Kit, mouse (#130-096-730, Miltenyi Biotec) for animal tissue following the manufacturer's instructions. The so obtained single-cell suspension was incubated with Red Blood Cell Lysis Buffer (#R7757, Sigma-Aldrich) for 3 min ar RT for red blood cell removal. Cells were then counted as described below and used for downstream applications.
A schematic workflow can be seen in Figure 10.

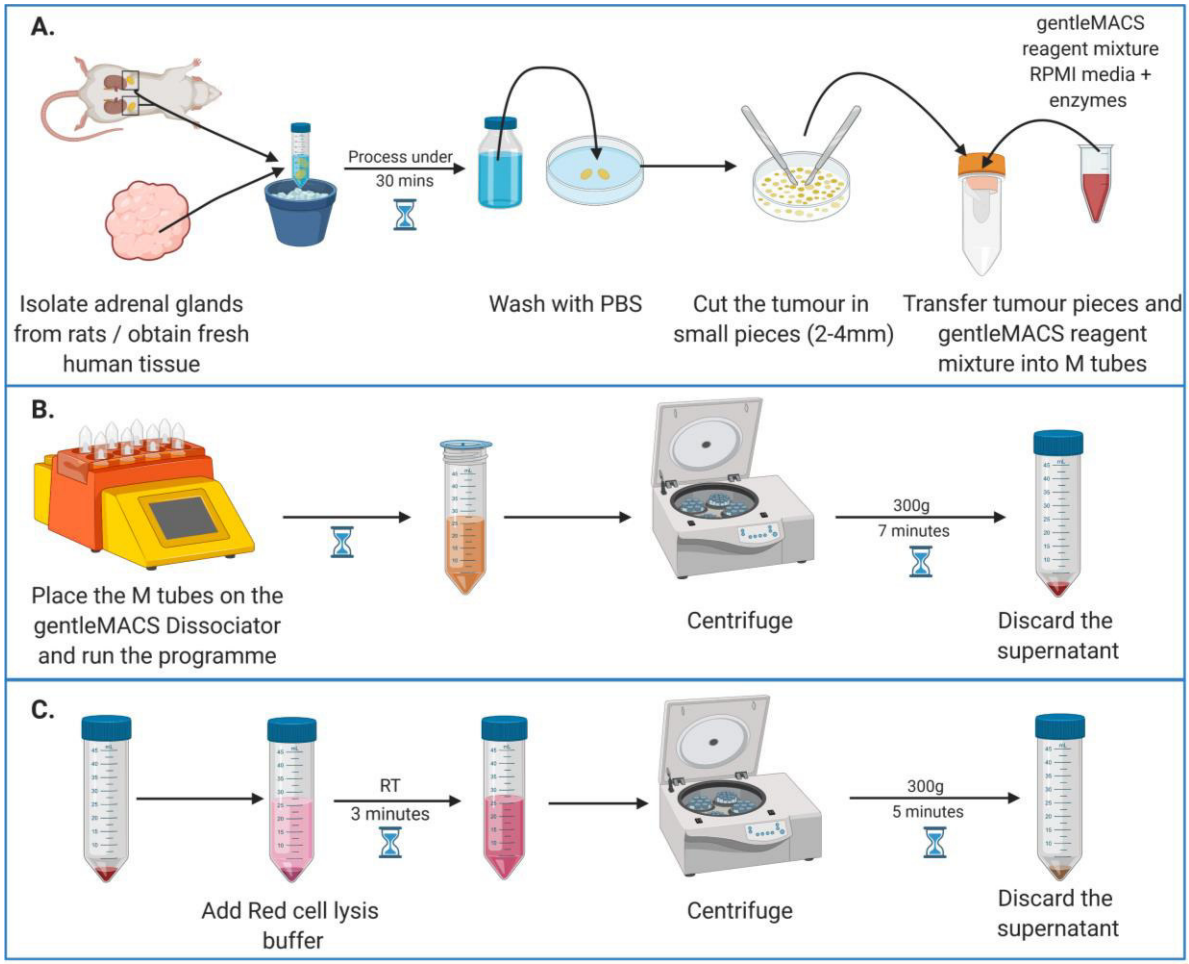

Figure 10: Workflow of adrenal/PPGL primary cell culture
Shown is the schematic workflow of adrenal and PPGL primary cell culture with the isolation of the organs and first preparation steps (A), the isolation of primary cells using GentleMAC Dissociator (B) and the final steps, including red blood cell removal (C). Created with BioRender.com

2.2.3.4 Pancreatic islets

Under a dissecting microscope, the hepato-pancreatic duct was clamped at the ampulla, where it meets the intestine. For mouse islet insolation, the bifurcation where the cystic (coming from the gallbladder) and hepatic ducts meet was located, and 3ml of collagenase P (2U/mg) were injected into the duct to inflate the pancreas. In the case of rats, 10ml of collagenase P (2U/mg) were directly injected into the hepatic duct as rats do not have a gallbladder. Then, omental fat was removed, and the pancreas was carefully dissected. The pancreas was transferred to a cooled 50ml falcon tube containing collagenase and placed on ice.

Collagenase digestion was performed by placing the tubes in a water bath at 37°C for 15 minutes. After 7.5 minutes, samples were shaken by hand for 5s. After 15 minutes, falcons

were removed from the water bath and vigorously shaken for 5s. Tubes were placed on ice and topped up with 20ml cold HBSS (HBSS + BSA 1mg/ml).

Samples were spined down for 2 min at 300g, the supernatant was discarded, and the pellets were carefully resuspended in 15ml HBSS+BSA. The solution was filtered through a strainer (500µM) and centrifuged for 2 min at 300g. Pellet was resuspended in a few ml of HBSS+BSA, and islets were handpicked using a dissection microscope. To obtain a single cell solution, isolated pancreatic islets were incubated in Trypsin for 3-10min until completely dissociated. Cells were counted as described later and used for 3D spheroid generation as described below (2.2.6). A schematic representation of the islet isolation process can be seen in Figure 11.

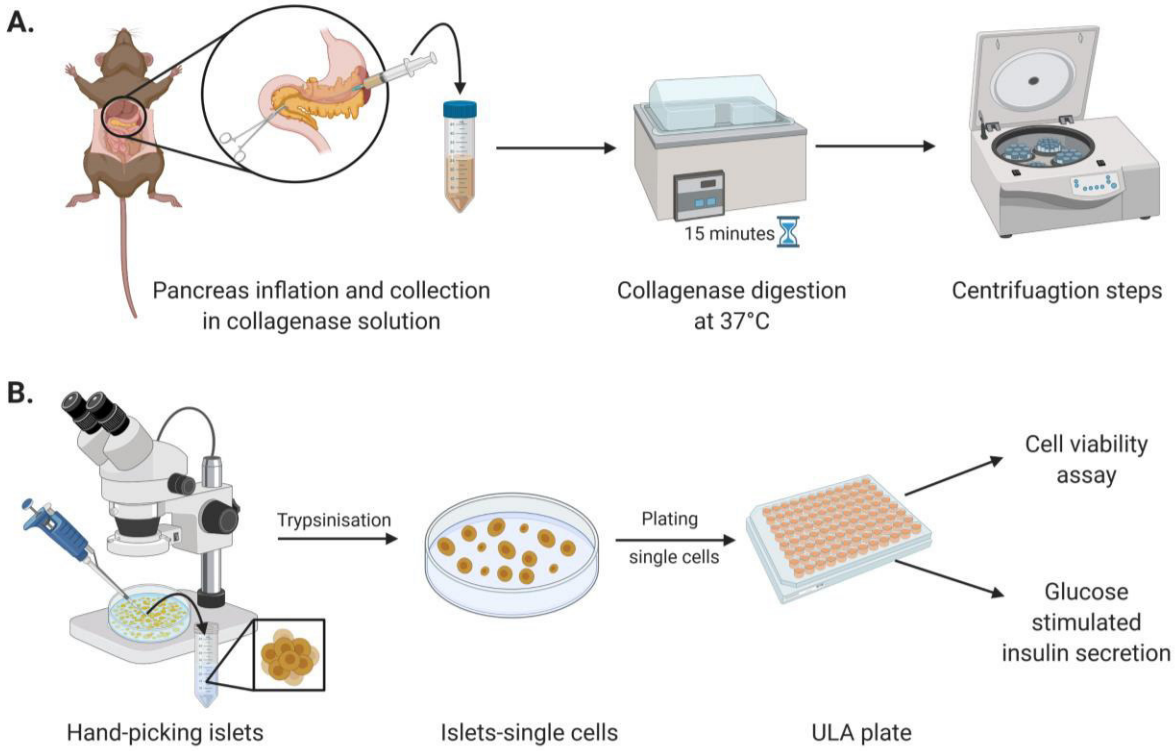

Figure 11: Islet isolation and handling
(A) shows the isolation of islets using Collagenase P injection and digestion at 37°C. (B) shows the process of isolating islets by hand-picking, and plating them for downstream applications. Created with BioRender.com

2.2.4 Human samples

Human pheochromocytoma and paraganglioma tissue was obtained from 6 patients as shown in Table 7.

Table 7: Human PPGL tissue

Tissue obtained on	Patient ID	Weight of tissue [g]
21.01.2020	Pheo 21	1.51
16.03.2020	Pheo 23	0.31
14.05.2020	Pheo 26	0.22
19.08.2020	Pheo 27	1.16
09.09.2020	Pheo 30	2.31
18.11.2020	Pheo 35	0.45

All the patients gave informed consent for this study, and all the procedure was approved by the ethics committee.

2.2.5 Cell culture

2.2.5.1 Sub-culturing

Cells were cultured at 37°C and 5% CO_2 in a humid atmosphere and handled under sterile conditions using sterile hoods with controlled air flow. All solutions that were added to the cells were pre-warmed to RT or in case of media to 37°C before their addition. Sub-culturing of cells was performed on a regular basis to avoid the confluence of cells and cell death. For this purpose, cells were washed with PBS and incubated with 0.05 % trypsin/EDTA for 3 – 5 min at 37 °C. Media with FBS was given to detached cells to inhibit trypsin. Cells were split by a ratio between 1:2 and 1:10 depending on cell line and confluence. Cell lines were routinely cultured in 75 cm2 and 175 cm2 tissue culture flasks, and media were used as described in Table 8. Cells were used for a maximum of 2 months after thawing. Flask for MPC cells were coated with rat collagen (0.1% Collagen solution in 0.01M HCl), flasks for NT3 cells were coated with human placenta collagen (50µg/ml in H_2O). INS-1E and PC12 cells were cultured without coating.

2.2.5.2 Cryopreservation of cells

Cell lines were cryopreserved at early passages and large volumes to ensure consistent handling of cells without changes over time. To this purpose, cells in the log growth phase were pelleted by centrifugation for 5min at 300g. The supernatant was discarded, and the cell pellet was resuspended in culture medium containing 10% dimethyl sulfoxide (DMSO). The cell suspension was aliquoted in 1.5ml cryovials, placed in a Cell Freezing Container (Biocision, Cool-Cell) and stored at -80°C. Long-term storage was carried out in liquid nitrogen.

To thaw cells, cryovials were thawed in a 37°C water bath, and the cell suspension was given into complete culture medium immediately after thawing. After centrifugation at 300g for 5min the cells were resuspended in culture medium and placed in a tissue culture flask.

Cryopreservation for primary cells was done by the same procedure, except the use of Recovery™ Cell Culture Freezing Medium instead of 10% DMSO in medium.

2.2.5.3 Cell counting

Cell pellets were generated as described and resuspended in 500µl-5ml, depending on the pellet size. 10µl of the so-obtained cell suspension were mixed with 10 µl of Trypan Blue (0.4%). 10µl of the cell-Trypan blue mixture were immediately given into a Countess™ Cell Counting Chamber Slide, and cells were counted using the Countess II Automated Cell Counter device. Numbers of total cells, living cells and dead cells were generated by the device.

2.2.5.4 Mycoplasma testing

Cell lines were routinely tested for the presence of mycoplasma. To this end, cell culture supernatant was analyzed by using the PCR Mycoplasma Test Kit I/C (PromoKine, #PK-CA91) and following the manufacturer's instructions. All cell clines used in this thesis were mycoplasma-free.

2.2.5.5 Cell lines

Used cell lines with information about the cells and the used medium is shown in Table 8.

Table 8: Cell lines

Cell line	species	description	Media
PC12	rat	derived from a transplantable rat pheochromocytoma	RPMI1640, GlutaMAX 5% FBS 10% HS 1% Penicillin/Streptomycin
MPC	mouse	derived from an irradiated heterozygous Nf1 knockout mouse pheochromocytoma	RPMI1640, GlutaMAX 5% FBS 10% HS 1% Penicillin/Streptomycin
INS-1E	rat	rat insulinoma cell line, pancreatic beta cell line	RPMI1640, GlutaMAX 5% FBS 1% Penicillin/Streptomycin 1mM Pyruvate 10mM HEPES 50µM 2-Mercaptoethanol
NT3	human	lymph node derived cell line from a male patient with well-differentiated pNET	RPMI1640, GlutaMAX 10% FCS 1% Penicillin/Streptomycin 20ng/ml EGF 10ng/ml FGF 1% L-Glutamine (200mM)

2.2.5.6 Assays

2D cell proliferation

2D cell proliferation was measured using the CyQUANT® NF kit (Thermo Fisher Scientific). Cells were seeded in black wall, clear bottom 96-well plates. 1 day after seeding, cells were treated with the drugs or controls as indicated in the figures. After 72h of treatment, medium was aspirated, and kit reagents were added following the manufacturer's instructions. After 1h incubation at 37°C in the incubator, the fluorescence signal was measured with an excitation wavelength of ~485 nm and an emission wavelength of ~530 nm. Cellular DNA content is hereby measured by quantifying the fluorescence signal.

Caspase 9 assay

Apoptosis was measured by assessing the Caspase 9 activity in treated cells using the Caspase-Glo® 9 Assay System (Promega). Cells were seeded in white-walled 96-well plates. 1 day after seeding, cells were treated with the drugs or controls as indicated in the figures. After 72h of treatment, reagents including MG-132 Inhibitor were added following the manufacturer's instructions. After 1h incubation at RT, luminescence was measured.

2D migration and invasion

2D migration and invasion assays were performed using the using Corning® BioCoat™ Matrigel® Invasion Chambers (invasion) and Corning® BioCoat™ Control Inserts (migration). Both insert types have an 8-micron pore size PET membrane which is covered with a thin layer of Matrigel Basement Membrane Matrix in case of the invasion chambers. The manufacturer's instructions were followed to perform the assay. Briefly, inserts were re-hydrated in medium before use. Then, cells in serum-reduced media were seeded into the inserts and then incubated at 37°C for 1 day. Serum-reduced media was generated by diluting the cell culture media with RPMI1640 Glutamax in a 1:10 ratio. After the incubation, normal cell culture medium supplemented with the drugs for treatment was added to the bottom of the wells. Additionally, the serum-reduced medium was exchanged with serum-reduced medium supplemented with the drugs. After 72h, the non-invading/migrating cells were removed by scrubbing with a cotton swab and invading cells were fixed and stained with 1% Toluidine blue (Sigma). Pictures were taken with the microscope, and the percentage of invasion was calculated.

Table 9: Cell numbers used in 2D cell culture

	Cells per well	
	96 well plate	2D migration and invasion inserts
NT3	1 x 10^5	8 x10^5
INS-1E	1 x 10^4	2.5 x 10^4
PC12	2.5 x 10^3	5 x 10^3
MPC	1 x 10^4	1 x 10^5

2.2.6 3D cell culture

2.2.6.1 General 3D cell culture

Prior to experiment performance, cell lines and primary cells were tested for the formation of 3D spheroids, and the optimal seeding density for each cell line was determined. To this end, 500-2000 cells per cell line or 20000 primary adrenal cells were seeded into one well of a ULA plate (Corning, #7007) or of the hanging drop system (Insphero, #IPS-06-010), respectively. For the spheroid generation from primary pancreatic islet cells, 5000 cells were plated in ULA plates. The formation of spheroids was examined after five days. The size plays a crucial role as it influences the availability of nutrients in the center, the required drug concentration for treatments and consistency is also important for statistical analysis. The optimal seeding densities for the different cell lines are shown below.

Table 10: Cell numbers used in 3D cell culture

	Cells per well
NT3	2000
INS1	1000
PC12	500
MPC	1000

2.2.6.2 3D drug treatments

Cells were plated directly after isolation in the corresponding system as mentioned before. Cells were left in the wells for three to six days to allow spheroid formation. After spheroid formation, cells were treated with drugs for 72h, and the different assays were performed during/after that time. For spheroid size analysis, pictures were taken at the start of the treatment and after 3, 7, 10 and 14 days using a 10x lense on the EVOS xl microscope.

2.2.6.3 3D cell viability

To measure the viability of 3D spheroids, the RealTime-Glo™ MT Cell Viability Assay (#G9712, Promega) assay was used. This assay uses a substrate that diffuses through the cell membrane into the cell where it gets reduced. The reduced substrate diffuses and exits the cell, where it creates a luminescence signal by serving as substrate for the NanoLuc® Luciferase. The substrate's reduction can only be carried out by metabolically active cells, not by dead cells, and the light production is proportional to the number of living cells. This assay is an excellent method to measure cell viability in an ATP-independent matter in a 3D culture system. The assay does not disturb the cells during the measurement and allows for a later use of the spheroids. Assay reagents were added together with the drugs to the cells following the manufacturer's instructions. Cell viability was measured at the start of the treatment and after 24h, 48h and 72h.

A schematic representation of the assay is shown in Figure 12. The assay was used following the manufacturer's instructions, and luminescence measurements were taken on a Varioskan Lux plate reader (Thermo Fisher Scientific).

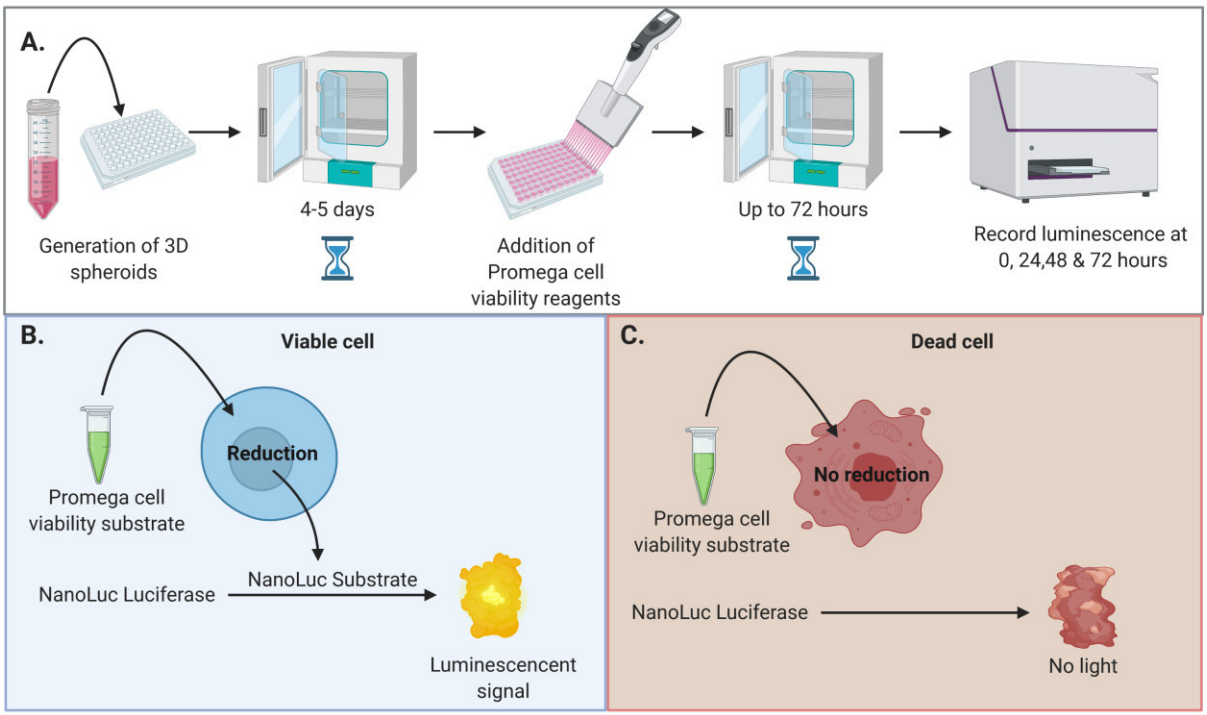

Figure 12: Schematic workflow of 3D cell viability measurements
Shown is the workflow for 3D cell viability including generation of 3D spheroids, start of the assay and luminescence readings (A). Additionally, the assay principle in viable (B) and dead (C) cells is shown. Created with BioRender.com

2.2.6.4 3D Apoptosis measurement

To measure Apoptosis of 3D spheroids, the RealTime-Glo™ Annexin V Apoptosis and Necrosis Assay (Promega, #JA1011) was used. This assays measures Apoptosis by detecting Phosphatidyl Serine on the outer membrane leaflet that gives a Luminescence signal. The assays was used following the manufacturer's instructions, and luminescence measurements were taken on a Varioskan Lux plate reader (Thermo Fisher Scientific). The assay design was the same as for the 3D cell viability and apoptosis was measured after 30h of treatment.

2.2.6.5 Insulin secretion assay

To assess insulin secretion, a glucose-stimulated insulin secretion (GSIS) assay was performed. For this assay spheroids were used that were either treated with drugs as indicated in the experiments or directly generated from primary tissues. The assay was performed in 96-well plates with one spheroid per well. In the following steps, Krebs Ringer Bicarbonate HEPES Buffer(115mM NaCl, 4.7mM KCl, 1.2mM KH_2PO_4, 1.2mM $MgSO_4$, 20mM $NaHCO_3$, 16mM

HEPES, 2.56mM $CaCl_2x2H_2O$, pH7.4, 1g/l BSA (no insulin)) was used and supplied with Glucose as indicated.

First of all, spheroids were washed three times with medium and then starved for 1h in 1mM Glucose. After washing two times with 1mM Glucose, spheroids were incubated for 60min with 2.8mM Glucose (Baseline). Baseline supernatant was collected, spheroids washed two times with 2.8mM Glucose and incubated for 60 min with 16.5mM Glucose (Insulin). Insulin supernatant was collected, and spheroids were washed two times with 16.5mM Glucose. Then, spheroids were incubated for 60 min with 2.8mM Glucose (Glucagon). Glucagon supernatant was collected.

To analyze the amount of secreted insulin, the Baseline and Insulin supernatants were measured using an Ultra Sensitive Insulin ELISA Kit (CrystalChem, #90080) following the manufacturer's instructions.

2.2.7 RNA Isolation

2.2.7.1 RNA extraction from cells

RNA extraction from cells was performed either with the RNeasy Mini Kit (Qiagen, #74104) or the RNeasy Micro Kit (Qiagen, #74004) depending on the number of total cells and according to the manufacturer's protocol. RNA quality and concentration was determined by measuring OD using Nanodrop 2000 (Thermo Fisher Scientific). To assess RNA quality, an A260/280 ratio of 1.8-2.2 and an A260/230 of 2.0-2.2 were used in this study. RNA was stored at −80°C until further use.

2.2.7.2 RNA quality measurement

For RNA extracted via laser microdissection or RNA used in Array or RNAseq applications, in addition to OD measurement RNA quality was assessed by using the Agilent RNA 6000 Pico (Agilent Technologies, #5067-1513) on a 2100 Bioanalyzer Instrument (Agilent Technologies, # G2939BA). With this kit, an RNA integrity number (RIN) was determined. RNA samples with a RIN number above seven were considered good quality and were used for downstream applications. The RIN numbers of samples used in this thesis are shown in Figure 13.

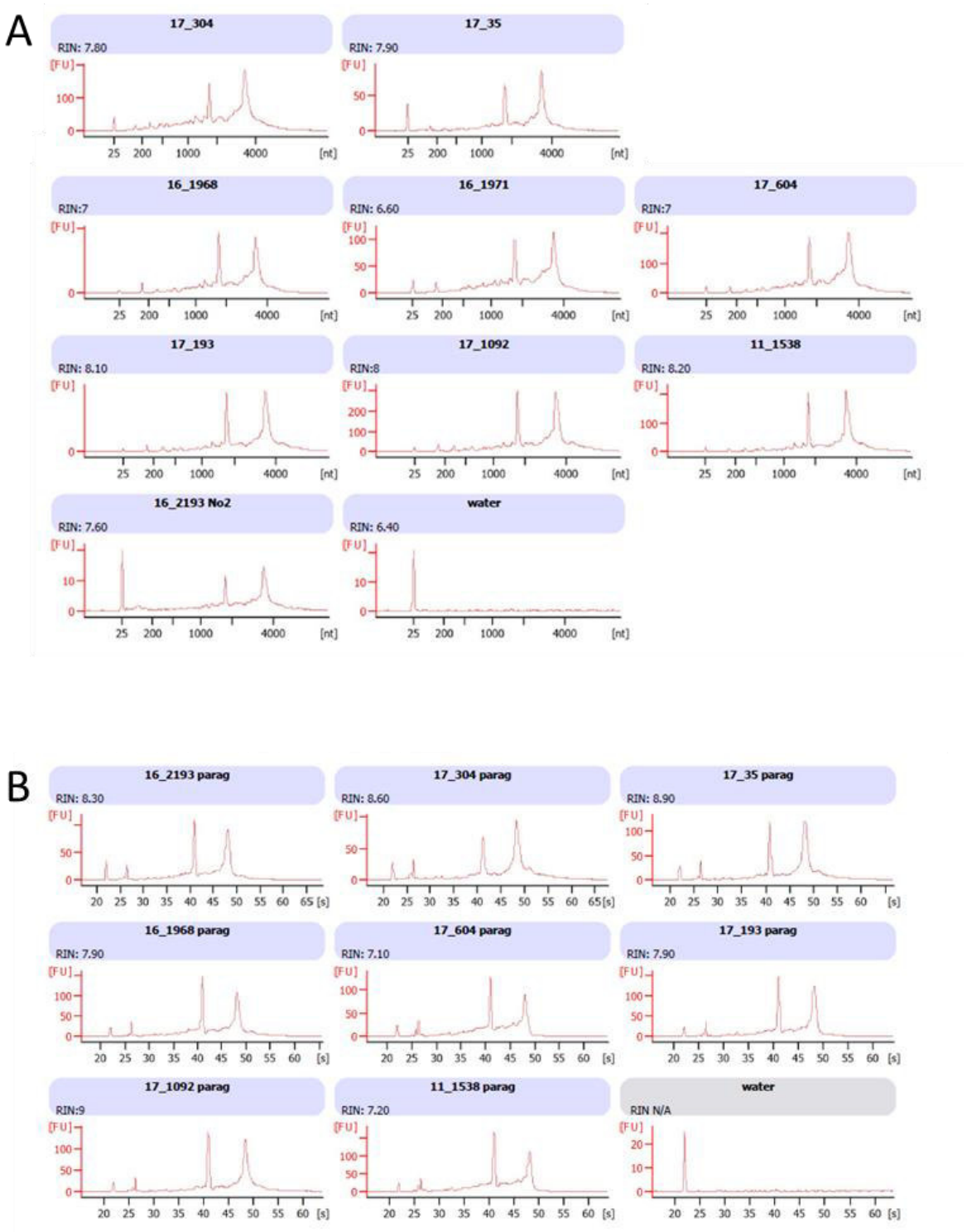

Figure 13: RIN values of samples used for arrays

Shown is the summary of RIN values generated by the 2100 Bioanalyzer instrument. (A) shows the RIN values of the PCC samples, and (B) shows the RIN values for the PGL samples. Sample 16_1971 was excluded from further array analysis due to the RIN value.

2.2.7.3 Laser Microdissection (LMD)

Laser Microdissection was carried out using a Leica DM6000 LMD instrument.

Samples were stored at -80°C. For performing the LMD, samples were put into a Cryo-Microtome (CM3050S, Leica) and were left in there for 30min to 1h to equilibrate to the temperature (-20°C). Tissues were placed in the Microtome, and thin slices of 10 µm were cut and put on PEN Membrane Glass slides (Life Technologies) that had been irradiated with UV light beforehand.

The so cut slices were transported on dry ice to the LMD instrument. For staining, slides were put in 75% EtOH for 2min, following 5-10s in 1% Cresyl-Violett solution. Slides were immediately put in 75% EtOH for a few seconds, following two incubation steps in 100% EtOH for 30s each. After slides were dried, LMD was immediately performed.

Cut tissues were stored in RLT buffer with β-Me and RNA was isolated using the RNeasy Micro Kit (Qiagen, #74004) as described before.

A schematic workflow of the LMD process including downstream array analysis is shown in Figure 14.

2.2.8 Gene expression studies

2.2.8.1 Reverse transcription (RT)

cDNA generation by reverse transcription was performed using the High-Capacity RNA-to-cDNA™ Kit (Thermo Fisher, #4387406) with 0.3-2µg of total RNA input.

The exact reaction mixture was prepared according to Table 11. A Reverse transcription (Enzyme Mix) negative control was used each time. The reaction mixture was placed into Eppendorf® Mastercycler X50i (Eppendorf) at 37°C for 60min, 95°C for 5min and held at 4°C. The cDNA was diluted by adding 80 µl of nuclease-free water for a final volume of 100 µl. The so obtained cDNA was stored at -20°C until further use.

Table 11: Reagents used for cDNA synthesis

	Volume [µl]	
	RT reaction (+)	RT reaction (-)
2x RT Buffer Mix	10.0	10.0
20X RT Enzyme Mix	1.0	-
RNA sample	up to 9.0	up to 9.0
Nuclease free H_20	up to 20.0	up to 20.0
Total Volume	20.0	20.0

2.2.8.2 qRT-PCR

To analyze gene expression levels of specific genes of interest, TaqMan™ PCR (Thermo ScientificTM) was used on QuantStudio™ 7 Flex (Thermo Fisher Scientific). TaqMan® probes with FAM™ dyes and Fast Advanced Master Mix (#4444557, Thermo Fisher Scientific) were used. All experiments were performed in triplicates and were normalized to a housekeeping gene. For this, beta-2-microtubulin was used. Each reaction had a final volume of 10 µL, which included 5 µL of TaqMan® Fast Advanced Master Mix, 1 µL of template cDNA, 0.5 µl TaqMan® probes and 3.5µL nuclease-free water. The used TaqMan® assays are listed in Table 12.

Data analysis was performed by analyzing the raw data in Excel and fold changes were determined by using 2–ΔCt method. Briefly, average Ct value was calculated for each sample and ΔCt was calculated taking the average Ct of the gene of interest subtracted by the average Ct

of the housekeeping gene. Next, ΔΔCt was calculated by subtracting the ΔCt (control sample) from the ΔCt (test sample). Lastly, 2–ΔCt for test sample and control sample was calculated using 2 to the power of negative ΔΔCt.

Table 12: TaqMan assays used in this thesis

Assay ID	Gene name	Dye	Species
Hs00187842_m1	B2M	FAM-MGB	human
Hs00171105_m1	ccna1	FAM-MGB	human
Hs00427214_g1	pcna	FAM-MGB	human
Mm00437762_m1	B2M	FAM-MGB	mouse
Mm00432337_m1	ccna1	FAM-MGB	mouse
Mm05873628_g1	pcna	FAM-MGB	mouse
Rn01429556_m1	Col6a1	FAM-MGB	rat
Rn00569647_m1	Col3a1	FAM-MGB	rat
Rn01239749_m1	Jag1	FAM-MGB	rat
Rn03416813_gH	Eya1	FAM-MGB	rat
Rn01407987_m1	ANG	FAM-MGB	rat
Rn01466080_m1	Lama4	FAM-MGB	rat
Rn00572063_m1	Loxl2	FAM-MGB	rat
Rn01437681_m1	MMP14	FAM-MGB	rat
Rn00579172_m1	CXCL12	FAM-MGB	rat
Rn00573260_m1	LTBP2	FAM-MGB	rat
Rn00560865_m1	B2M	FAM-MGB	rat
Rn01761348_m1	ccna1	FAM-MGB	rat
Rn01514538_g1	pcna	FAM-MGB	rat

2.2.8.3 Gene Arrays

For the gene expression studies of MENX PCCs and PGLs, GeneChip™ Rat Gene 1.0 ST Arrays (Thermo Fisher Scientific) were used. Amplified cDNA for the arrays was generated by using the Ovation® Pico WTA System V2 (Nugen) and following the manufacturer's instructions. Generated cDNA was then used for the Gene Arrays. Run of arrays and analysis was performed by Dr. Martin Irmler of the Institute of Experimental Genetics, Helmholtz Zentrum München. The whole workflow starting from RNA isolation to the gene arrays can be seen in Figure 14.

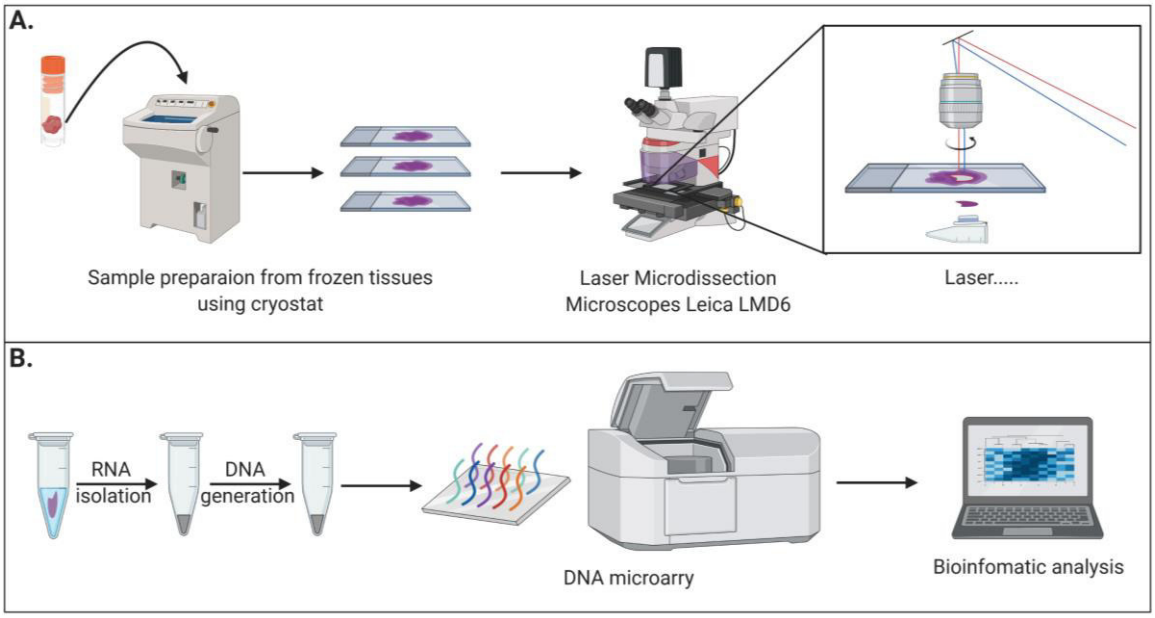

Figure 14: LMD-RNA isolation to arrays workflow
Shown is the workflow starting with cryosectioning, RNA isolation using LMD, cDNA generation and array analysis of the PPGL samples used in this thesis. Created with BioRender.com

2.2.9 Protein expression analysis

2.2.9.1 Protein isolation and BCA assay

Cells were washed with ice-cold 1x PBS (gibco, #14190-094). Ice-cold RIPA buffer (Sigma-Aldrich, #R0278) containing PhosTOP™(Roche, #04906837001) and cOmplete™Mini (Roche, #11836153001) was added to the cells, cells were scraped off and transferred into a 1.5 ml reaction tube. For cell debris removal, the lysates were centrifuged at 14,000g at 4°C for 15 minutes, and the supernatant was transferred to a fresh tube. Protein quantification was carried out using Pierce™ BCA Protein Assay Kit (Thermo Fisher Scientific, #23225) following the manufacture's protocol, and the absorbance was measured at 560 nm.

2.2.9.2 Western Blotting

Using Novex™ 10% Tris-Glycine Gels (Invitrogen), 35µg of protein were resolved together with page ruler (Thermo Fisher Scientific, #26616). The transfer was done by using the Trans-Blot® Turbo™ Transfer System (Bio-Rad) and nitrocellulose membrane (Bio-Rad, #1704271). Membrane blocking was done with 5% non-fat dry milk (CarlRoth, #T145.2) for 1h at RT. After that, membranes were incubated overnight with primary antibodies (Table 13) at 4°C. The next day, membranes were washed three times for 10 minutes with TBS-T and consequently incubated with the secondary antibody for 1h at RT. Then membranes were again washed 3 times for 10 minutes with TBS-T. Protein detection was carried out using chemiluminescent reagents (Thermo Fisher Scientific, SuperSignal) and hyper film ECL (GE healthcare, #28906837). Quantification of signal intensity was done with ImageJ software by analyzing the intensity of the protein bands and normalizing expression to the housekeeping control. Visualization and statistical analysis were done using GraphPad Prism software.

Table 13: Antibodies used for WB

Type	Antibody	Clonality	Company	ID	Dilution
Primary	Phospho-S6 Ribosomal Protein (Ser240/244) (D68F8) XP®	Rabbit	Cell Signaling Technology	5364	1/2500
Primary	S6 Ribosomal Protein (5G10)	Rabbit	Cell Signaling Technology	2217	1/2500
Primary	Akt Antibody	Rabbit	Cell Signaling Technology	9272	1/1000
Primary	Phospho-Akt (Ser473) (D9E) XP®	Rabbit	Cell Signaling Technology	4060	1/2000
Primary HRP	α-Tubulin (DM1A) Mouse mAb (HRP Conjugate)	Mouse	Cell Signaling Technology	12351	1/5000
Secondary	Rabbit IgG HRP Linked Whole Ab		GE Healthcare	NA934V	1/2000

2.2.9.3 Immunohistochemistry

Immunohistochemistry was performed using the standard protocol suggested by abcam. Slides were cut for IHC procedure by the Core Facility Pathology. First, slides were deparaffinized by incubation at 60°C for 10 minutes. After that rehydration was carried out by incubation in xylene for 2x15 minutes, 100% EtOH for 10 minutes, 95% EtOH for 1 minute, 85% EtOH for 1 minute, 75% EtOH for 1 minute and distilled water for 6 minutes. Antigen retrieval was carried out by cooking the slides in a pressure cooker for 18 minutes in Citrate buffer pH 6.0 (abcam). Afterward, slides were rinsed in distilled water for 5 min. Endogenous peroxidase was inactivated by incubation with hydrogen peroxide (abcam) for 15 minutes. Then, at least 3x5min TBS-T washing steps were performed. The non-specific antibody binding was blocked using protein block (abcam) for 15 minutes. Primary antibodies were diluted with antibody diluent (abcam) and incubated overnight at 4°C in a humidified chamber. The next days, slides were washed 3x5 min with TBST and pre-diluted secondary antibody was applied to the sections for 15 minutes at room temperature. Slides were washed 3x5 min with TBST in order to

remove non-specific binding, and incubated with Streptavidin peroxide for 10 minutes at RT. Peroxidase activity was detected by freshly prepared DAB substrate (30 µl DAB chromogen + 1.5 ml DAB substrate) (abcam). After washing the slides with TBST, counterstaining was performed using Haematoxylin for 1 minute, followed by rinsing the slides with tap water. The slides were de-hydrated through a series of de-hydration steps: 75% EtOH (1 minute), 85% EtOH (1 minute), 95% EtOH (1 minute), 100% EtOH (3 minutes) and xylene (3 minutes). Mounting was done using mounting media (abcam) and then slides were dryed overnight at RT. Pictures were taken using Nikon Eclipse Ci Upright microscope.
For this thesis, NuSAP primary antibody (#12024-1-AP, Proteintech, 1/250) and Rabbit specific HRP (ab64261, abcam) were used.

2.2.10 Statistical analysis

The experiments in this thesis were performed three times independently from each other with at least three technical replicates each time unless otherwise stated. Statistical analysis of the biological replicates was done by using Graph Pad Prism software. The statistical tests used are indicated in each figure legend.

3. Results

3.1 Molecular based therapy of PPGLs by targeting PI3K and CDK4/6

3.1.1 2D Treatment of PPGL cell lines with BKM120 and LEE011 *in vitro* reduces cell proliferation

Two different PPGL cell lines, MPC and PC12, were used to study the effect of the PI3K inhibitor BKM120 and the CDK4/6 inhibitor LEE011 *in vitro*. While MPC cells are of murine origin, PC12 cells were originally isolated from a rat PCC, and both are widely used in PPGL research. We first investigated the effect of different doses of BKM120 and LEE011 alone or in combination on the proliferation of PC12 cells. As observed in Figure 15, after 72h of treatment both the single drugs and the combination reduced cell proliferation compared to the DMSO control in a dose-dependent manner. A direct comparison of the three conditions showed that the combination of BKM120 + LEE011 had the strongest effect (IC50 of 0.2µM) followed by BKM120 (IC50 of 0.7µM). LEE011 had the weakest effect with an IC50 of 1.6µM. It can also be observed that for BKM120 and especially LEE011, higher concentrations than for the combination were needed to decrease proliferation to a minimum of 10-20%.

Additionally, the effect of these drugs was also assessed in the MPC cell line (Figure 16). As shown, after 72h of treatment BKM120 and LEE011 reduced cell proliferation both as single drugs and in combination. In all three conditions, a dose-dependent manner can be observed. The IC50 values show that the combination of BKM120 and LEE011 is the most effective, showing the lowest IC50. While BKM120 showed a clear reduction of cell proliferation starting with low doses, LEE011 had a weaker effect and a relatively high IC50 value compared to BKM120 and also compared to the value in the PC12 cells.

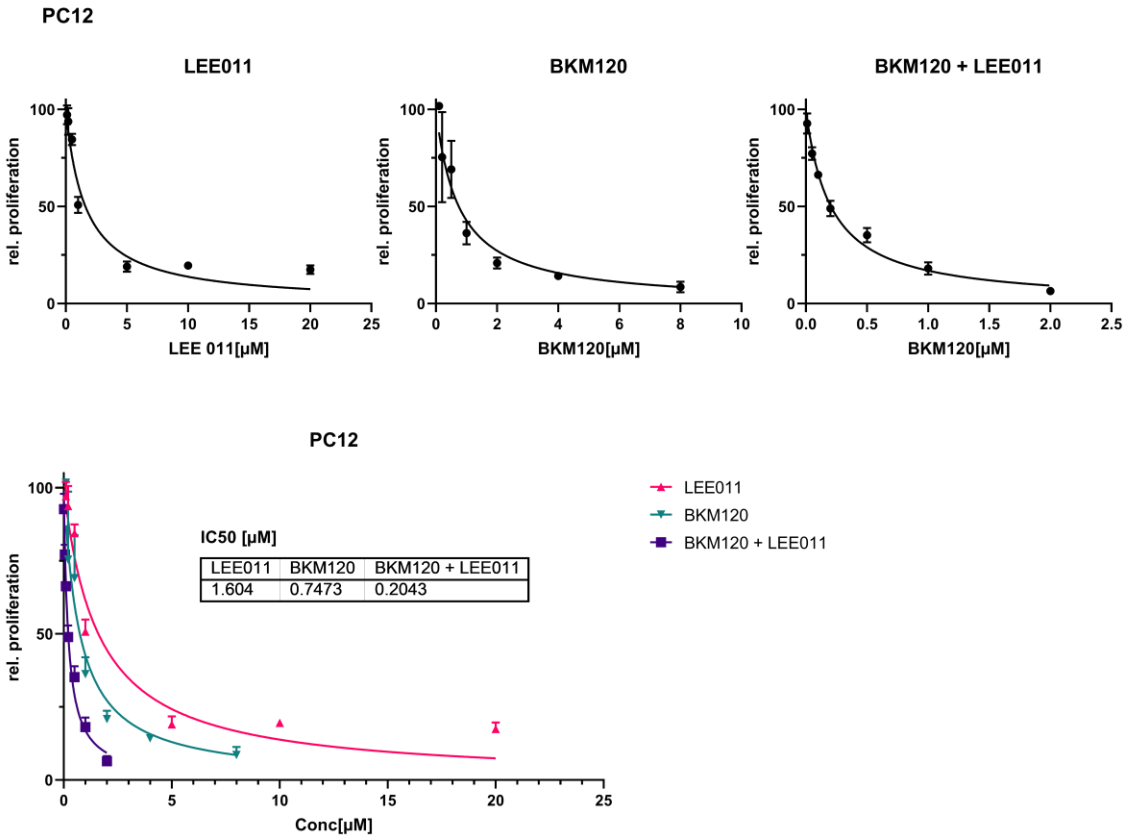

Figure 15: Effect of BKM120 and LEE011 on cell proliferation in PC12 cells
PC12 cells were treated with LEE011, BKM120, a combination of both drugs or DMSO as control in a 2D system. Cell proliferation was measured after 72h of treatment. Different concentrations were used to determine the IC50 values of the single drugs and the combination (Table 14). To evaluate the drug response, the DMSO control was set to 100% and nonlinear regression was used to determine the IC50. Data shows the mean ±SD from 3 independent experiments with 3 technical replicates each.

Table 14: Doses used in Figure 15

LEE011 [µM]	BKM 120 [µM]	BKM120 + LEE011 [µM]
0.1	0.1	0.01 + 0.04
0.2	0.2	0.05 + 0.2
0.5	0.5	0.1 + 0.4
1	1	0.2 + 0.8
5	2	0.5 + 2
10	4	1 +4
20	8	2 +8

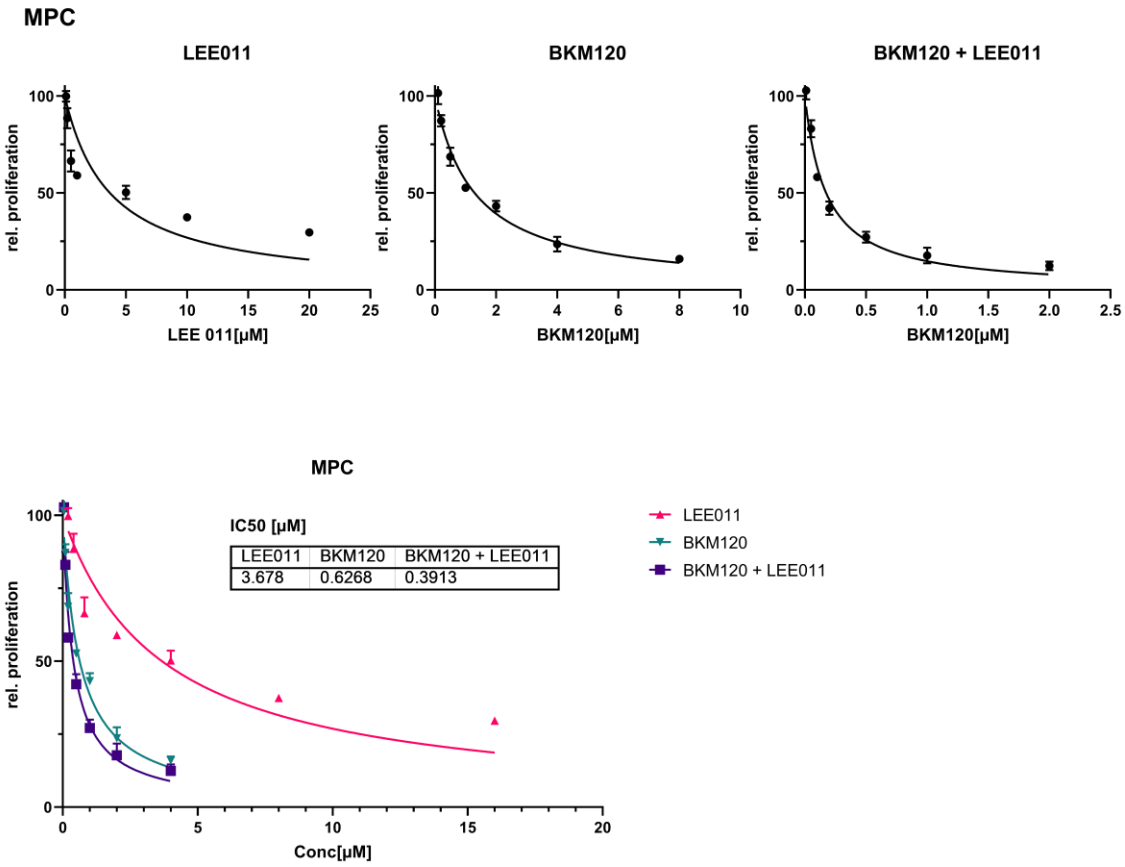

Figure 16: Effect of BKM120 and LEE011 on cell proliferation in MPC cells
MPC cells were treated with LEE011, BKM120, a combination of both drugs or DMSO as control in a 2D system. Cell proliferation was measured after 72h of treatment. Different concentrations were used to determine the IC50 values of the single drugs and the combination (Table 15). To evaluate the drug response, the DMSO control was set to 100% and nonlinear regression was used to determine the IC50. Data shows the mean ±SD from 3 independent experiments with 3 technical replicates each.

Table 15: Doses used in Figure 16

LEE011 [µM]	BKM 120 [µM]	BKM120 + LEE011 [µM]
0.2	0.05	0.05 + 0.2
0.4	0.1	0.1 + 0.4
0.8	0.2	0.2 + 0.8
2	0.5	0.5 + 0.2
4	1	1 + 4
8	2	2 + 8
16	4	4 +16

3.1.2 2D Treatment of PPGL cell lines with BKM120 and LEE011 *in vitro* partly induces apoptosis

To further investigate the effects of BKM120 and LEE011 treatment, we performed an apoptosis assay by checking for Caspase 9 activity in treated cells. Apoptosis is an important parameter for cancer treatments: inducing the death of tumor cells may decrease tumor volume in a clinical context. To investigate if our drugs could induce apoptosis, we treated both PC12 and MPC cells grown as 2D monolayers with the single drugs or their combination. 72h after the start of the treatment, Caspase 9 activity was measured as seen in Figure 17. In both cell lines, induction of apoptosis can be seen in samples treated with BKM120 and with BKM120 + LEE011, while no apoptosis is observed in LEE011-treated samples. Apoptosis is induced in a dose-dependent manner in both cell lines. Direct comparison of the different doses shows a significantly better effect of BKM120 over LEE011 and of the combination over both single drugs in MPC and PC12 cells. Additionally, for low concentrations only the combination is able to induce apoptosis while the single drugs are not (BKM120 0.5µM + LEE011 2µM for PC12 and BKM120 0.2µM + LEE011 0.8µM for MPC).

This again shows a stronger effect of the drug combination compared to the single drugs as we already observed for cell proliferation.

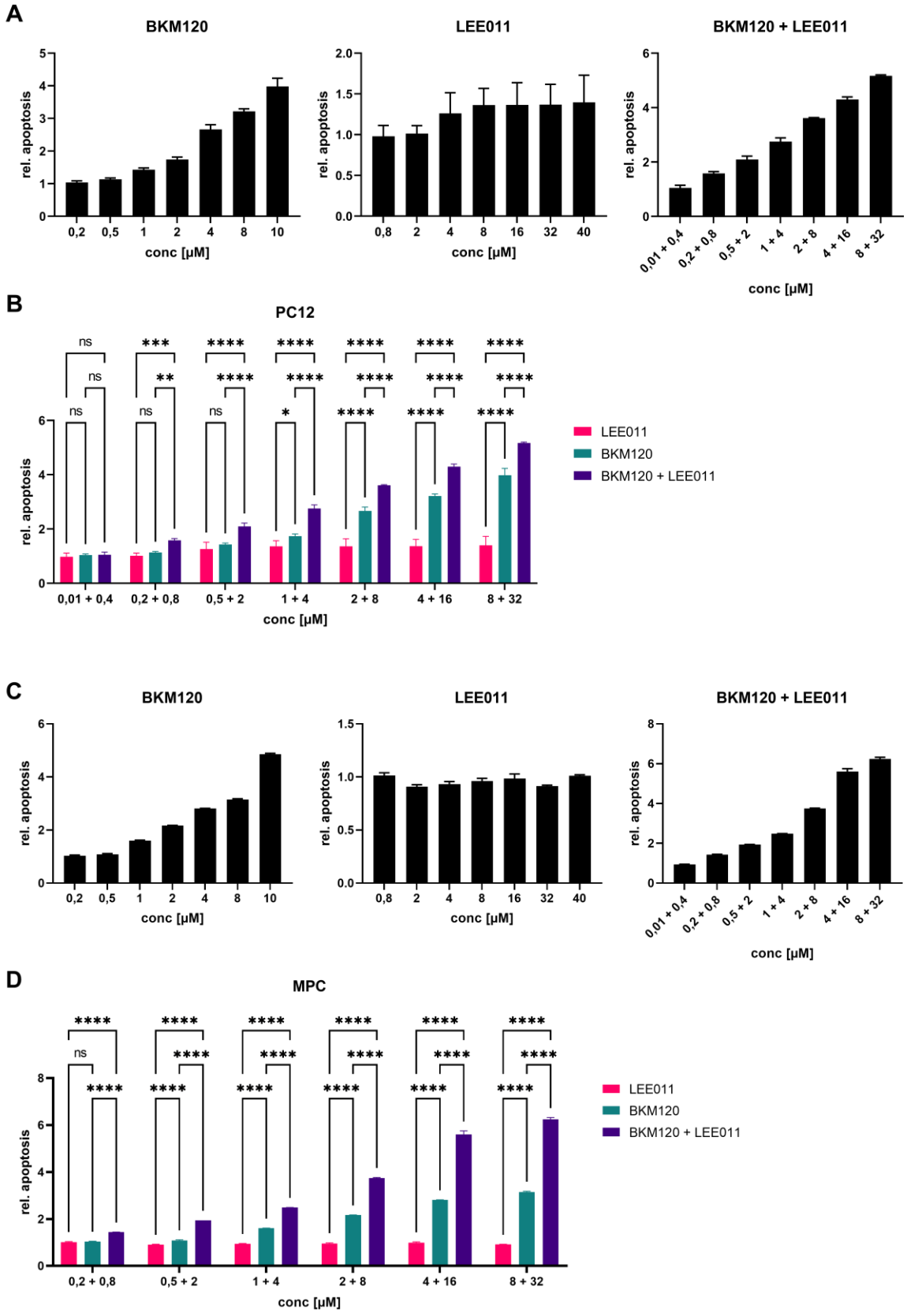

Figure 17: Apoptosis induction upon treatment in PC12 and MPC cells
PC12 (A,B) and MPC (C.D) cells were treated with LEE011, BKM120, a combination of both drugs or DMSO as control in a 2D system. Caspase 9 activity was measured after 72h of treatment and used

as a readout for apoptosis. A range of concentrations as shown in the panels was used to evaluate the effect of the drugs. A and C show an overview of the different treatments, while in B and D the different treatments are directly compared. Shown is always the relative apoptosis normalized to the DMSO control. Data shows the mean ±SD from 3 independent experiments with 3 technical replicates each. 2way ANOVA. ns, not significant; *, p< 0.05; **, p< 0.01; ***, p<0.001; ****, p< 0.0001

3.1.3 Migration and invasion behavior of PC12 and MPC cells upon BKM120 and LEE011 treatment

As migration and invasion of tumor cells are characteristics of aggressive behavior and are associated with bad prognosis, we wanted to test whether our treatment approach would also affect these parameters. To this end, we used a 2D migration and invasion system. Transwell inserts coated with Matrigel or uncoated were used to assess invasion and migration, respectively. PC12 and MPC cells were seeded in the inserts, and 24h later medium with chemo-attractants was added to the bottom of the well. As seen in Figure 18 A, C PC12 cells did migrate and invade. Treatment with BKM120 and LEE011 as well as with the combination significantly reduced the migration of PC12 cells. Especially treatment with BKM120 alone or with the combination reduced the migration to a minimum. Additionally, also invasion was reduced upon treatment with BKM120 or the combination, but not with LEE011. Treatment of PC12 cells with the combination reduced invading cells significantly better than with BKM120 and LEE011 individually. Overall, we saw a strong effect of the treatment on migration and invasion, which were suppressed upon the combination-treatment.

In contrast to PC12 cells, MPC cells did not show any ability to migrate and invade in this assay. Figure 19 shows that no cells could be detected on the bottom of the inserts (Figure 19 A), while the plated cells on the surface were visible (Figure 19 B).

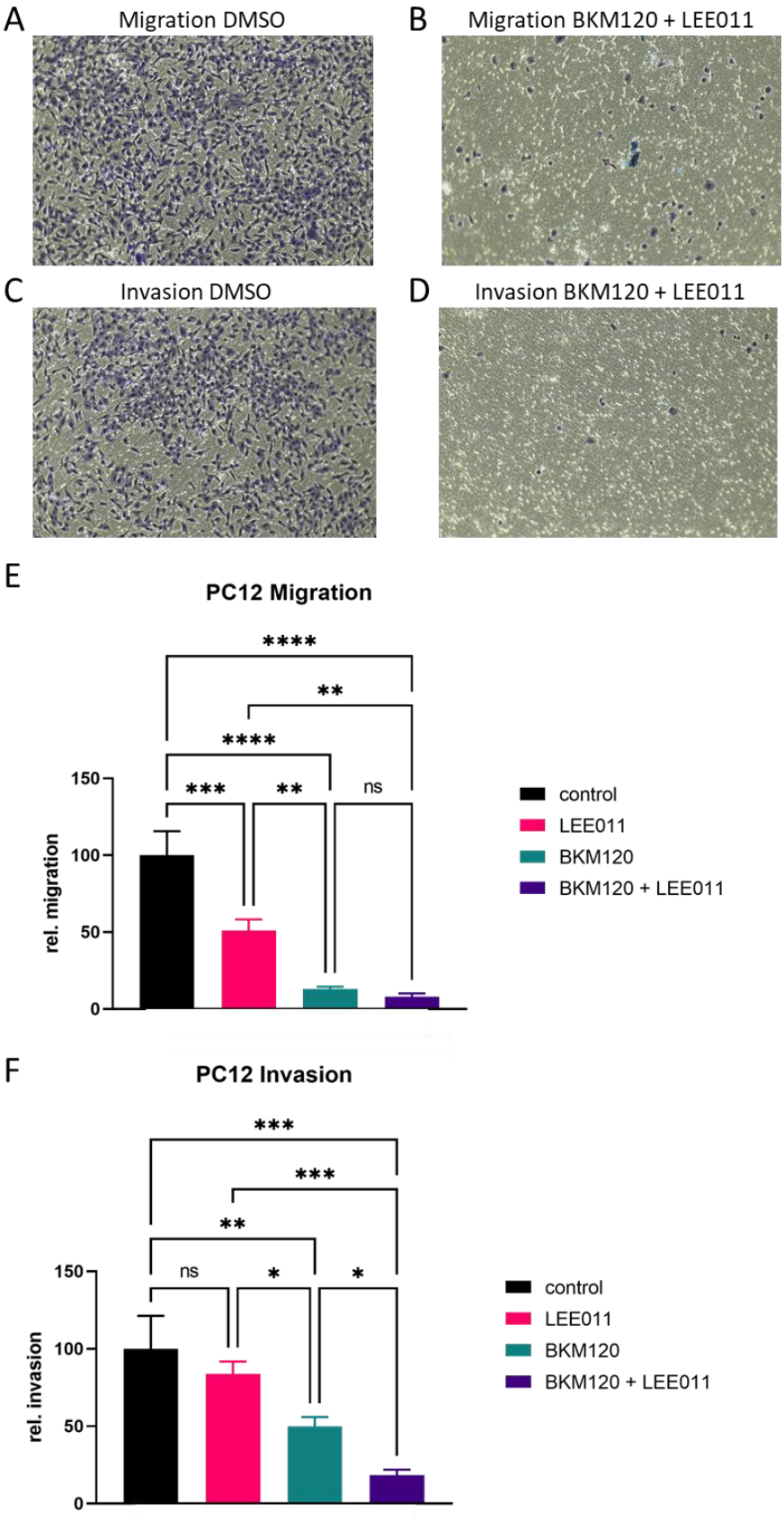

Figure 18: 2D Migration and Invasion in treated PC12 cells
PC12 cells were plated in invasion chambers containing Matrigel or migration chambers without Matrigel. After 72h of treatment with IC50 values as calculated before, chambers were collected and

stained for migrated and invaded cells. Cells were photographed (3 technical replicates for each condition) and pictures were taken for 3 representative fields per sample for calculating the average. A-D shows a representative picture of migrated and invaded cells in DMSO and BKM120 + LEE011 treated samples. E and F show the quantification of all pictures. Data show the mean ±SD from three independent experiments. 1way ANOVA ns, not significant; *, p< 0.05; **, p< 0.01; ***, p<0.001; ****, p< 0.0001

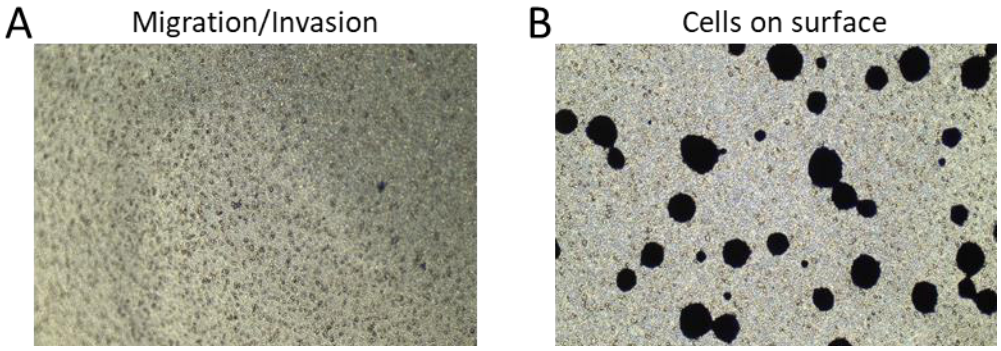

Figure 19: Migration and Invasion of MPC cells
MPC cells were plated in invasion chambers containing Matrigel or migration chambers without Matrigel. After 72h of treatment with IC50 values as calculated before, chambers were collected and stained for migrated and invaded cells. Cells were photographed (3 technical replicates for each condition) and pictures were taken for 3 representative fields per sample for calculating the average. A shows an example of a well for migrated and invaded cells, whereas B shows the plated cells on the surface of the chamber. Three independent experiments were performed

3.1.4 Confirmation of pathway downregulation by WB and qPCR

So far, our treatment approach with BKM120 and LEE011 as single drugs or in combination showed good anti-tumor effects in PPGL cells. In detail, these agents and especially their combination reduced cell proliferation, induced apoptosis and suppressed migration and invasion. To confirm that the observed effects are due to a downregulation of the PI3K/AKT and the CDK4/6 pathway, we set out to analyze downstream targets of both pathways using WB and qPCR.

Downregulation of the PI3K/AKT pathway was assessed using WB looking for the phosphorylation of pAKT and pS6 after treatment. Both proteins are involved in the PI3K pathway and are expected to be reduced after treatment with BKM120. As shown in Figure 20, treatment with BKM120 significantly reduced the pAKT/AKT as well as the pS6/S6 signal ratio in both PC12 and MPC cells. This effect could be observed both in the single drug treatment with BKM120 and in the combination. As expected, treatment with DMSO (control) and LEE011 showed no effect on pAKT/AKT and pS6/S6.

To confirm the downregulation of the CDK4/6 pathway, we analyzed the expression of two genes, *Ccna1*(Cyclin A1) and *Pcna* (Proliferating Cell Nuclear Antigen) upon treatment. Both genes are involved in the cell cycle and are associated with CDK-pRB-E2F signaling. As shown in Figure 21, the expression of both genes was significantly reduced upon LEE011 treatment in both cell lines. This confirms the successful downregulation of the CDK4/6 pathway after treatment with LEE011.

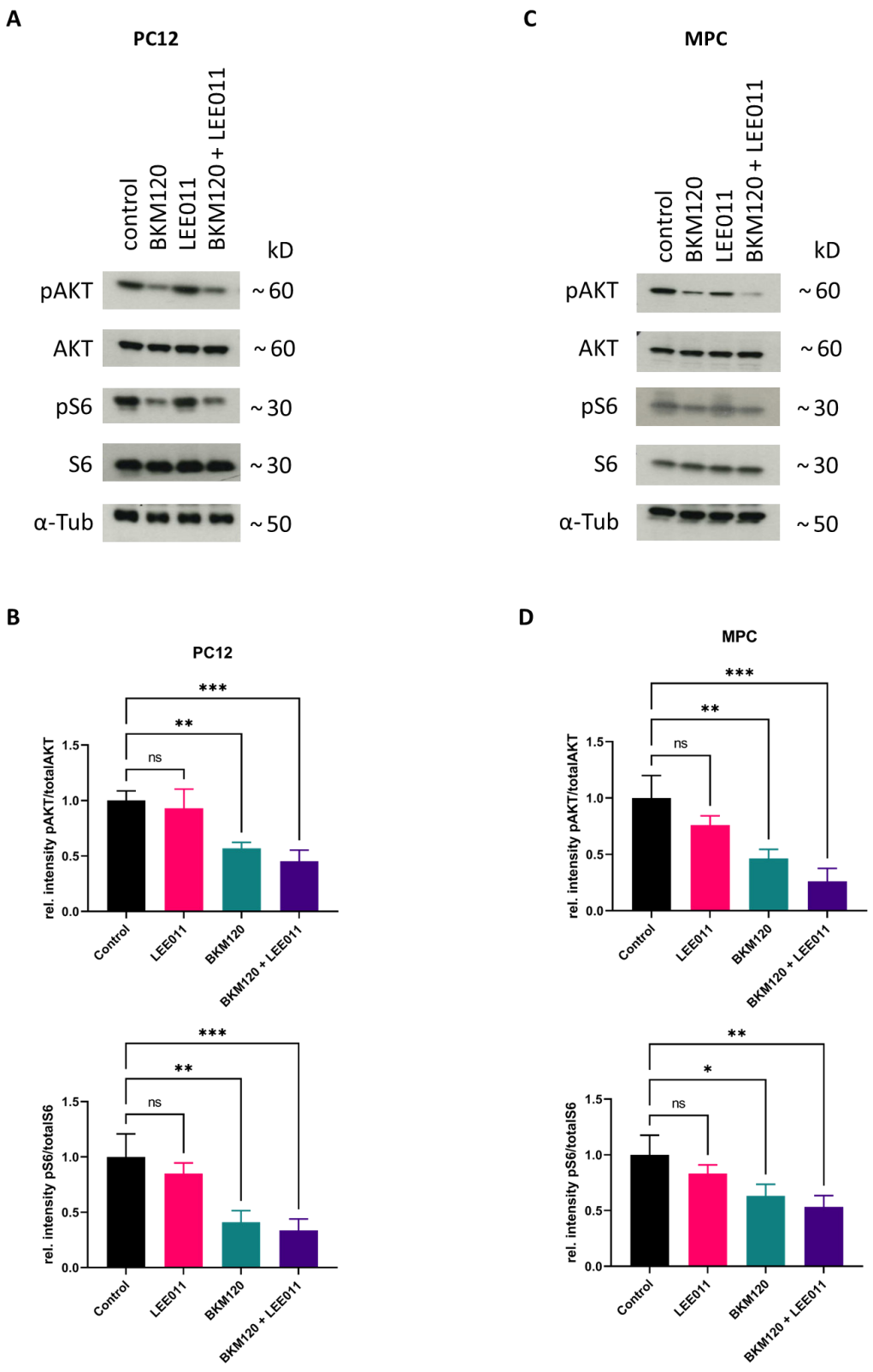

Figure 20: WB for PI3K pathway targets in PC12 and MPC cells

A and C show immunoblots representing phospho-Akt (pAKT), total Akt, phospho- S6 (p-S6), total S6 and α-Tubulin for PC12 and MPC cells, respectively. Shown is one representative immunoblot out of three experiments. B and D show graphs representing the ratio of pAkt over total Akt and pS6 over total S6. Data shows the mean ±SD from three independent experiments. 1way ANOVA, ns, not significant; *, p< 0.05; **, p< 0.01; ***, p<0.001

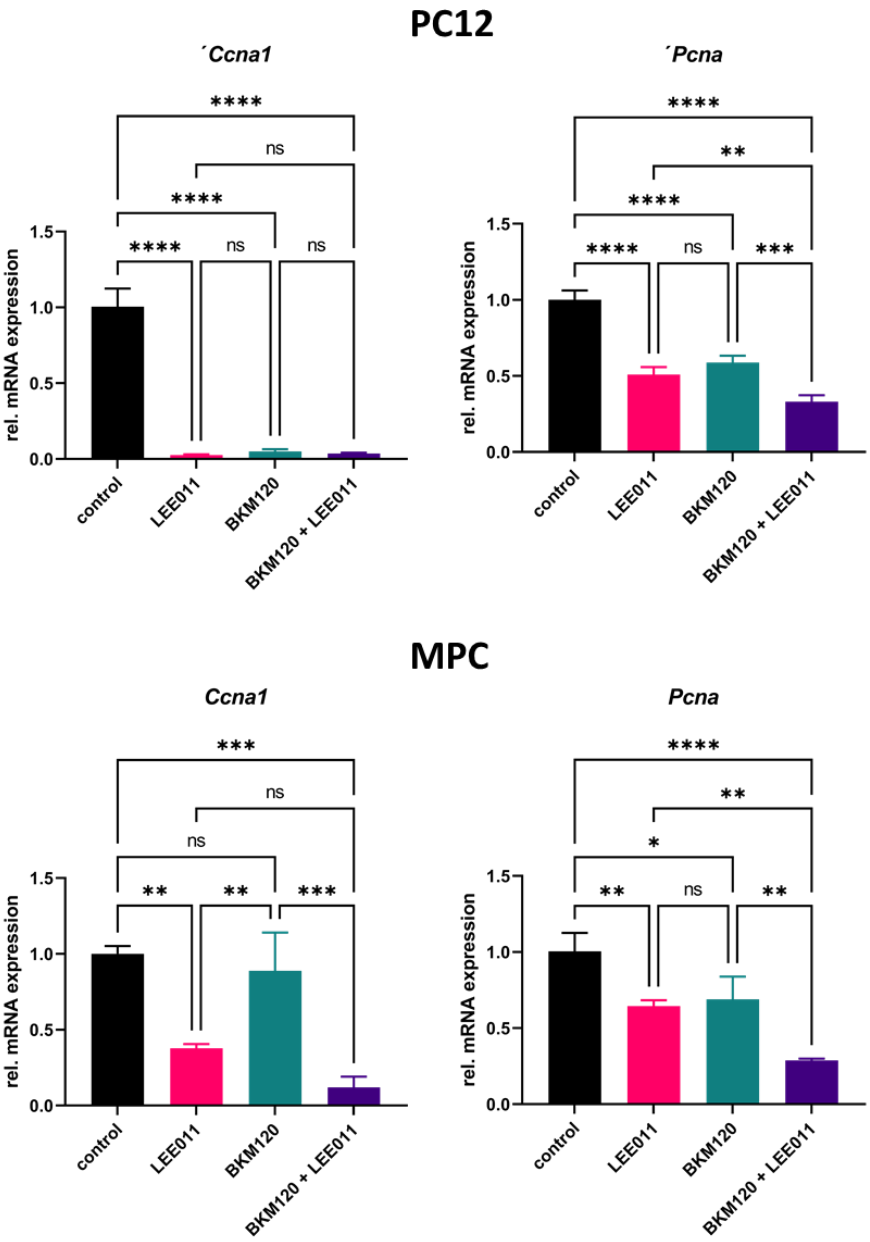

Figure 21: qPCR of PC12 and MPC cells after treatment
PC12 and MPC cells were plated in 2D cell culture. After 72h of treatment with BKM120, LEE011 and BKM120 + LEE011 using IC50 values pellets were collected and RNA isolated. Gene expression for Ccna1 and Pcna was carried out using TaqMan probes. Data represent the mean ±SD from three independent biological replicates. 1way ANOVA ns, not significant; *, p< 0.05; **, p< 0.01; ***, p<0.001; ****, p< 0.0001

3.1.5 Effect of BKM120 and LEE011 on cell viability and growth of PC12 and MPC cells in a 3D system

As 2D cell culture cannot recapitulate the *in vivo* parameters, 3D cell culture systems are often used as a model system in which cells behave more closely to an in-body situation. We used ultra-low attachment plates to generate 3D spheroids from PC12 and MPC cells. After spheroid formation, cells were treated with the single drugs or with the drug combination to analyze their effect on cell viability. Using an assay suitable for 3D cell culture, cell viability was measured at various time points after the addition of the drugs (2h(start), 24h, 48h and 72h). The assay allows the continuous measurement of cell viability in a 3D culture system by measuring the reducing potential of viable cells in an ATP-independent manner.

As shown in Figure 22, both BKM120 and LEE011 as well as the combination reduced cell viability in PC12 cells. BKM120 showed a reduction from 0.2µM onwards, whereas for LEE011 only the highest dose (100µM) showed an effect. Over the course of 72h, cell viability increased overall within the first 24h and then stayed on a similar level or was even reduced upon treatment. After 72h of treatment, the combination was significantly more effective compared to both the single drugs in almost all of the used concentrations. BKM120 reduced cell viability more efficiently than LEE011.

Similar experiments were also conducted with the MPC cells, and also in these cells BKM120 and LEE011 reduced the cell viability in a dose-dependent manner as seen in Figure 23. Although BKM120 and LEE011 show no viability reducing effects in the first 24h, they are able to reduce cell viability after 72h. This reduction can especially be seen in the combination group. Looking at the 72h timepoint, there is no difference between the three treatment groups at the low concentrations. Using concentrations that show an effect on cell viability, BKM120 is effective at lower doses compared to LEE011 and the combination shows a significantly better reduction of cell viability compared to the single drugs.

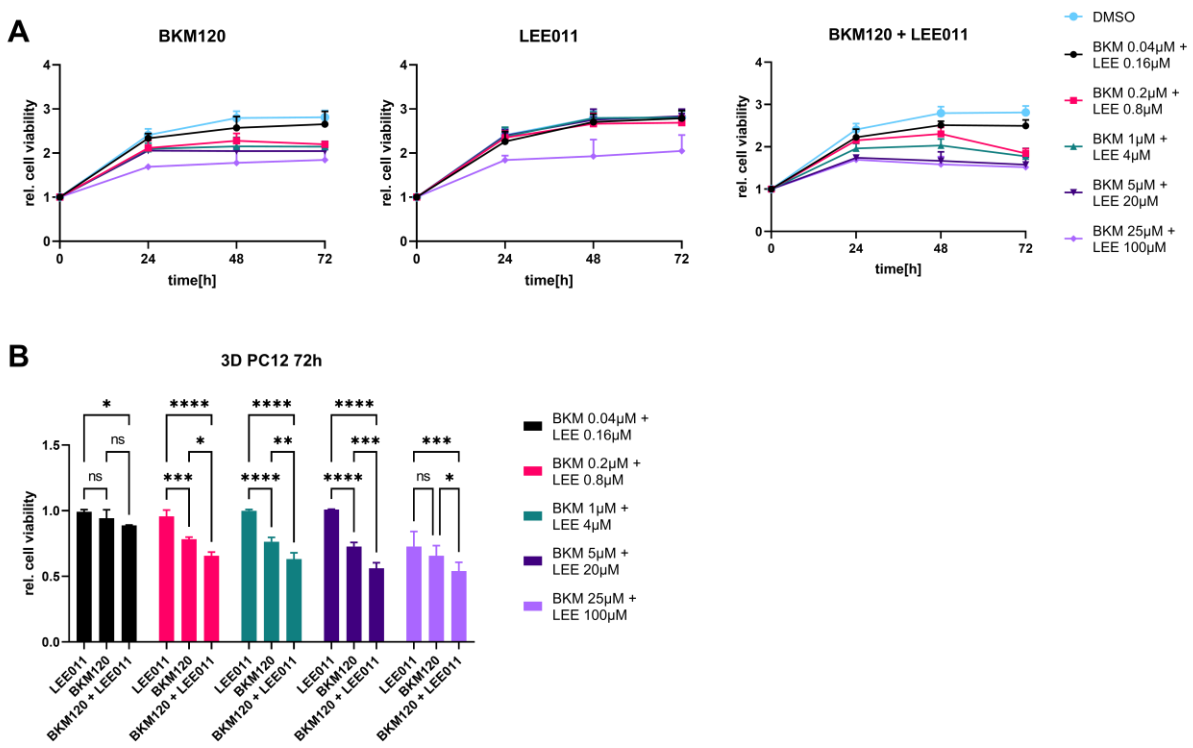

Figure 22: 3D cell viability in treated PC12 cells

PC12 cells were treated with LEE011, BKM120, a combination of both drugs or DMSO as control in a 3D system using ULA plates. Cell viability was measured after the addition of drugs and after 24h, 48h, 72h. A range of concentrations as shown in the panels was used to evaluate the effect of the drugs. A shows the overview of each drug treatment over 72h, whereas in B the comparison of the treatments with different concentrations at the 72h timepoint is shown. Shown is the relative cell viability normalized to the initial measurement and the DMSO control. Data shows the mean ±SD from 3 independent experiments with 8 technical replicates each. 2way ANOVA. ns, not significant; *, p< 0.05; **, p< 0.01; ***, p<0.001; ****, p< 0.0001

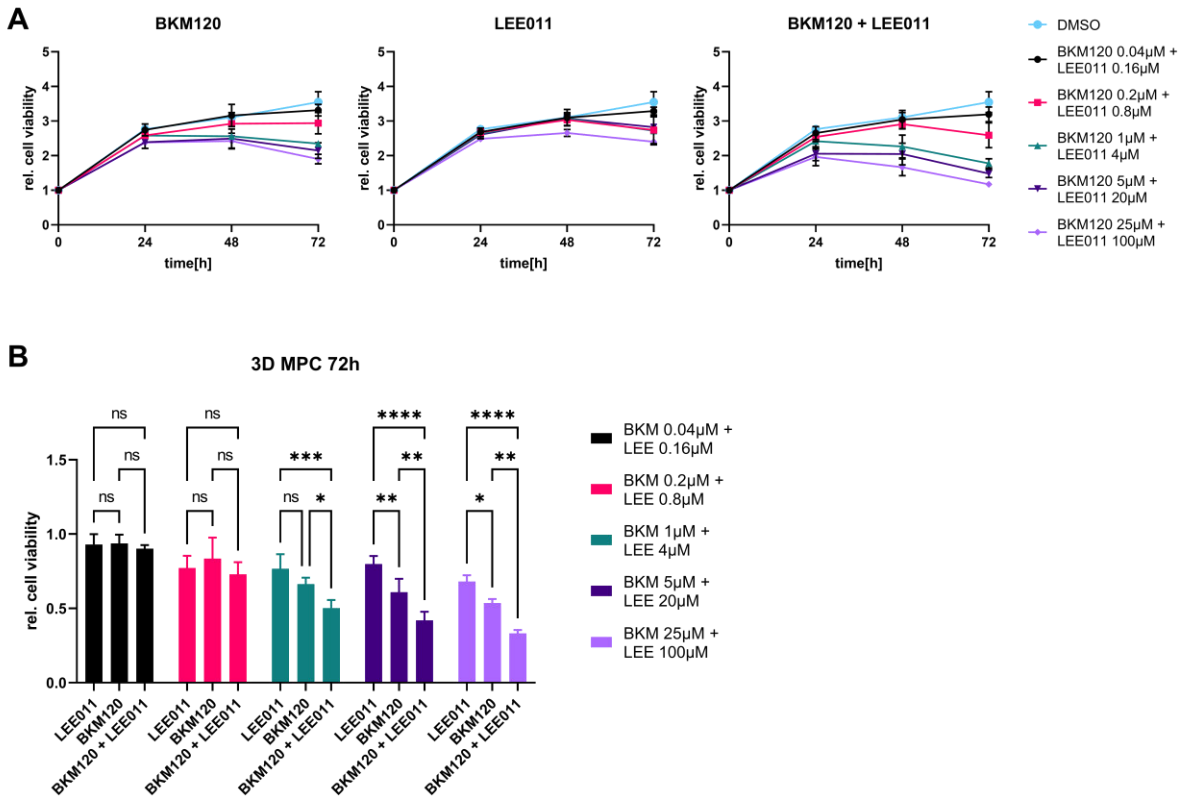

Figure 23: 3D cell viability in treated MPC cells
MPC cells were treated with LEE011, BKM120, a combination of both drugs or DMSO as control in a 3D system using ULA plates. Cell viability was measured after the addition of drugs and after 24h, 48h, 72h. A range of concentrations as shown in the panels was used to evaluate the effect of the drugs. (A) shows the overview of each drug treatment over 72h, whereas in (B) the comparison of the treatments with different concentrations at the 72h timepoint is shown. Shown is the relative cell viability normalized to the initial measurement and the DMSO control. Data shows the mean ±SD from 3 independent experiments with 8 technical replicates each. 2way ANOVA. ns, not significant; *, p< 0.05; **, p< 0.01; ***, p<0.001; ****, p< 0.0001

Additionally, we also investigated the growth of spheroids over 14 days of treatment. Spheroids were again generated by using ULA plates, and treatment was started after spheroid formation. The growth of the spheroids was measured at the start of the treatment (Day 0) and on Days 3, 7, 11 and 14. This experiment allowed us to have cell growth as a readout for the treatment and to also observe the treatment effects over a longer period of time. Figure 24 A shows an example of the PC12 spheroids at the start of the treatment and on Day 3. It can be observed that the spheroids treated with the combination do not show any growth in size and additionally are very dark compared to the controls. Overall, the spheroids treatment with BKM120 or the combination completely inhibited spheroid growth, as shown in Figure 24 B, whereas LEE011 reduced spheroid growth starting from day 7. Looking at the 72h timepoint allows for a comparison with the results we have seen using the cell viability assay. In contrast to the cell viability measurement, there was no difference between BKM120 and the drug combination after 72h of treatment.

Looking at the MPC spheroids, a similar behavior can be seen in terms of reduced growth and darkening of the treated spheroid at Day 3 (Figure 25 A). In contrast to PC12 cells, all three treatments inhibited MPC cell growth over a period of 14 days as shown in Figure 25 B. Additionally, it can be seen that BKM120 reduces the tumor growth significantly better than LEE011 after 72h. Also, the combination of BKM120 + LEE011 shows a significantly better effect than both single drugs, which is in line with the results obtained for cell viability.

Overall, the results show that in both cell lines spheroid growth is significantly reduced upon treatment with the selected drugs and that BKM120, as well as the combination, show the best results.

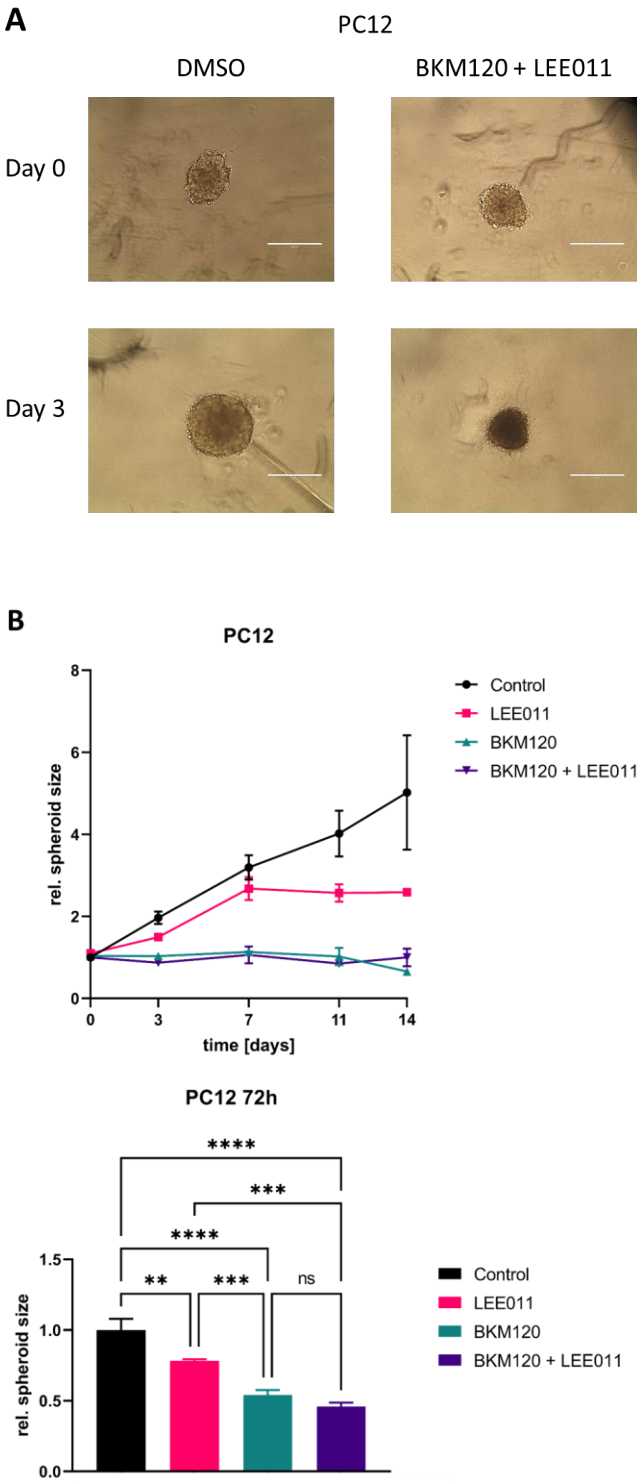

Figure 24: PC12 spheroid growth

PC12 cells were treated with LEE011 (20µM), BKM120 (5µM), a combination of both drugs or DMSO as control in a 3D system using ULA plates. Spheroid pictures were taken after the addition of drugs and after 3, 7, 11 and 14 days. Spheroid size was measured using ImageJ. (A) shows representative images of spheroids on Day 0 and Day 3 treated with DMSO (control) or the drug combination. (B) shows the rel. spheroid size over the course of 14 days with a statistical analysis of the 72h time point. Data shows the mean ±SD from 3 independent experiments with 8 technical replicates each. 1way ANOVA. ns, not significant; *, p< 0.05; **, p< 0.01; ***, p<0.001; ****, p< 0.0001

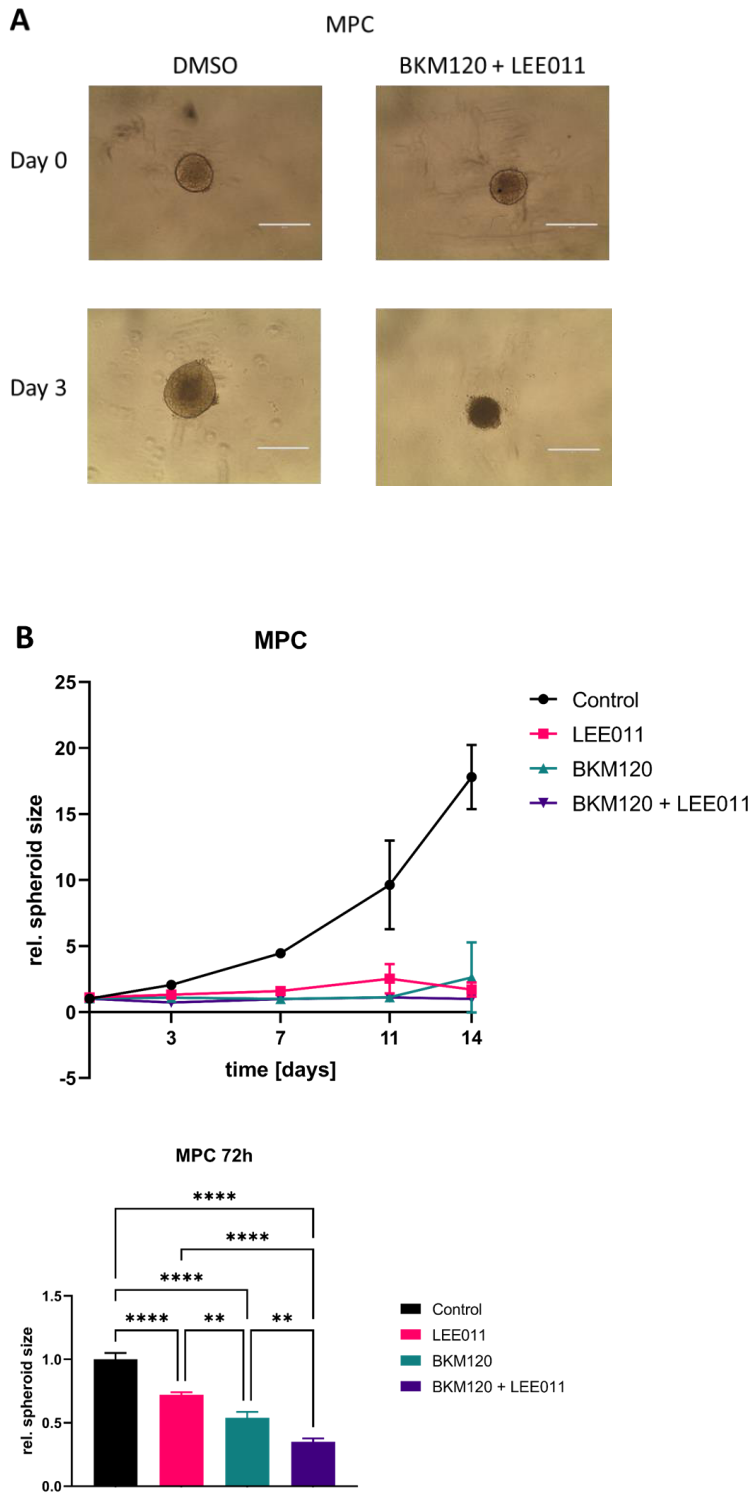

Figure 25: MPC spheroid growth

MPC cells were treated with LEE011 (20µM), BKM120 (5µM), a combination of both drugs or DMSO as control in a 3D system using ULA plates. Spheroid pictures were taken after the addition of drugs and after 3, 7, 11 and 14 days. Spheroid size was measured using ImageJ. (A) shows representative images of spheroids on Day 0 and Day 3 treated with DMSO (control) or the drug combination. (B) shows the rel. spheroid size over the course of 14 days with a statistical analysis of the 72h time point. Data shows the mean ±SD from 3 independent experiments with 8 technical replicates each. 1way ANOVA. ns, not significant; *, p< 0.05; **, p< 0.01; ***, p<0.001; ****, p< 0.0001

3.1.6 3D invasion of PC12 and MPC cells upon treatment

As MPC cells did not invade in the 2D system, we set out to test the invasion of both cell lines in a 3D system. For this, PC12 and MPC cells were plated in ULA plates and allowed to form spheroids. After spheroid formation, Matrigel was added into the wells and medium containing the drugs or DMSO was added. Cells without Matrigel were used as growth controls. Similar to the 2D situation, MPC cells did not show any potential to invade (Figure 26 C), whereas PC12 cells showed invasion after seven days (Figure 26 A). Analyzing the area of invading cells, we found that both the single treatments and the combination drastically decreased the invasion compared to the DMSO control (Figure 26 B). The invasion was decreased to levels below 5% in the treated groups so that no differences between the treatments could be observed.

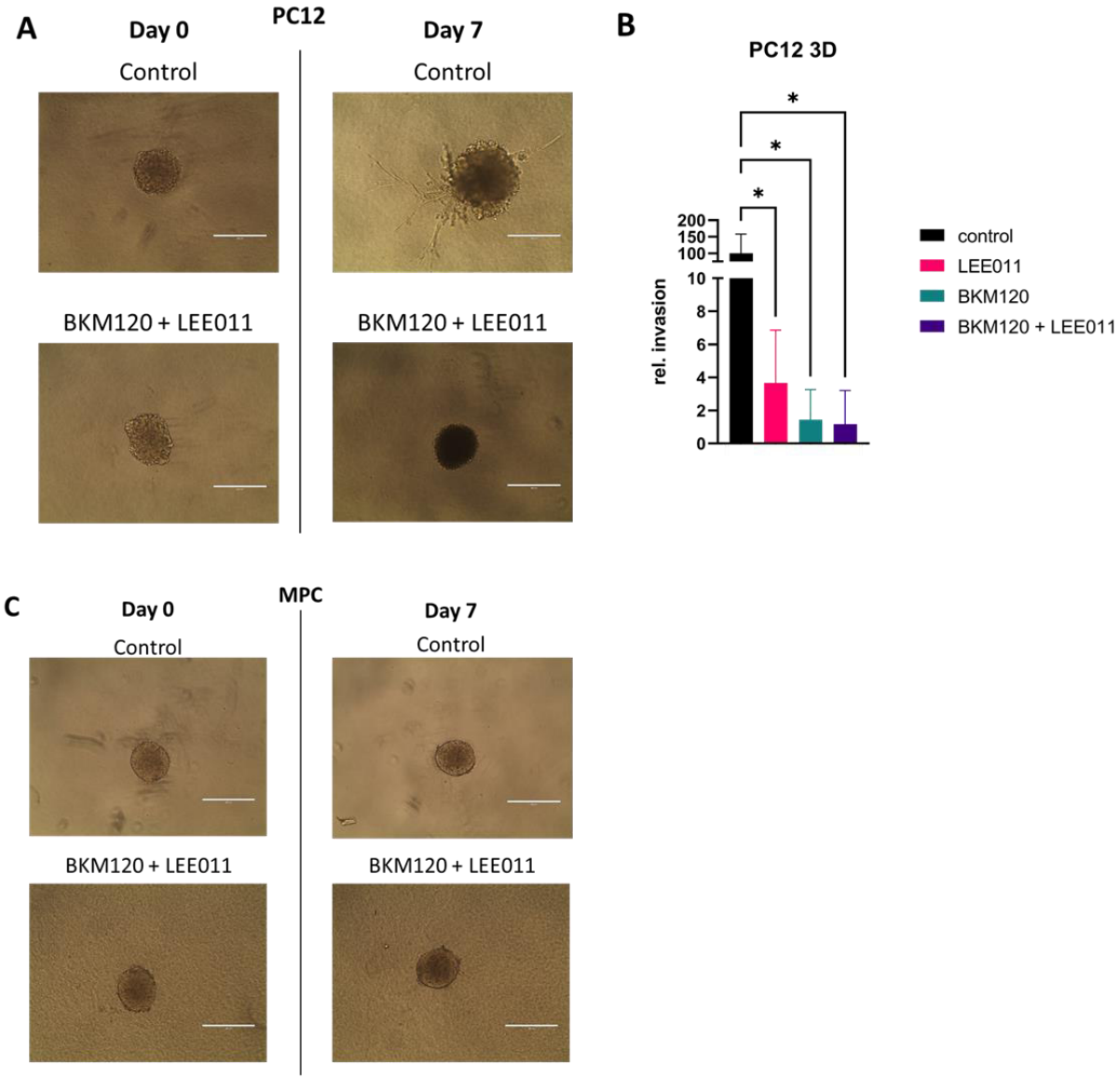

Figure 26: 3D invasion of PC12 and MPC cells
PC12 and MPC cells were seeded in ULA plates and Matrigel was added after spheroid formation to observe invasion. Cells were treated with BKM120 (5µM), LEE011 (20µM) or a combination of both drugs. Wells without Matrigel were used as growth control and invading area was calculated by sub-stracting the are of wells with Matrigel from well without Matrigel. Pictures were taken immediately after adding the Matrigel and after 7 days once invasion through the Matrigel was visible. Data show the mean ±SD from three independent experiments. 1way ANOVA. *, $p < 0.05$

3.1.7 Treatment of 3D MENX primary cells and assessment of cell viability

The MENX rat model harbors a frameshift mutation in the *Cdkn1B* gene encoding p27, which results in a mutant protein that is fastly degraded. Homozygous mutant rats develop PCCs with a full penetrance at the age of 8 months. We collected the adrenal tumors of seven animals, isolated the primary tumor cells and generated 3D spheroids using a hanging-drop system. After spheroids formation, treatment was carried out with BKM120, LEE011 and the combination of both agents. Due to limited material, we only analyzed the cell viability and apoptosis upon treatment and used one concentration for each drug based on pilot dose-response experiments.

As shown in Figure 27, the cell viability of primary MENX cells was reduced after treatment with both drugs and with the combination. Whereas LEE011 caused a slight but significant reduction of cell viability, BKM120 suppressed the cell viability to almost 50% compared to the controls. The strongest effect was observed using the combination of BKM120 and LEE011, which decreased cell viability below 50% versus the controls, significantly lower than individual drug treatments. This confirms the results we obtained from the cell lines in both 2D and 3D systems.

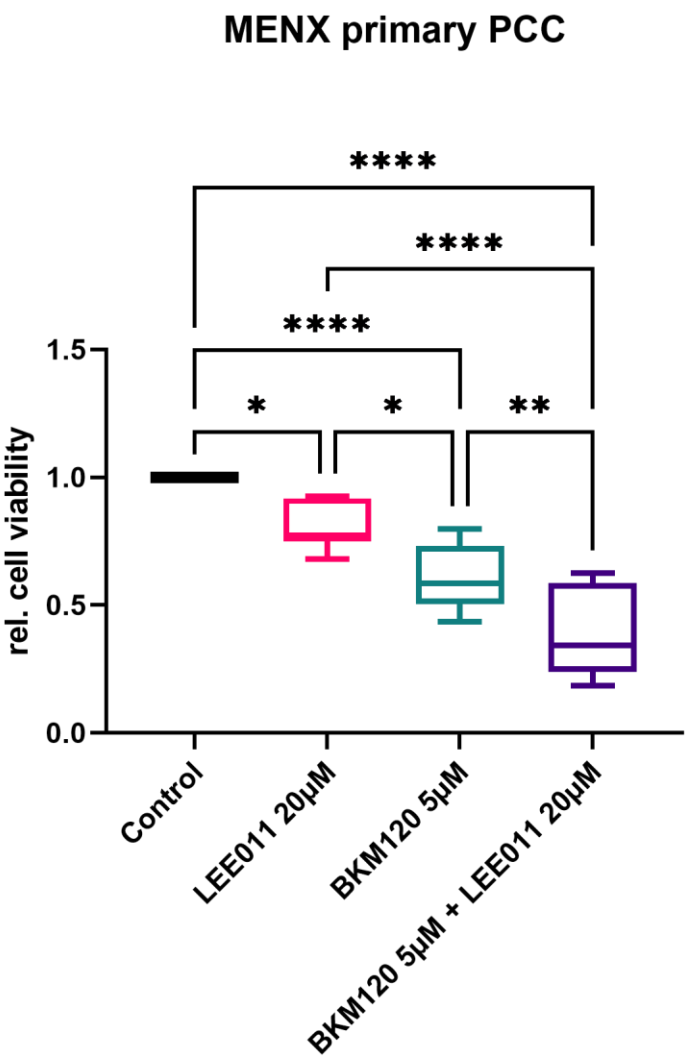

Figure 27: Cell viability of MENX primary cells in 3D
Primary cells were isolated from MENX PCCs and 3D spheroids generated using a hanging-drop system. Spheroids were treated with BKM120 (5µM), LEE011(20µM), a combination of both and DMSO for 72h after spheroid formation and cell viability was measured using cell viability assay. Shown is the relative cell viability normalized to the initial measurement and the DMSO control. Data shows the min to max box plot from primary cells of 7 rats with 5-15 technical replicates each (depending on the total amount of cells). 1way ANOVA. ns, not significant; *, p< 0.05; **, p< 0.01; ***, p<0.001; ****, p< 0.0001

3.1.8 3D MENX PCC apoptosis upon treatment

To further investigate the effect of the drugs on the primary tumor spheroids, we also analyzed their ability to induce apoptosis in this experimental system. Generation of spheroids was done as described above, and cells were treated with the drugs or DMSO as control. Apoptosis was assessed by using a 3D apoptosis assay measuring AnnexinV on the plasma membrane, a marker for early apoptosis. Therefore, the 30h timepoint after treatment start was chosen instead of the usual 72h. As shown in Figure 28, both BKM120 and the combination but not LEE011 were able to induce apoptosis in the primary MENX cells. The signal was significantly higher than the DMSO control, but no difference between BKM120 and the combination could be observed.

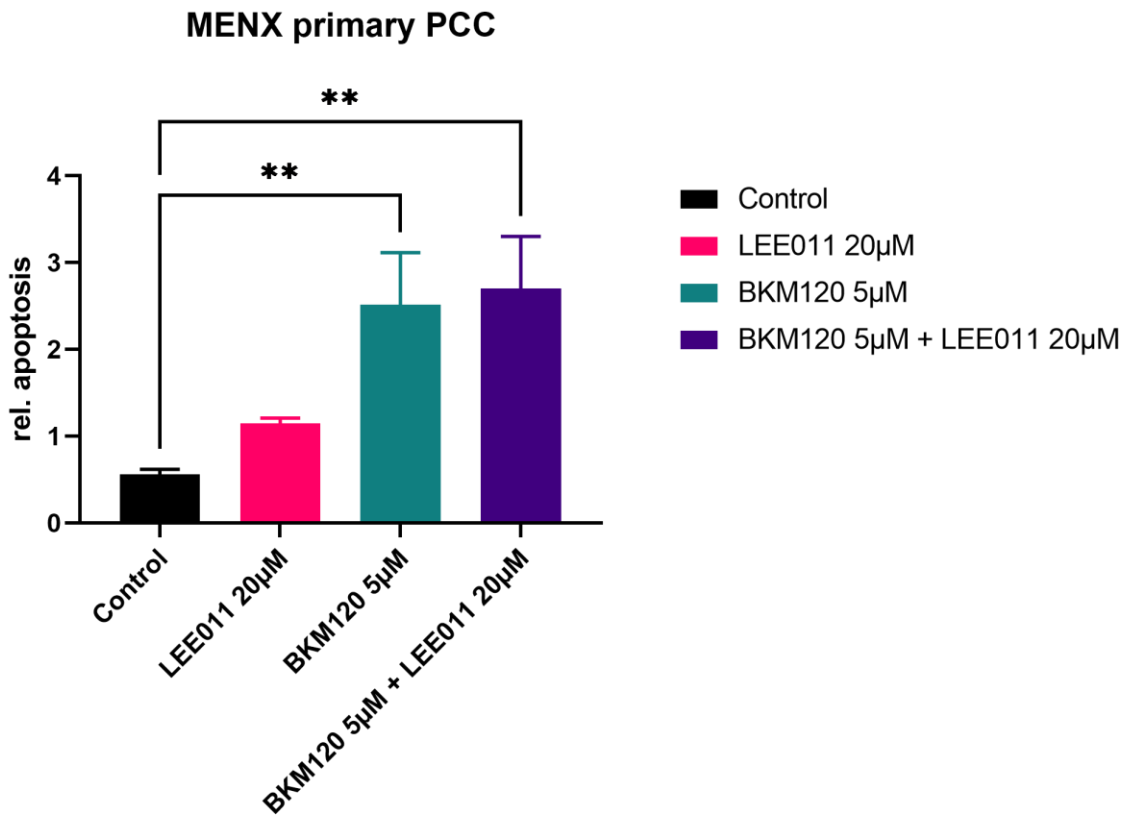

Figure 28: AnnexinV signal in 3D MENX PCCs
Primary cells were isolated from MENX PCCs and 3D spheroids generated using a hanging-drop system. Spheroids were treated with BKM120(5µM), LEE011(20µM), a combination of both and DMSO after spheroid formation. AnnexinV signal was measured after 30h to assess apoptosis. Shown is the relative apoptosis normalized to the DMSO control. Data shows the mean ±SD from primary cells of 3 rats with 8 technical replicates each. 1way ANOVA. ns, not significant; *, p< 0.05; **, p< 0.01; ***, p<0.001; ****, p< 0.0001

3.1.9 Treatment of primary human PPGL cells

In collaboration with our clinical partners, we were able to obtain fresh human PPGL tissues from a total of six patients. After isolation of the primary cells from these tumors, spheroids were generated using a hanging-drop system, similar to MENX-derived primary tumor spheroids.

As done for the rat cells, we treated the human PPGL cells after spheroid formation with our drugs and measured their viability. The results are illustrated in Figure 29. Whereas LEE011 showed a trend on reducing cell viability which was however not significant, both BKM120 and the combination significantly and strongly reduced the cell viability compared to the DMSO control. The combination seemed to be more effective than BKM120 alone, but the difference between these two treatments was not significant.

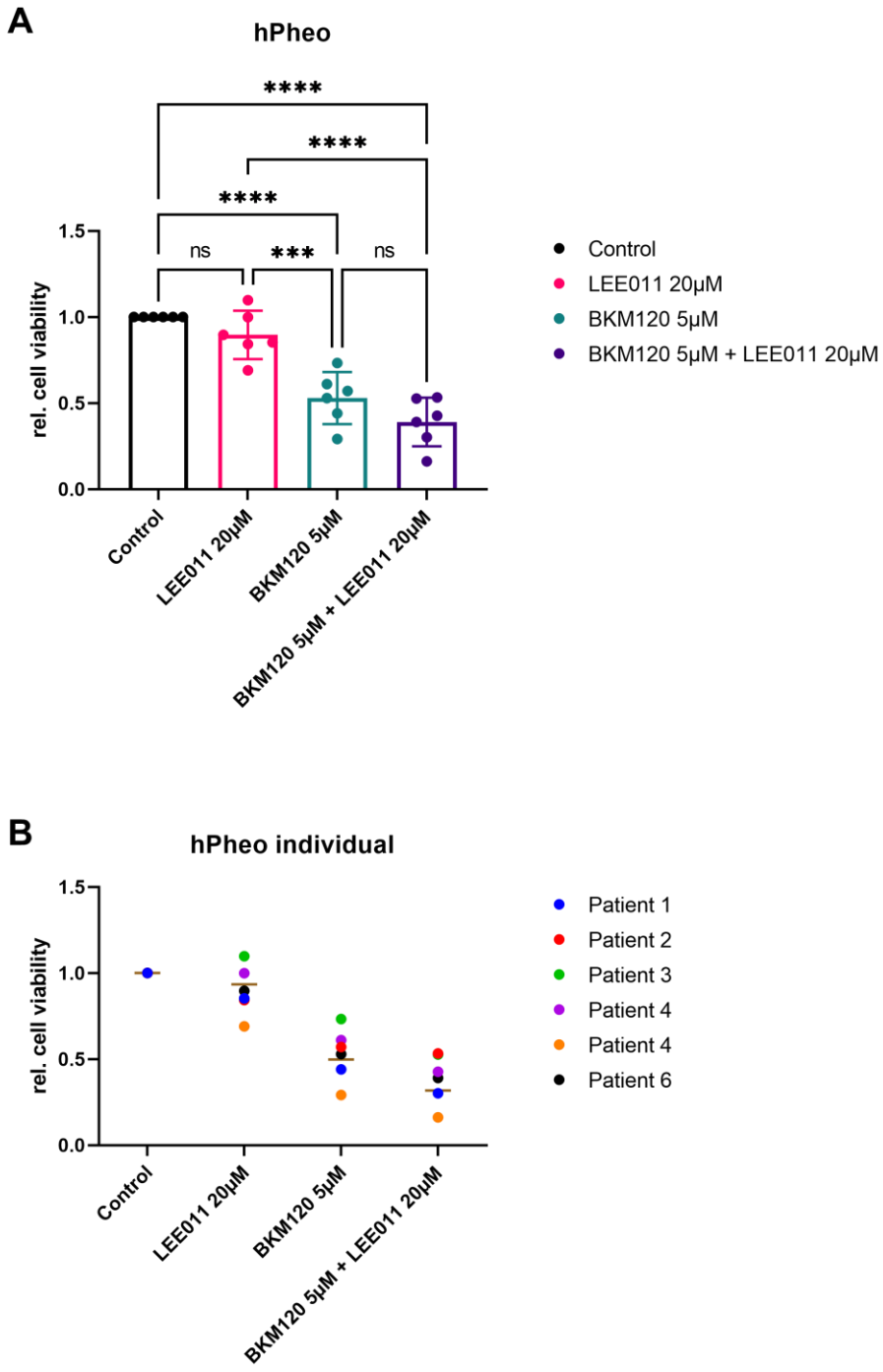

Figure 29: Cell viability of primary human PPGL spheroids
Primary cells were isolated from tumors obtained from human patients and 3D spheroids generated using a hanging-drop system. Spheroids were treated with BKM120 (5µM), LEE011 (5µM), a combination of both and DMSO for 72h after spheroid formation and cell viability was measured using cell viability assay. Shown is the relative cell viability normalized to the initial measurement and the DMSO control. In (A) the mean ±SD from primary cells of 6 patients with 4-8 technical replicates each (depending on total amount of cells) is shown, whereas (B) allows to follow the response of the individual cultures. 1way ANOVA. ns, not significant; *, p< 0.05; **, p< 0.01; ***, p<0.001; ****, p< 0.0001

3.1.10 Tumor growth of treated PC12 Xenografts in immunodeficient mice

After the promising *in vitro* data, we set out to investigate the effects of BKM120 and LEE011 treatments in an *in vivo* setting. For this, we injected PC12 cells subcutaneously in immunodeficient CD1 mice to generate xenograft-tumors. We started the treatment of the mice two weeks after cell injection when the tumors had reached a size of approximately 100mm^3. Xenograft-bearing mice were then treated with LEE011, and BKM120 alone or with two different combinations of both drugs or with a vehicle for 21 days, as illustrated in Figure 30 A. We used two different concentrations of the drugs in the combination treatment to see whether a lower concentration of the drugs would still have a beneficial effect. During treatment, tumor volume was longitudinally measured twice a week using a caliper. At the end of the study, the xenografts were collected for further analysis.

As shown in Figure 30 B, at the end of the study we observed a reduction in tumor growth upon treatment. In detail, BKM120 and both combination groups reduced tumor growth significantly, whereas LEE011 only showed a trend towards a reduction. BKM120 worked better as a single drug compared to LEE011 alone, and both combinations reduced the tumor volume significantly more than BKM120 or LEE011 alone. The strongest effect was observed with the combination of 25mg/kg BKM120 and 75mg/kg LEE011. It is important to note that the combination group with the lower doses gave better results than the higher concentrations of each single drug. By combining the two drugs, we can decrease their dose, thereby potentially reducing their side effects while maintaining their anti-tumor effects.

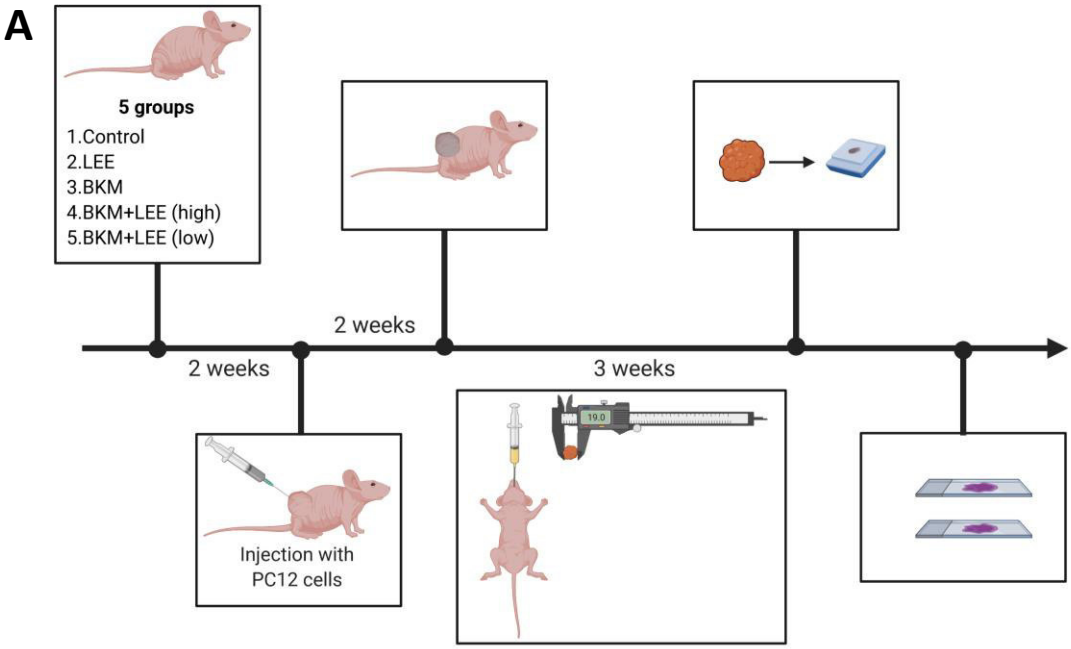

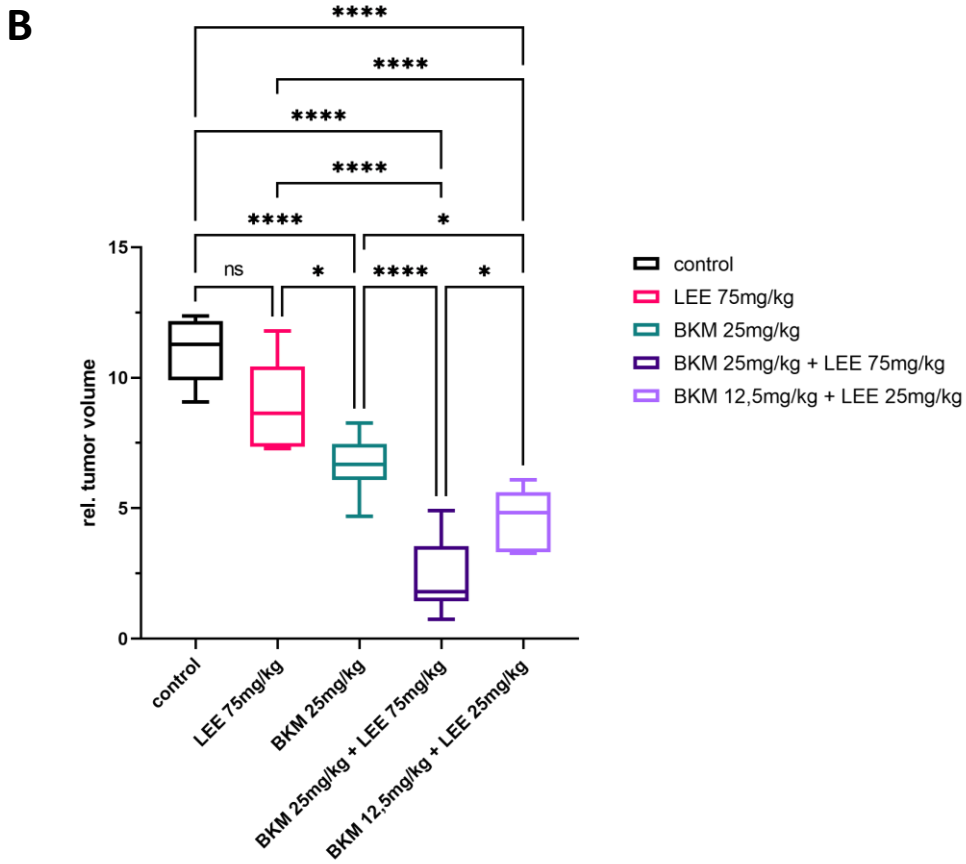

Figure 30: Tumor growth of treated PC12 Xenografts
In (A) a schematic illustration of the Xenograft experiment is shown. Two weeks after injection of PC12 cells the treatment was started. Treatment lasted for three weeks with caliper measurements twice a week. The 5 treatment groups were: 1. Vehicle control; 2. LEE011 75mg/kg; 3. BKM120

25mg/kg; 4. BKM120 25mg/kg + LEE011 75mg/kg; 5. BKM120 12.5mg/kg + LEE011 25mg/kg. (B) shows the relative tumor volume compared to the beginning of treatment. Mice were treated daily with oral gavaging for three weeks with the different drugs as shown in (A). 1way ANOVA. Data shows the min to max box plot from tumors of 6-8 mice per group after outlier removal in GraphPad Prism using ROUT method . 1way ANOVA. ns, not significant; *, p< 0.05; **, p< 0.01; ***, p<0.001; ****, p< 0.0001 Created with BioRender.com

3.1.11 Histological analysis of the xenografted tumors

At the end of the *in vivo* therapy, the tumorgrafts were collected and embedded in paraffin blocks to allow further examination. Our aim was to investigate whether the differences in tumor growth upon treatment might be due to changes in cell proliferation. Therefore, we stained sections of the embedded tumors with the proliferation marker NuSAP. NuSAP is a protein involved in spindle-formation and can be used as a marker of proliferation [138, 139]. Stainings with a specific anti-NuSAP antibody showed a decrease in the number of positive nuclei in the tumors following treatment, as shown in Figure 31. In detail, all treatments significantly reduced the positive cells per area in the tumors. There was a trend towards a stronger reduction in the tumors treated with the higher dose of the combination, whereas the lower dose reduced cell proliferation as effectively as the higher doses of the single drugs.

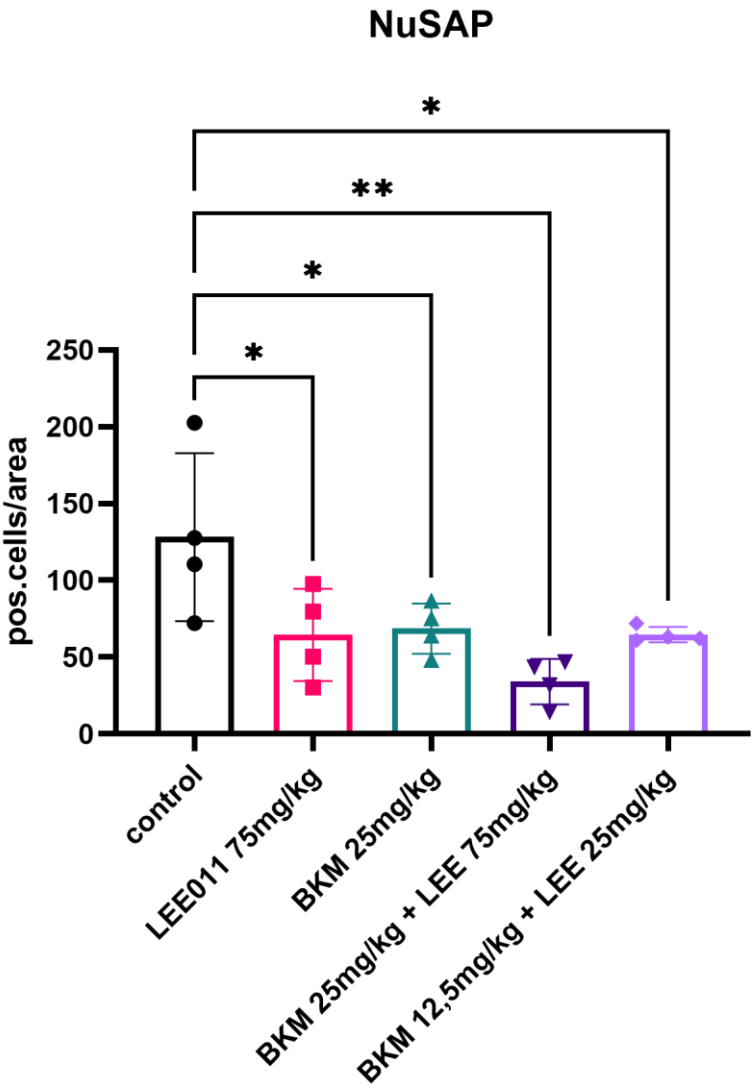

Figure 31: Histological stainings of Xenografts
IHC staining was performed on tissues from the xenografted tumors using a specific anti-NuSAP antibody. After stainings were performed, positive cells were counted using ImageJ. Data shows the mean ±SD from three slides and three pictures per slide of each treatment group. 1way ANOVA. *, p< 0.05; **, p< 0.01

3.1.12 Summary

The goal of this study was to find a novel treatment approach for PPGLs. To our knowledge, this is the first study combining a PI3K/AKT and a CDK4/6 inhibitor in PPGLs. We could show that both BKM120 and LEE011 show an effect on PPGL cells when used alone and that the combination of both is enhancing the treatment effects. In detail, we showed downregulation of 2D cell proliferation, 3D cell viability and 3D spheroid growth in PC12 and MPC cells upon treatment with the drug combination giving significantly better results compared to the single drugs. We also could show the induction of apoptosis upon treatment with BKM120 alone and in combination in both 2D and 3D systems. Additionally, PC12 cells also showed a reduction of migration and invasion after being treated with the drugs. In line with this, cultures from human PPGL tissues also responded to our treatment approach, even if the combination only showed a trend toward better reduction of cell viability compared to BKM120 alone. An *in vivo* treatment of xenografted PC12 tumors showed great potential in terms of reducing tumor growth. Here, the combination of BKM120 and LEE011 gave the best results, allowing to lower the doses of the single drugs by half and still maintaining an excellent treatment effect.

3.2 Molecular based therapy of pNETs by targeting PI3K and CDK4/6

3.2.1 2D Treatment of pNET cell lines with BKM120 and LEE011 in vitro reduces cell proliferation

We first set out to test the effect of the PI3K inhibitor BKM120 and the CDK4/6 inhibitor LEE011 on pNET cells in cell culture. For this, we used the two pNET cell lines INS-1E and NT3. INS-1E cells derive from pancreatic beta cells, are of rat origin and are widely used as a pancreatic islet cell line. NT3 cells are of human origin and are one of the only functional human pNET cell lines available. For the studies, the cells were treated for 72h with the two mentioned compounds as single drugs, with a combination of both or with DMSO as control. After the treatment we measured the cell proliferation of the cells grown as 2D cell cultures. As shown in Figure 32, INS-1E cells responded well to the treatments, and the individual drugs were able to reduce cell proliferation in a dose-dependent manner. The combination of BKM120 + LEE011 showed the strongest effect and also had the lowest IC50. The single treatment with LEE011 had the weakest effect and needed higher doses to decrease proliferation. Considering the IC50, using the combination allowed to reduce the drug concentration by <50% to reach effects that are equally good or even better as the single drugs.

NT3 cells responded to BKM120 and LEE011 differently from INS-1E cells (Figure 33). The drugs reduced cell proliferation in all treatment groups to a minimum of 70%. Comparing the treatments, BKM120 and LEE011 had a similar effect resulting in comparable IC50 values. Also here, the combination showed a better effect with an IC50 value that was 50% reduced. It has to be noted that overall the standard deviation was quite high, making it difficult to compare the treatment groups. In general, the effect of the drugs was remarkably lower for NT3 cells than for the INS-1E cells, giving IC50 values 20-30 fold higher in the former. The differences between the two cell lines can be explained by the slow-growing behavior of NT3 cells. Indeed, it has been reported that NT3 cells show a low Ki67 labeling index compared to other

cells and have a doubling time of around 11 days [140]. Due to the slow growth, the assessment of cell proliferation for 72h is maybe not long enough to see differences. This issue will be addressed in chapter 3.2.5.

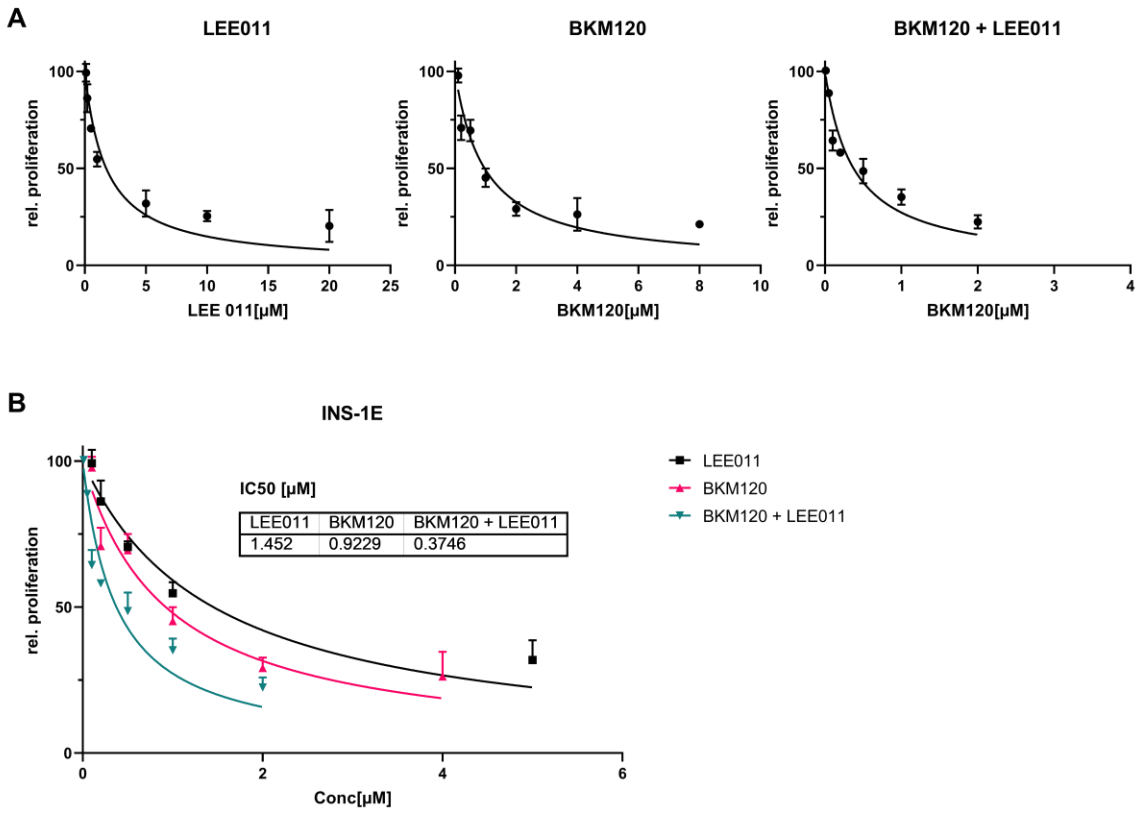

Figure 32: Effect of BKM120 and LEE011 on cell proliferation in INS-1E cells
INS-1E cells were treated with LEE011, BKM120, a combination of both drugs or DMSO as control in a 2D system. Cell proliferation was measured after 72h of treatment. Different concentrations were used to determine the IC50 values of the single drugs and the combination (Table 16). To evaluate the drug response, the DMSO control was set to 100% and nonlinear regression was used to determine the IC50. Data shows the mean ±SD from 3 independent experiments with 3 technical replicates each.

Table 16. Doses used for treatment of INS-1E and NT3 cells

LEE011 [µM]	BKM 120 [µM]	BKM120 + LEE011 [µM]
0.2	0.05	0.05 + 0.2
0.4	0.1	0.1 + 0.4
0.8	0.2	0.2 + 0.8
2	0.5	0.5 + 2
4	1	1 + 4
8	2	2 +8
16	4	4 +16

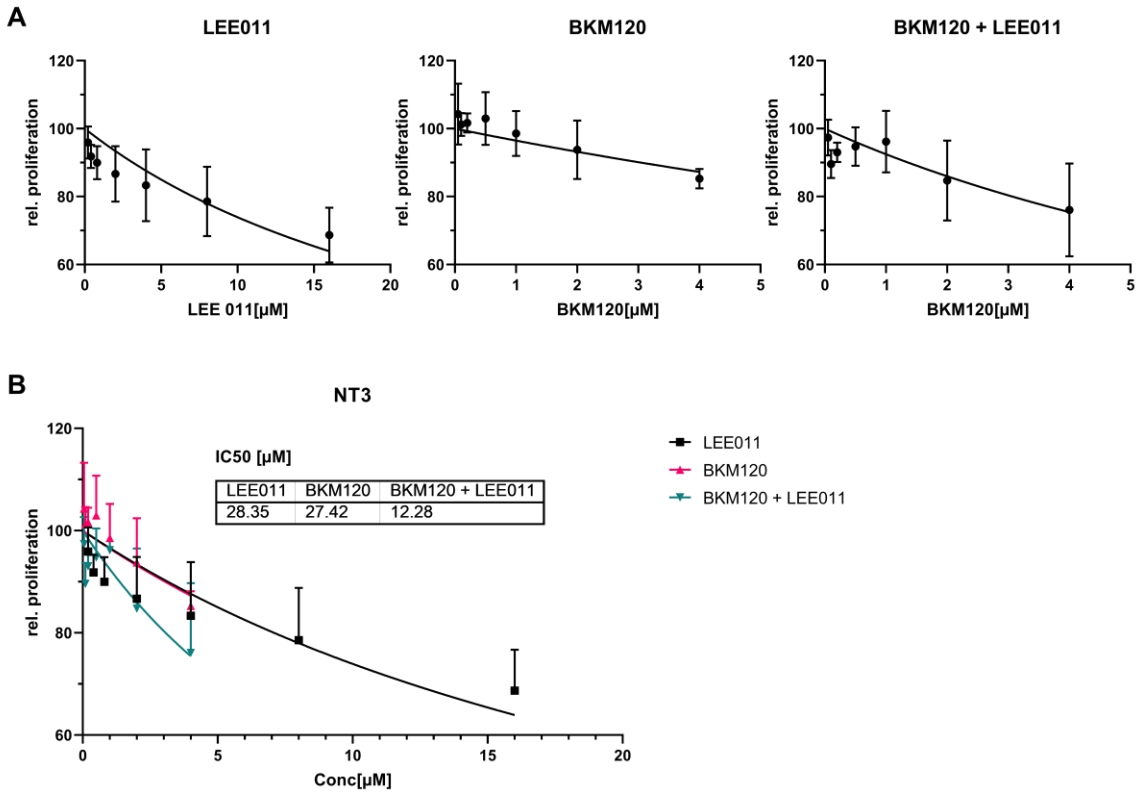

Figure 33: Effect of BKM120 and LEE011 on cell proliferation in NT3 cells
NT3 cells were treated with LEE011, BKM120, a combination of both drugs or DMSO as control in a 2D system. Cell proliferation was measured after 72h of treatment. Different concentrations were used to determine the IC50 values of the single drugs and the combination (Table 16). To evaluate the drug response, the DMSO control was set to 100% and nonlinear regression was used to determine the IC50. Data shows the mean ±SD from 3 independent experiments with 3 technical replicates each.

3.2.2 Apoptosis induction of pNET cell lines grown in 2D upon treatment with BKM120 and LEE011

To test whether the selected drugs not only reduce proliferation but also induce apoptosis of pNET cells, we measured Caspase9 activity in both cell lines after 72h of treatment. As shown in Figure 34 A+B, in INS-1E cells both BKM120 and the combination induced apoptosis in a dose-dependent manner, whereas LEE011 alone did not show any apoptotic signal. Direct comparison showed that there is no difference between BKM120 and the combination, indicating that only BKM120 promotes apoptosis.

Interestingly, the NT3 cells (Figure 34 C+D) showed a different behavior. While similar to INS-1E cells only BKM120 and the combination induced apoptosis, the observed pattern was different. Low concentrations of both BKM120 and the combination showed no effect, and apoptosis was induced starting from a certain concentration. Comparing BKM120 and the combination treatment, we found that the latter worked significantly better, inducing apoptosis already at lower concentrations. This suggests a synergistic activity of LEE011 when combined with BKM120.

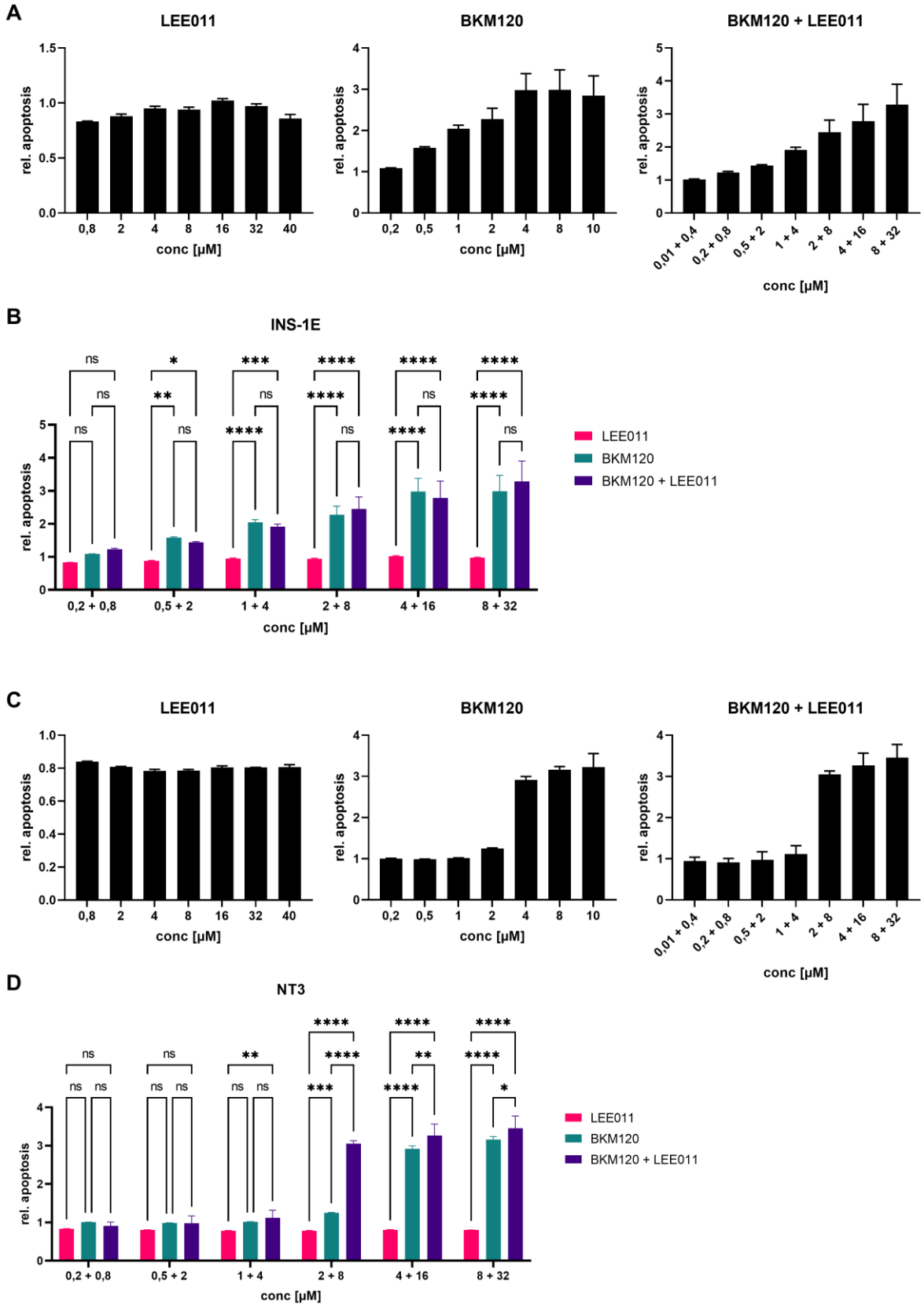

Figure 34: Apoptosis induction upon treatment in PC12 and MPC cells
INS-1E (A,B) and NT3 (C.D) cells were treated with LEE011, BKM120, a combination of both drugs or DMSO as control in a 2D system. Caspase 9 activity was measured after 72h of treatment and used

as readout for apoptosis. A range of concentrations as shown in the panels was used to evaluate the effect of the drugs. A and C show an overview of the different treatments, while in B and D the different treatments are directly compared. Shown is always the relative apoptosis normalized to the DMSO control. Data shows the mean ±SD from 3 independent experiments with 3 technical replicates each. 2way ANOVA. ns, not significant; *, p< 0.05; **, p< 0.01; ***, p<0.001; ****, p< 0.0001

3.2.3 Migration and invasion behavior of INS-1E and NT3 cells

After observing a reduction of proliferation and induction of apoptosis in pNET cells upon BKM120 and LEE011 treatment, we set out to investigate whether these drugs affect cell migration and invasion. Both are important processes involved in tumorigenesis, and a treatment that also inhibits migration and/or invasion would have further clinical impact. We chose a 2D Boyden chamber system and plated INS-1E and NT3 cells in migration and invasion inserts. Unfortunately, both cell lines did not show any potential to migrate and invade (Figure 35). INS-1E cells attached well to the surface of the inserts, but no cells migrated or invaded through the inserts, as shown by the absence of cells at the bottom of the insert. Similarly, NT3 cells did not migrate nor invade. Interestingly, only a few cells could be detected on the surface of the inserts, suggesting that the NT3 cells could not properly attach to the surface.

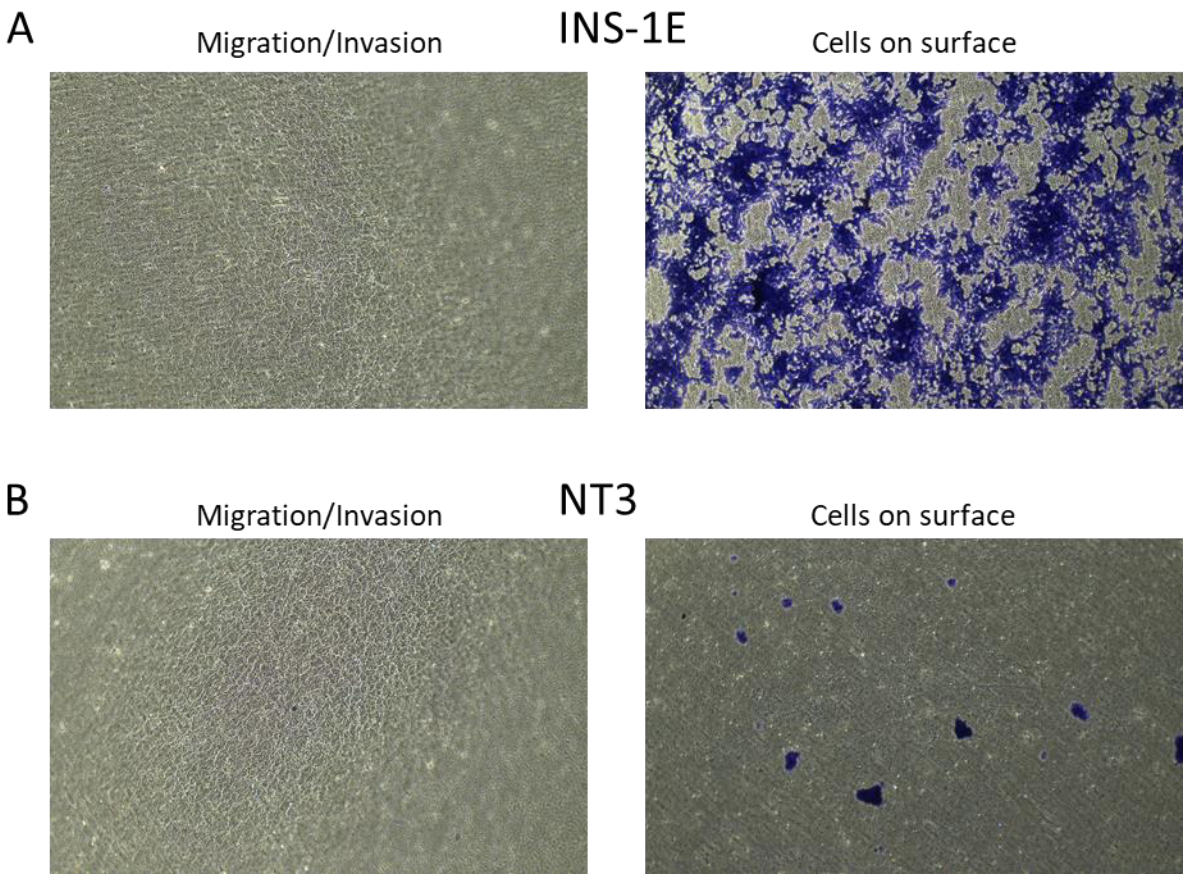

Figure 35: Migration and Invasion of pNET cell lines
INS-1E and NT3 cells were plated in invasion chambers containing Matrigel or migration chambers without Matrigel. The amount of migrating and invading cells was assessed 72h after plating. Shown is the amount of INS-1E (A) and NT3 (B) cells on the bottom(left panel) and the surface (right panel) of the inserts. Shown are representative pictures from three independent experiments with three replicates each.

3.2.4 WB and qPCR analysis of INS-1E and NT3 cells treated with BKM120 and LEE011

We could show that in a 2D system, our treatment approach was able to reduce cell proliferation and induce apoptosis in both pNET cell lines. Before continuing our treatment approach and assessing more parameters, we wanted to make sure that the drugs inhibited the PI3K/AKT (BKM120) or the CDK4/6 (LEE011) pathway so that the observed phenotypes are explained by pathway inhibition and not by unspecific effects. Therefore, we set out to assess different downstream signals by WB and qPCR.

For the PI3K/AKT pathway, we analyzed the phosphorylation of AKT and S6. Both are well-known members and downstream targets of the PI3K pathway. As shown in Figure 36, treatment with BKM120 and the combination significantly reduced both the pAKT/AKT - and the pS6/S6 signal ratio in INS-1E and NT3 cells. Treatment with DMSO (control) and LEE011 had no effect on pAKT/AKT and pS6/S6. This confirms the downregulation of the PI3K/AKT pathway after treatment with the PI3K inhibitor BKM120.

Confirmation of CDK4/6 downregulation was carried out by analyzing the expression of *Ccna1* and *Pcna*, two genes that are involved in the CDK-pRB-E2F and cell cycle signaling. Figure 37 shows a strong reduction of both target genes in samples treated with LEE011 alone and with the combination of BKM120 and LEE011. The reduction of gene expression can be seen in both pNET cell lines, indicating that the treatment with LEE011 downregulates the CDK4/6 signaling.

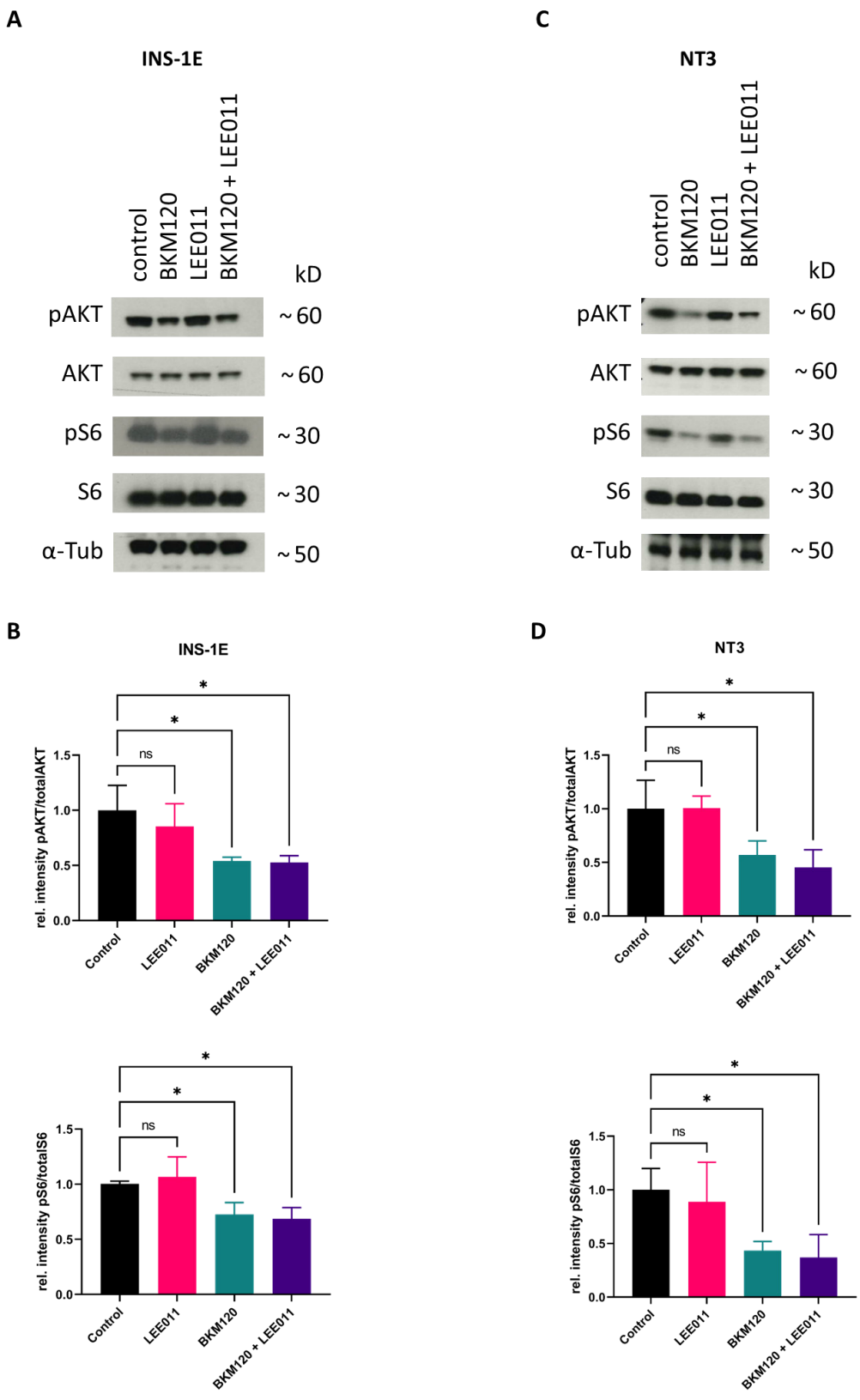

Figure 36: WB for PI3K pathway targets in INS-1E and NT3 cells
A and C show immunoblots representing phospho-Akt (pAKT), total Akt, phospho- S6 (p-S6), total S6 and α-Tubulin. Shown is one representative immunoblot out of three experiments. B and D show graphs representing the ratio of pAkt over total Akt and pS6 over total S6. Data shows the mean ±SD from three independent experiments. 1way ANOVA, ns, not significant; *, p< 0.05;

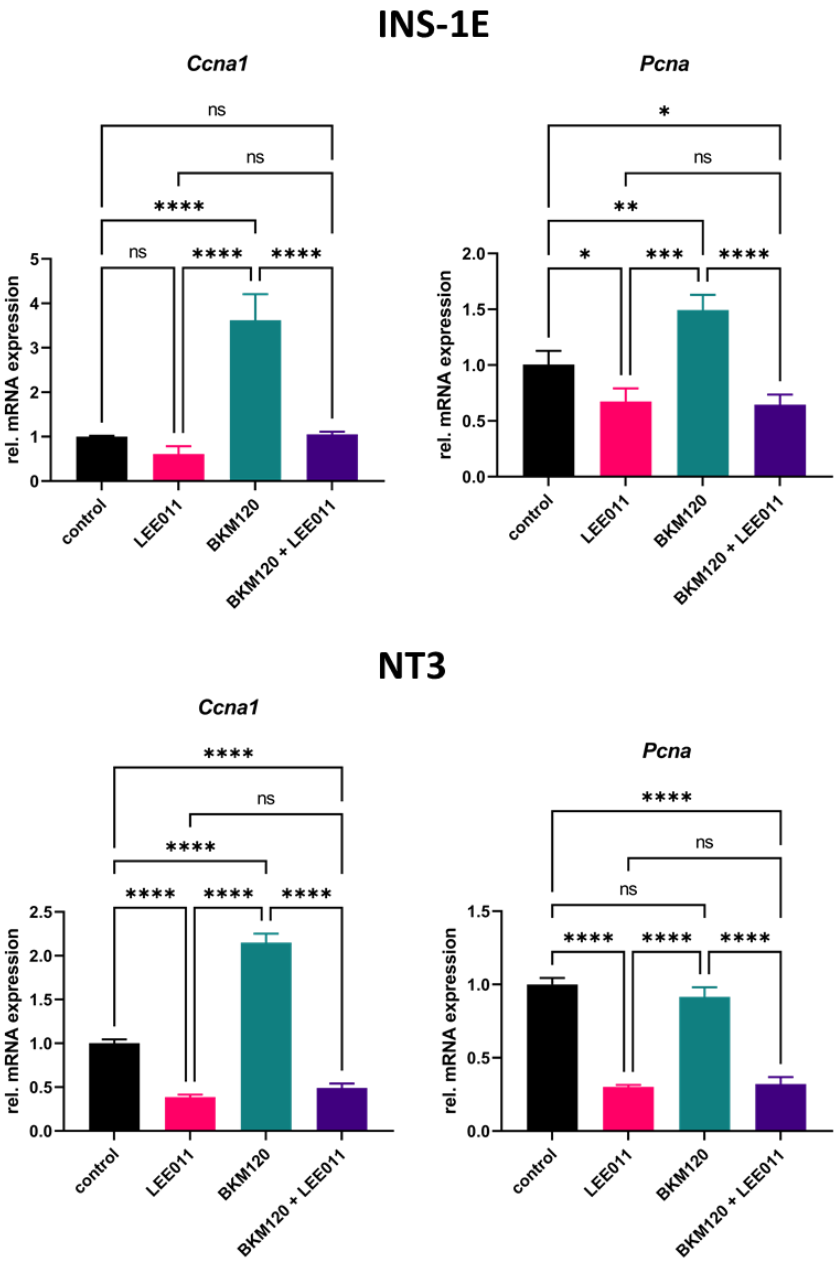

Figure 37: qPCR analysis of INS-1E and NT3 cell after treatment
INS-1E and NT3 cells were plated in 2D cell culture. After 72h of treatment with BKM120, LEE011 and BKM120 + LEE011 using IC50 values, pellets were collected and RNA isolated. Gene expression for Ccna1 and Pcna was carried out using TaqMan probes. Data represent the mean ±SD from three independent biological replicates. 1way ANOVA ns, not significant; *, p< 0.05; **, p< 0.01; ***, p<0.001; ****, p< 0.0001

3.2.5. 3D cell viability and spheroid growth in INS-1E and NT3 cells upon treatment

We set out to establish and treat both pNET cell lines grown as 3D cultures. Given that 3D cell cultures resemble more closely an *in vivo* situation and enable a better crosstalk of cells, it can also be seen as an intermediate step in between traditional 2D cell culture and possible *in vivo* treatments. Our goal was to investigate whether our treatment approach would show the same effects in 3D as seen in 2D cell cultures.

Cells were seeded in ULA plates, and they formed 3D spheroids within a few days. Upon spheroid formation, we treated the cells with BKM120, LEE011, a combination of both drugs or DMSO as a control for 72h. Cell viability was assessed at the start and after 24h, 48h and 72h of treatment.

As shown in Figure 38, both drugs were able to reduce the viability of INS-1E cells when used individually, with BKM120 showing the stronger effects. At the highest concentrations, both single drugs and the combination reduced cell viability to a minimum. In case of the combination, even the second-highest doses (BKM120 5µM + LEE011 20µM) were able to reach these minimum values. Looking at the 72h timepoint, the combination is significantly more effective in the middle-range doses compared to both the single treatments. Moreover, even at the low doses it shows a superior effect over LEE011 alone and a trend towards a better efficacy than BKM120 alone.

Looking at the NT-3 cells (Figure 39), cell viability in the controls and overall was lower than in INS-1E cells, which also resulted in less strong effects of the treatment. Nevertheless, both BKM120 and LEE011 as well as the combination reduced the cell viability and at higher concentrations the viability was even lower than at the beginning. Taking a look at the 72h time point, the combination worked significantly better than both the single drugs in the middle-range concentrations and better than LEE011 in almost all cases. This confirms the good treatment effects in both cell lines and shows that assessing cell viability in NT3 cells is a good readout despite the low proliferation of the NT3 cells.

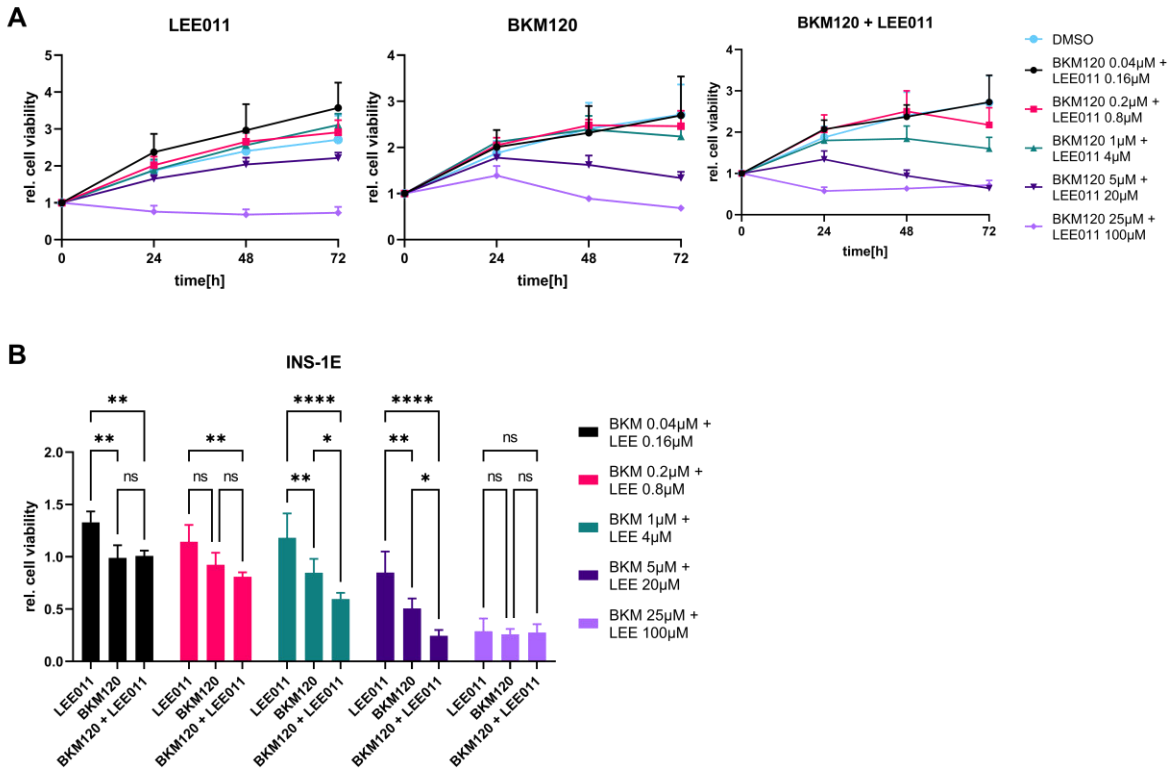

Figure 38: 3D cell viability in treated INS-1E cells

INS-1E cells were treated with LEE011, BKM120, a combination of both drugs or DMSO as control in a 3D system using ULA plates. Cell viability was measured after the addition of drugs and after 24h, 48h, 72h. A range of concentrations as shown in the panels was used to evaluate the effect of the drugs. A shows the overview of each drug treatment over 72h, whereas in B the comparison of the treatments with different concentrations at the 72h timepoint is shown. Shown is the relative cell viability normalized to the initial measurement and the DMSO control. Data shows the mean ±SD from 3 independent experiments with 8 technical replicates each. 2way ANOVA. ns, not significant; *, p< 0.05; **, p< 0.01; ***, p<0.001; ****, p< 0.0001

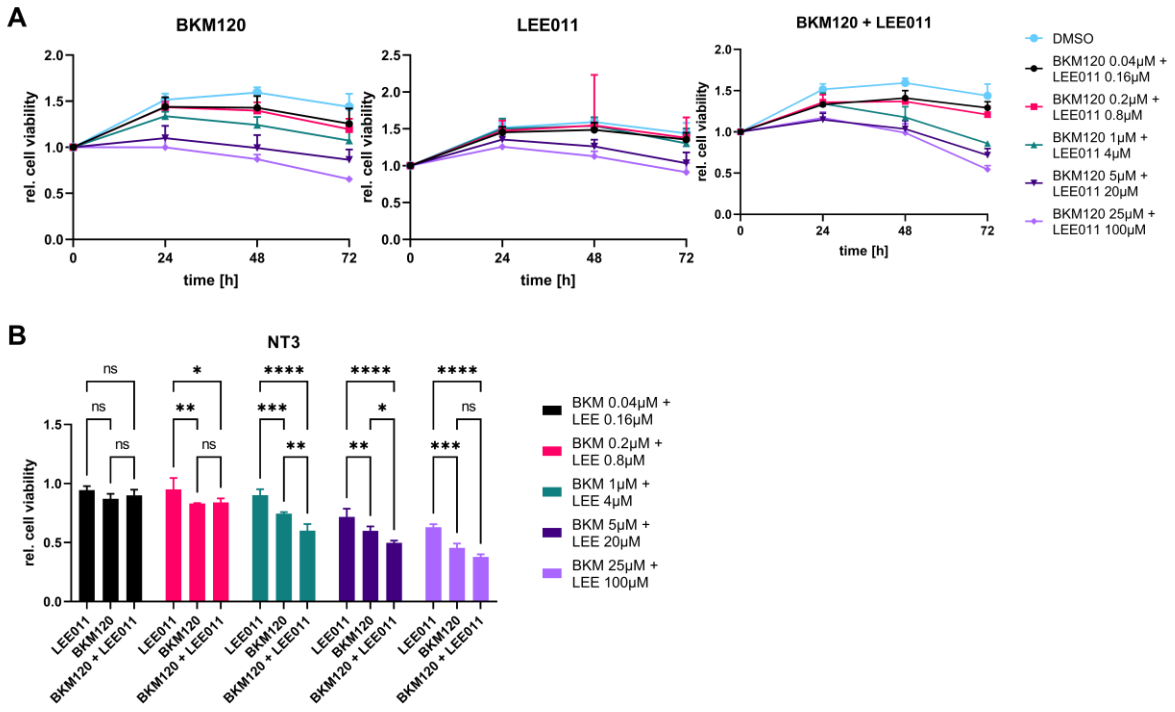

Figure 39: 3D cell viability in treated NT3 cells

NT3 cells were treated with LEE011, BKM120, a combination of both drugs or DMSO as control in a 3D system using ULA plates. Cell viability was measured after the addition of drugs and after 24h, 48h, 72h. A range of concentrations as shown in the panels was used to evaluate the effect of the drugs. A shows the overview of each drug treatment over 72h, whereas in B the comparison of the treatments with different concentrations at the 72h timepoint is shown. Shown is the relative cell viability normalized to the initial measurement and the DMSO control. Data shows the mean ±SD from 3 independent experiments with 8 technical replicates each. 2way ANOVA. ns, not significant; *, p< 0.05; **, p< 0.01; ***, p<0.001; ****, p< 0.0001

Additionally, we also set out to investigate the growth of the treated spheroids over a time of 14 days. This allows us to assess the effect of the drugs over a longer period of time. Spheroids were generated using ULA plates and then treated for 14 days with the drugs. The spheroid size was measured at the start of the treatment and at Days 3, 7, 11 and 14. As shown in Figure 40 A, INS-1E cells form nice spheroids, and an effect of the treatment in terms of size and darkening of the spheroids can be seen already after three days of treatment with the drug combination. BKM120 and the drug combination of BKM120 + LEE011 completely stopped spheroid growth, whereas LEE011 reduced it (Figure 40 B). Looking at the spheroid size after 72h, BKM120 and the combination worked better than LEE011 at suppressing cell growth, and there was a trend toward higher efficacy of the combination compared to BKM120 alone.

NT3 cells also formed spheroids in ULA plates, as shown in Figure 41 A, even though the spheroids seem to be more loose compared to the INS-1E cells. Also in NT3 cells, a clear reduction in size and a progressive darkening of the spheroids can be seen. Figure 41 B shows that all three treatments inhibited spheroid growth with BKM120 and the combination showing the strongest effect. While LEE011 suppressed spheroid growth, BKM120 and the combination even led to a slight reduction of spheroid size. As expected, the growth rate in the control NT3 spheroids is remarkably lower than that of INS-1E. Nevertheless, slight differences in spheroid size can already be seen after 72h of treatment.

Overall, in both cell lines the single drugs and the combination reduced the spheroid growth with BKM120 and the combination of BKM120 + LEE011 showing the strongest effects.

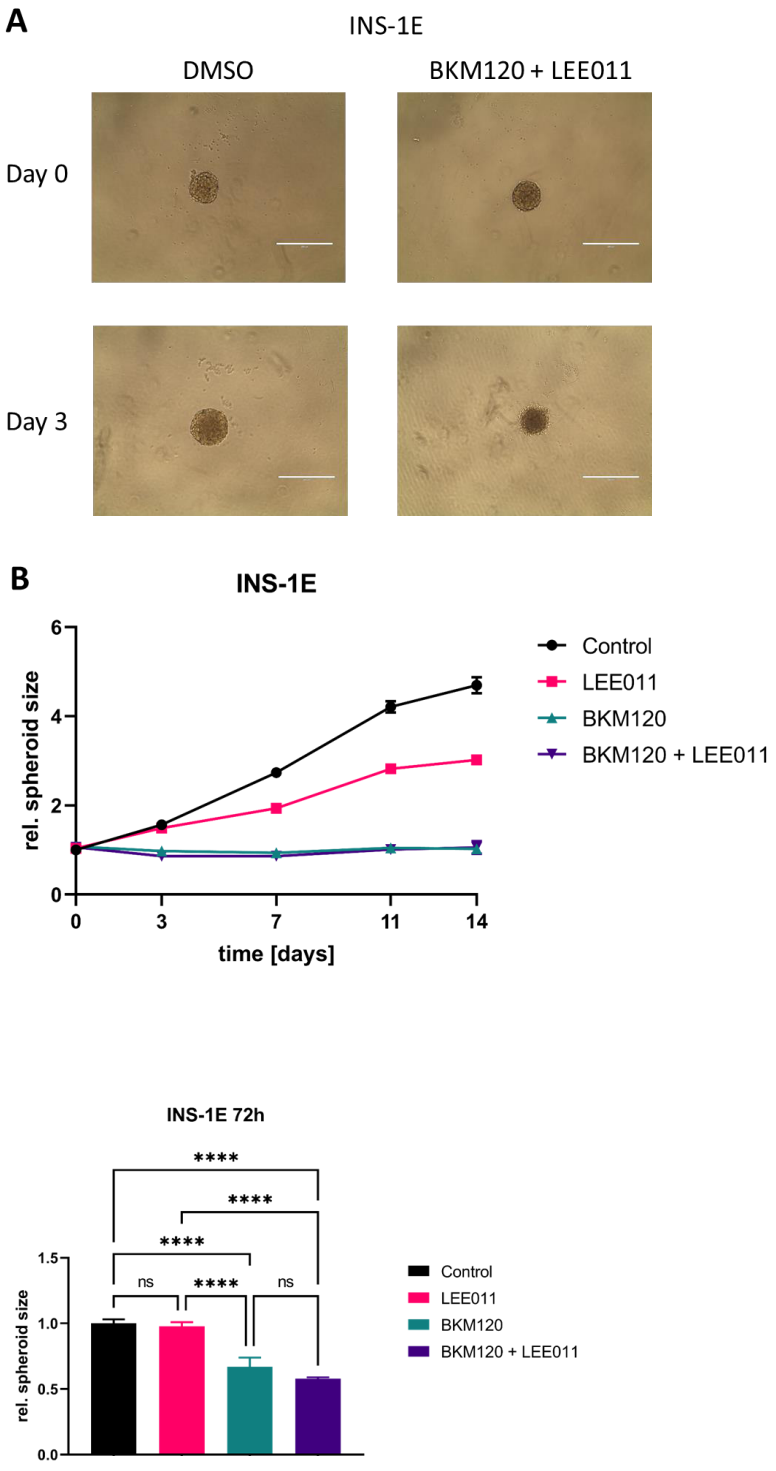

Figure 40: INS-1E spheroid growth
INS-1E cells were treated with LEE011 (20µM), BKM120 (5µM), a combination of both drugs or DMSO as control in a 3D system using ULA plates. Spheroid pictures were taken after the addition of drugs and after 3, 7, 11 and 14 days. Spheroid size was measured using ImageJ. (A) shows representative images of spheroids on Day 0 and Day 3 treated with DMSO (control) or the drug combination. (B) shows the rel. spheroid size over the course of 14 days with a statistical analysis of the 72h time point. Data shows the mean ±SD from 3 independent experiments with 8 technical replicates each. 1way ANOVA. ns, not significant; *, p< 0.05; **, p< 0.01; ***, p<0.001; ****, p< 0.0001

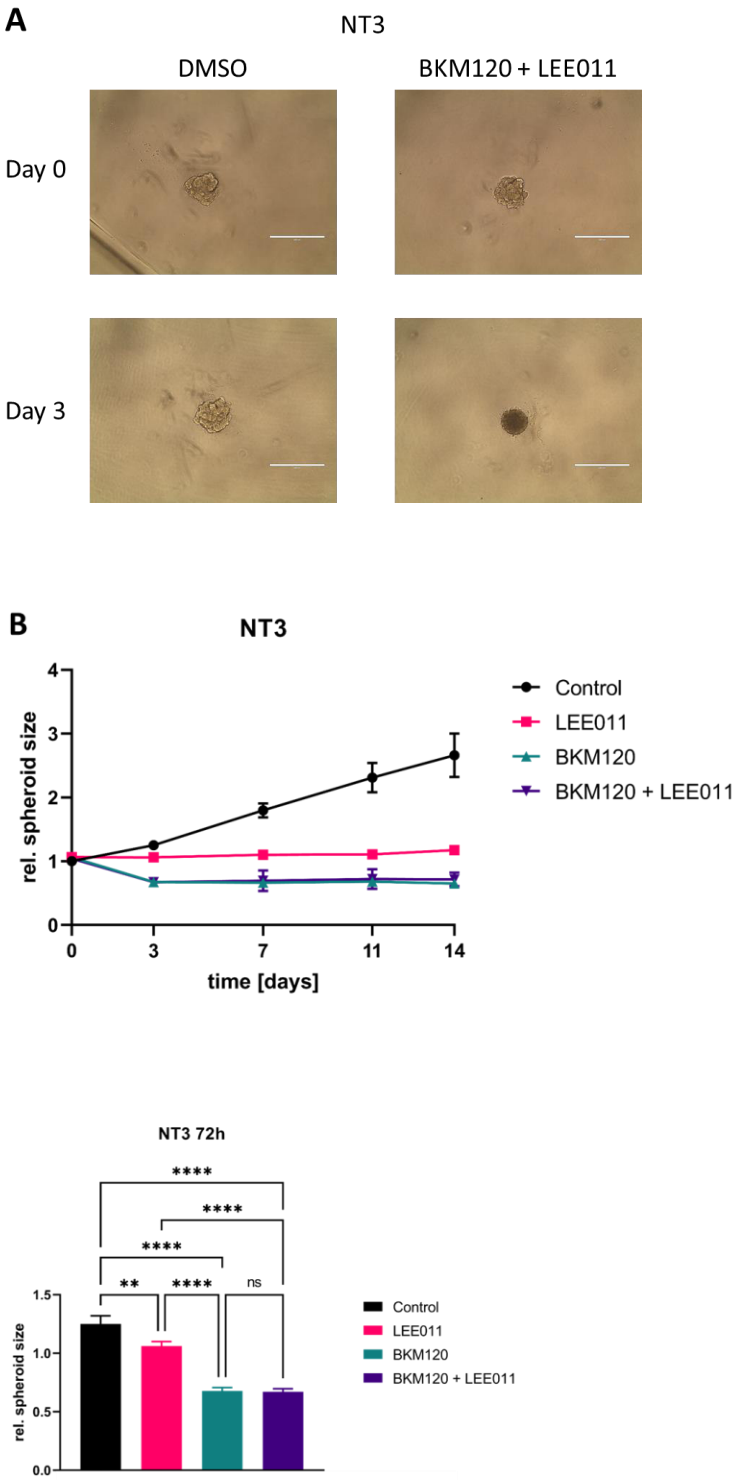

Figure 41: NT3 spheroid growth

NT3 cells were treated with LEE011 (20µM), BKM120 (5µM), a combination of both drugs or DMSO as control in a 3D system using ULA plates. Spheroid pictures were taken after the addition of drugs and after 3, 7, 11 and 14 days. Spheroid size was measured using ImageJ. (A) shows representative images of spheroids on Day 0 and Day 3 treated with DMSO (control) or the drug combination. (B) shows the rel. spheroid size over the course of 14 days with a statistical analysis of the 72h time point. Data shows the mean ±SD from 3 independent experiments with 8 technical replicates each. 1way ANOVA. ns, not significant; *, p< 0.05; **, p< 0.01; ***, p<0.001; ****, p< 0.0001

3.2.6 3D invasion of INS-1E and NT3 cells

As both pNET cell lines did not show any potential to migrate and invade in 2D, we tested if these cells would invade in a 3D system. After spheroid formation, Matrigel was added into the wells and medium containing the drugs or DMSO was added. Cells without Matrigel were used as growth controls. As shown in Figure 42, both cell lines did not show any potential to invade in the 3D context within 14 days of measurement. While both cell lines did show growth of the spheroid, no invading structures could be observed. Both INS-1E and NT3 cells do not show any invasion potential in 2D or 3D and therefore we cannot determine the effect of the drugs on these two processes.

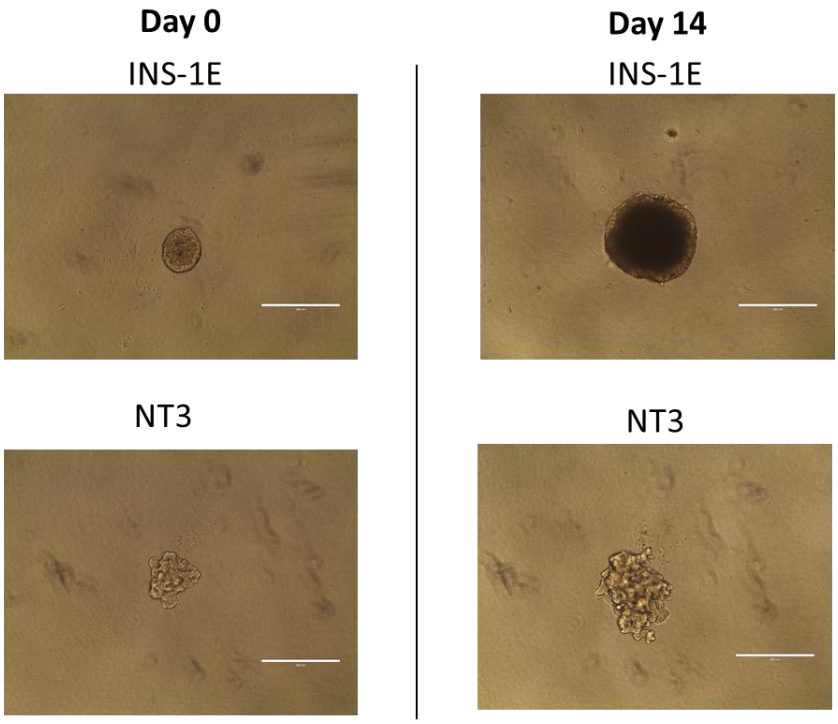

Figure 42: Invasion of pNET cell lines in 3D
INS-1E and NT3 cells were seeded in ULA plates and Matrigel was added after spheroid formation to observe invasion. Wells without Matrigel were used as growth control. Pictures were taken immediately after adding the Matrigel and after 14 days. Shown are representative pictures of three independent experiments with four replicates.

3.2.7 Treatment effects on 3D Men1 primary pNET cells

Giving the promising results we observed in 2D and 3D cultures of established cell lines, we set out to test our treatment approach on primary pNET cells. For this, we isolated pancreatic islets from Men1 mice. The Men1 mouse model is well suited for the study of NETs and especially of pNETs given that these mice develop pNETs that closely resemble human pNETs. To test our treatment strategy, we treated islets from both wild-type (n=5) and heterozygous *Men1*- deficient (n=9) animals to see the effect of the drugs on both healthy and tumor tissues. Islets were isolated by collagenase digestion and further teated with trypsin to obtain a single-cell suspension. These single cells were then plated into a hanging-drop system to generate 3D spheroids. Containing the same number of cells and having a similar size is an important issue given that the freshly isolated islets differ in size. These spheroids were treated with BKM120 and LEE011 and cell viability was assessed 72h later.

Figure 43 A shows that the treatment overall was effective in islets from heterozygous animals. Both BKM120 and LEE011 reduced the cell viability after 72h of treatment, with BKM120 working significantly better than LEE011. Moreover, the combination of BKM120 and LEE011 was the most effective treatment reducing cell viability the most. In contrast, neither of the single drugs nor the combination showed a significant reduction of cell viability in the islets of wild-type mice. There only seems to be a trend toward reduction in the BKM120 and the combination-treated samples (Figure 43 B). This shows that our treatment is highly effective in primary tumor cells and shows no side effects on cell from healthy animals. It has to be noted that the sample size for the wild-type mice (n=5) was considerably lower than that of the *Men1*-deficient mice (n=9), affecting statistical results.

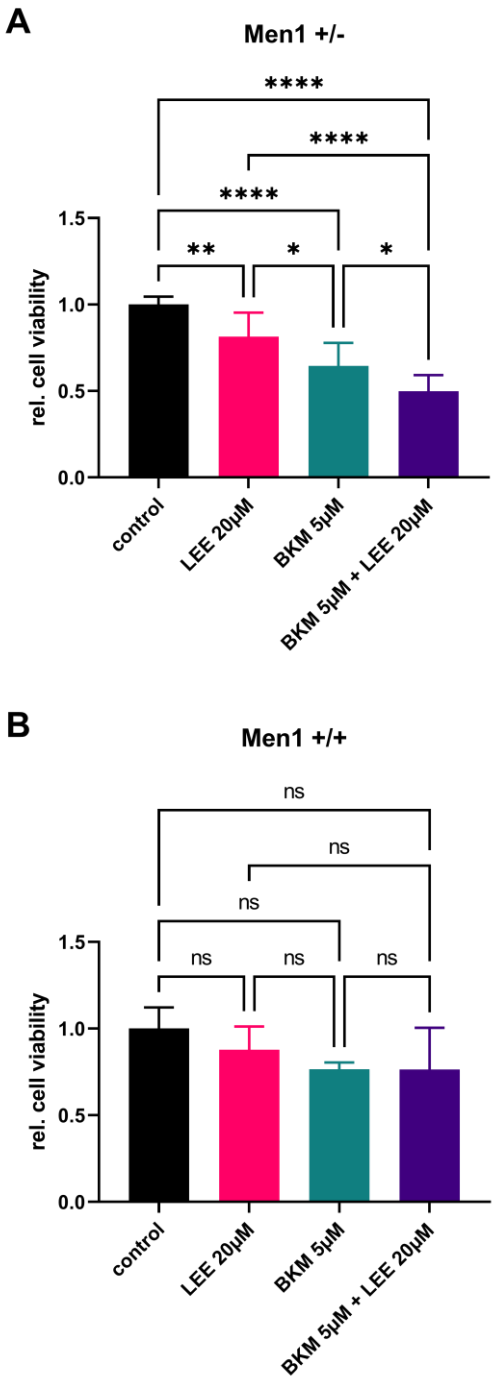

Figure 43: Treatment of primary islet cells from Men1 mice
Primary islets were isolated from *Men1* heterozygous (A) and *Men1* wild-type (B) mice. Single cells were obtained out of the islets and 3D spheroids generated using a hanging-drop system. Spheroids were treated with BKM120, LEE011, a combination of both or DMSO for 72h after spheroid formation and cell viability was measured using cell viability assay. Shown is the relative cell viability normalized to the initial measurement and the DMSO control. Data shows the mean ±SD from primary cells of 9 MEN1 +/- and 5 MEN1 +/+ mice with 4-14 technical replicates each (depending on total amount of cells). 1way ANOVA. ns, not significant; *, p< 0.05; **, p< 0.01; ***, p<0.001; ****, p< 0.0001

3.2.8 Insulin secretion of Men1 primary spheroids after treatment

Insulin secretion upon glucose stimulation is one of the most important physiological features of the pancreatic islets, a function that is carried out by the insulin-producing beta cells. We set out to investigate whether the treatment with BKM120 and LEE011 affects the ability of islets cells to produce insulin. In view of a possible use of these drugs for treatment of pNET patients, it is important to know whether these drugs would perturb insulin secretion or not. We used 3D spheroids of the isolated Men1 mouse islets and treated them with BKM120 and LEE011 in the same way as for the cell viability assays. After 72h of treatment, spheroids were starved before measuring baseline insulin secretion (incubation with 2.8mM glucose) and secretion upon stimulation with high glucose (16.5mM glucose).

Figure 44 shows the insulin secretion of both wild-type and *Men1*- deficient spheroids. In the wild-type spheroids used as controls, a low baseline insulin secretion can be seen that is significantly increased upon glucose stimulation. The treatment with BKM120 and LEE011 alone or in combination showed no differences in insulin secretion.

Men1- deficient spheroids showed a higher baseline insulin secretion compared to the wild-type spheroids. Additionally, treatment with BKM120 alone increased the baseline insulin secretion even more. In the control *Men1*- deficient spheroids we could not see an effect of the glucose stimulation. Both baseline insulin levels and glucose-stimulated insulin levels were similar. Also, in the *Men1*- deficient spheroids treated with the drugs, no significant effect of the glucose stimulation could be measured. These results indicate a disturbed insulin secretion behavior in the heterozygous animals, most likely due to the tumors in the islets. As the drugs showed no effect on the wild-type islets, it still can be concluded that they do not interfere with the insulin secretion of islets.

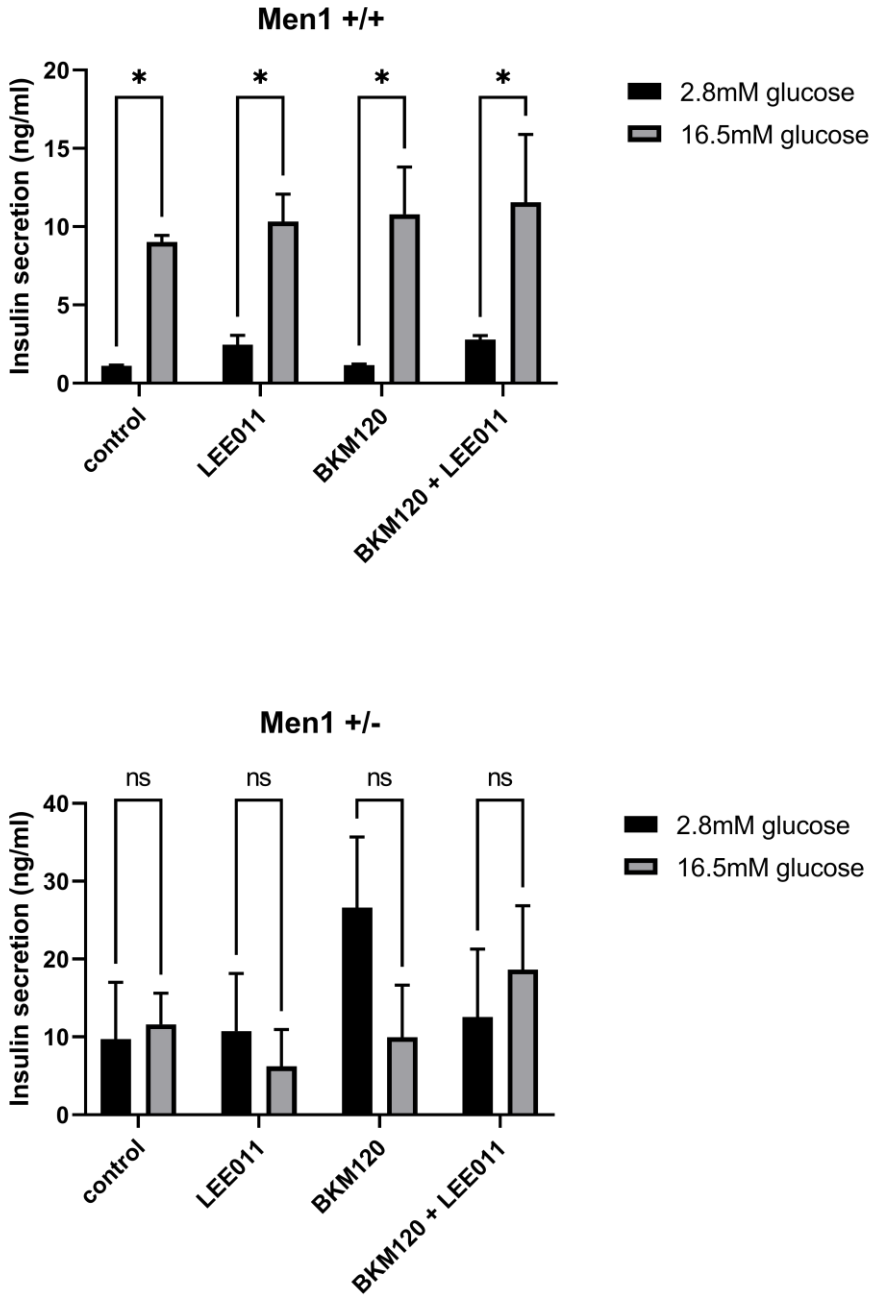

Figure 44: Glucose stimulated insulin secretion in Men1 primary spheroids
Primary islets were isolated from *Men1* heterozygous (wt/mut) and wild-type (wt/wt) mice. Single cells were obtained out of the islets and 3D spheroids generated using a hanging-drop system. Spheroids were treated with BKM120, LEE011, a combination of both or DMSO for 72h after spheroid formation. After starvation, baseline insulin secretion (incubation with 2.8mM glucose) and secretion upon stimulation with high glucose (16.5mM glucose) was measured by incubating the spheroids with the mentioned concentrations of glucose and collecting the supernatant after incubation of 1h. Insulin levels were measured using an insulin-ELISA kit. Data shows the mean ±SD from primary cells of 3 *Men1* +/- and 3 *Men1* +/+ mice with 3 technical replicates each. 1way ANOVA. ns, not significant; *, p< 0.05; **, p< 0.01; ***, p<0.001; ****, p< 0.0001

3.2.9 Summary

This study is the first of its kind to use a PI3K/AKT and a CDK4/6 inhibitor for the treatment of pNETs. Our unique approach of combining these two inhibitors showed good results in our *in vitro* studies using cell lines and primary cells. In detail, we showed downregulation of 2D cell proliferation, 3D cell viability and 3D spheroid growth in INS-1E and NT3 cells with the combination of BKM120 and LEE011 giving superior results than the single drugs. Additionally, treating the cells with BKM120 alone or in combination with LEE011 induced apoptosis in the cell lines. In line with this, also primary cells from *Men1* heterozygous mice showed a reduction of cell viability upon drug treatment, whereas cells from wild-type mice only showed a not significant trend. Again, the combination of BKM120 and LEE011 reduced cell viability significantly better in the primary cells compared to the single drugs. Lastly, we could show that our treatment does not affect insulin secretion in Men1 mouse islets, even though the baseline secretion in tumor-bearing mice is already altered compared to wild-types.

3.3 Characterization of PCCs and PGLs occurring in MENX heterozygous animals

As described before, the MENX rat model is well suited for the study of NETs. Hyperplasia and/or tumors develop in the adrenals, pituitary, thyroid and pancreas. Besides the homozygous animals, which develop hyperplasia from an early age on and die with 8-10 months of age because of tumor progression, also heterozygous animals develop the above-mentioned tumors. Development is slower in heterozygous animals, with tumors arising at 13-15 months of age. Overall, heterozygous rats live up to 20 months. As tumor progression in these animals is slower, it also allows for the development and growth of PGLs, a tumor that is rarely detected in the homozygous animals due to their early death. PGLs developing in the heterozygous animals give the unique opportunity to study similarities and differences between PCCs and PGLs in the same rats.

Our aim was to compare the molecular signature of matched PCCs and PGLs in the MENX model and ultimately compare them with human expression profiles. For this study, we used matched PGLs and PCCs occurring in eight MENX rats.

3.3.1 Sample preparation and quality control

After isolation of RNA from the adrenals and PGLs using laser microdissection, we performed Gene Array analysis to investigate the differences between the two tumor types. Table 17 shows the samples used. As shown in Figure 45, sample Pheo_F_3 was excluded after QA analysis as an outlier. PCA analysis grouped PCCs into one cluster and PGLs into two different clusters. Previously performed array data from WT animals was used as control [141]. Overall, strong significant gene expression differences between tumor tissues and wild-types as well as between PCCs and PGLs could be observed, as shown in Table 18.

Table 17: Sample overview for gene array study

label	No	Array name	Section	Tissue	Gender	Age (mo)	Genotype	Rat line
NN1	N1	Pheo_M_1	16/2193	pheochromocytoma	M	17.0	wt/mut	MENX rats
NN2	N2	Pheo_M_2	17/304	pheochromocytoma	M	18.0	wt/mut	MENX rats
NN3	N3	Pheo_F_3	17/35	pheochromocytoma	F	18.5	wt/mut	MENX rats
NN4	N4	Pheo_M_4	16/1968	pheochromocytoma	M	18.5	wt/mut	MENX rats
NN5	N5	Pheo_F_5	17/604	pheochromocytoma	F	18.5	wt/mut	MENX rats
NN6	N6	Pheo_F_6	17/193	pheochromocytoma	F	20.0	wt/mut	MENX rats
NN7	N7	Pheo_M_7	17/1092	pheochromocytoma	M	20.0	wt/mut	MENX rats
NN8	N8	Pheo_F_8	11/1538	pheochromocytoma	F	23.0	wt/mut	MENX rats
P1	P1	Para_M_1	16/2193	paraganglioma	M	17.0	wt/mut	MENX rats
P2	P2	Para_M_2	17/304	paraganglioma	M	18.0	wt/mut	MENX rats
P3	P3	Para_F_3	17/35	paraganglioma	F	18.5	wt/mut	MENX rats
P4	P4	Para_M_4	16/1968	paraganglioma	M	18.5	wt/mut	MENX rats
P5	P5	Para_F_5	17/604	paraganglioma	F	18.5	wt/mut	MENX rats
P6	P6	Para_F_6	17/193	paraganglioma	F	20.0	wt/mut	MENX rats
P7	P7	Para_M_7	17/1092	paraganglioma	M	20.0	wt/mut	MENX rats
P8	P8	Para_F_8	11/1538	paraganglioma	F	23.0	wt/mut	MENX rats

A

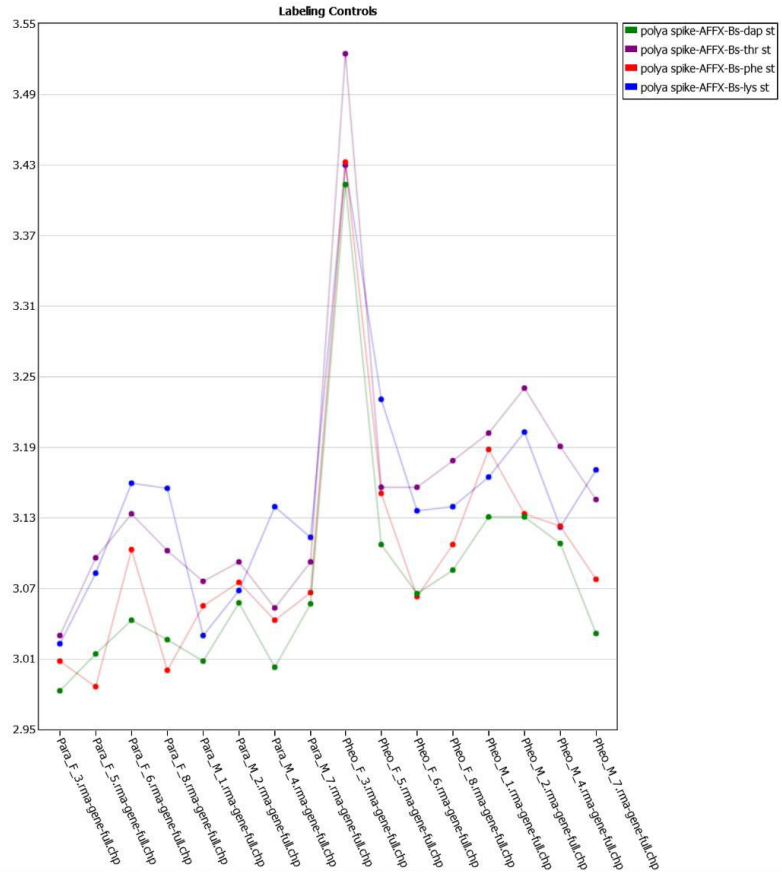

B

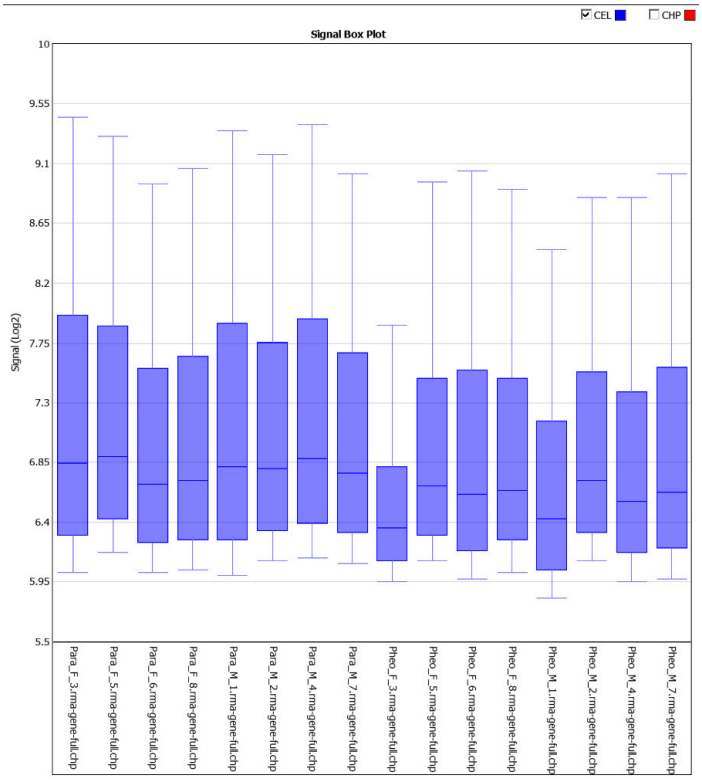

Figure 45: Quality analysis of samples used for gene array
Quality control of samples used for gene arrays was performed. Shown are the labeling controls (A) and the signal controls (B). Sample Pheo_F_3 was identified as outlier and excluded from further studies.

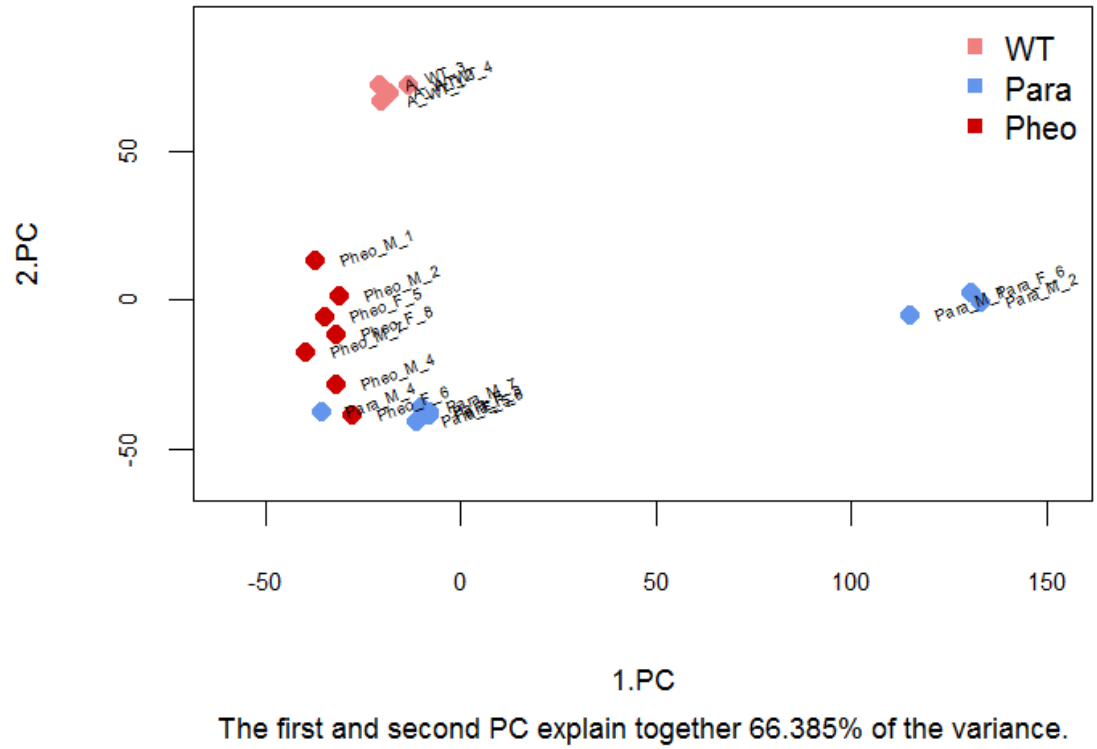

Figure 46: PCA of array samples
Principal component analysis showing the clustering of samples in the MENX array data. Shown are the two tumor types PCCs (Pheo, red) and PGLs (Para, blue) as well as wild-type adrenal samples (WT, pink).

Table 18: Statistical analysis of differently regulated genes in MENX arrays
Analysis was done with limma t-test and Benjamimin-Hochberg multiple testing correction

Statistical analysis /No of regulated genes	p<0.05	p<0.01	FDR<10%	p<0.05, Av>16	p<0.01, Av>16	FDR<10, Av>16%	FC>1.5x, p<0.05, Av>16	FC>1.5x, p<0.01, Av>16	FC>1.5x, FDR<10%, Av>16	FC>2x, p<0.05, Av>16	FC>2x, p<0.01, Av>16	FC>2x, FDR<10%, Av>16
Stat. analysis, Pheo vs WT	8824	5445	7200	7368	4922	6238	3954	3332	3734	1669	1501	1600
Stat. analysis, Para vs WT	8750	5479	7233	7934	5222	6720	4924	4051	4593	2293	2029	2202
Stat. analysis, Pheo vs Para	4456	1858	1182	3909	1760	1148	1470	957	728	522	369	309
Pheo-specific												68
Para-specific												293

Because we could observe two different groups in the PCA analysis for the PGLs, we set out to verify that all samples were indeed PGLs and not tissue that was wrongly classified as PGL. Thus, we analyzed the expression of TH (tyrosine hydroxylase), an enzyme that is involved in dopamine production and is highly expressed in chromaffin cells of adrenals but also para-sympatic ganglia and not in other organs of the body (Figure 47). As shown in Figure 48, all 16

samples and therefore all PGL samples showed a high expression of TH with CT values between 16 and 24. This suggests that all samples were correctly classified as PPGLs and that the differences in the PCA analysis are due to other reasons, e.g. stage of tumor progression or the procedure during tissue collection. Interestingly, the PGL samples showed a higher TH expression than the PCCs, indicating a higher expression of this gene in the former.

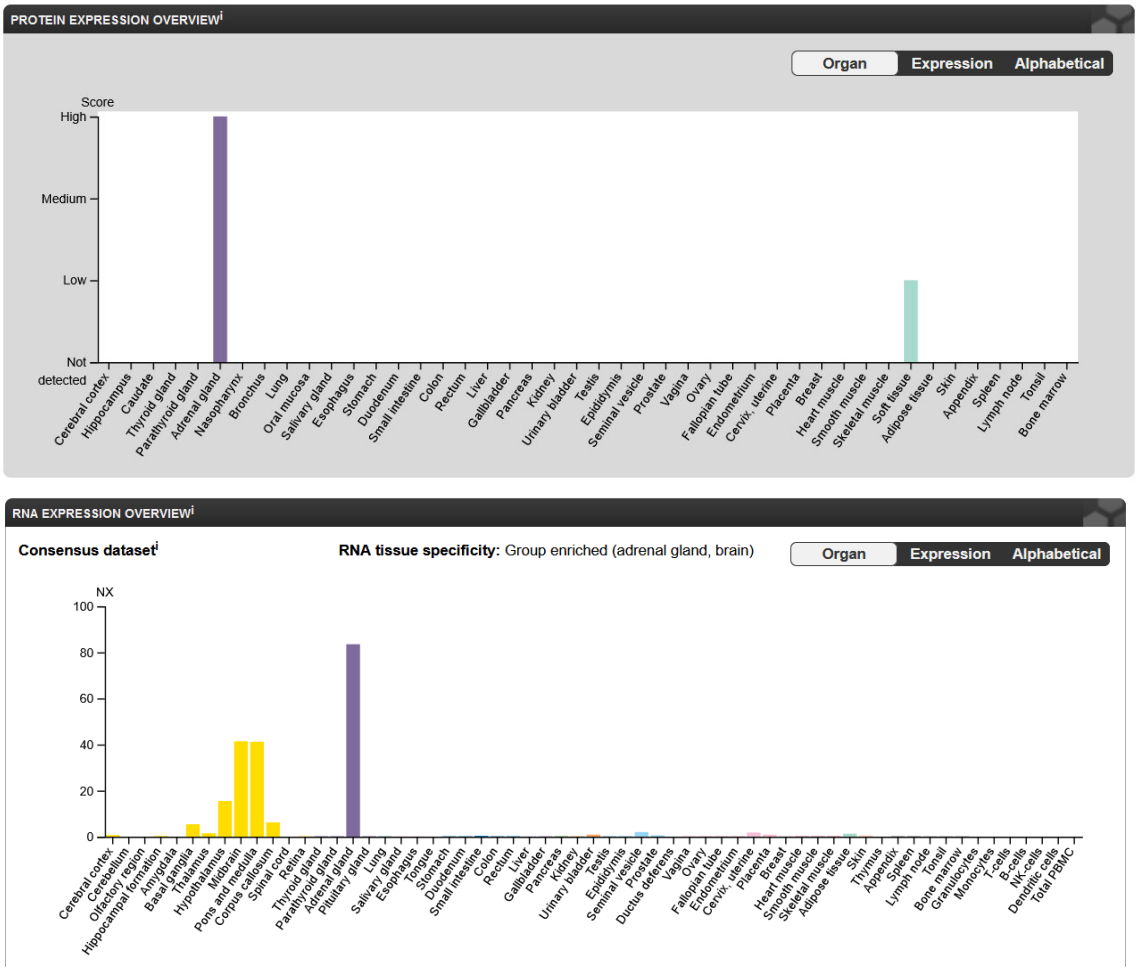

Figure 47: TH expression on protein and RNA levels
Shown are the TH expression on protein (A) and RNA (B) level according to the Human Protein Atlas. High expression is mainly observed in the adrenal glands. Data is obtained from the Human Protein Atlas as published in Uhlen M et al., A pathology atlas of the human cancer transcriptome. Science. (2017). Link: https://www.proteinatlas.org/ENSG00000180176-TH/tissue

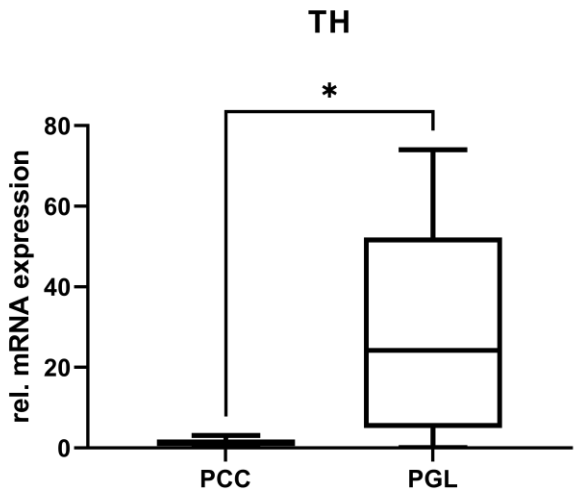

Sample	Ct
PCC 1	23,34
PCC 2	21,92
PCC 3	21,80
PCC 4	22,91
PCC 5	20,61
PCC 6	22,38
PCC 7	21,02
PCC 8	24,05
PGL 1	25,39
PGL 2	19,13
PGL 3	16,04
PGL 4	20,37
PGL 5	17,74
PGL 6	16,91
PGL 7	16,44
PGL 8	17,58

Figure 48: Expression of TH in PCC and PGL samples
Shown is the rel. mRNA expression of TH in all 16 PCC and PGL samples that were initially used for the study. TH expression was analyzed by qPCR using TaqMan probes. Additionally, the CT values for each sample are shown. Data shows the min to max box plot. Unpaired t-test. *, $p < 0.05$

3.3.2 Comparison of PCCs and PGLs in MENX rats

We could observe that both rat PCCs and PGLs had a significant number of differentially expresses genes when compared to wild-type controls. Additionally, our analysis also showed a high number of altered genes when we compared PCCs with PGLs. To investigate the differences between the two tumors, we set out to compare the genes that were differentially regulated in PCCs vs. wt with those in PGLs vs. wt. This analysis revealed that 68 genes are differently regulated in PCCs but not in PGLs and that 293 genes are differentially regulated in PGLs but not in PCCs (Figure 49). This gave a total number of 361 differentially expressed genes in PCCs vs. PGLs compared to 3802 genes that were differentially regulated when both PCCs and PGLs were compared to wild-types.

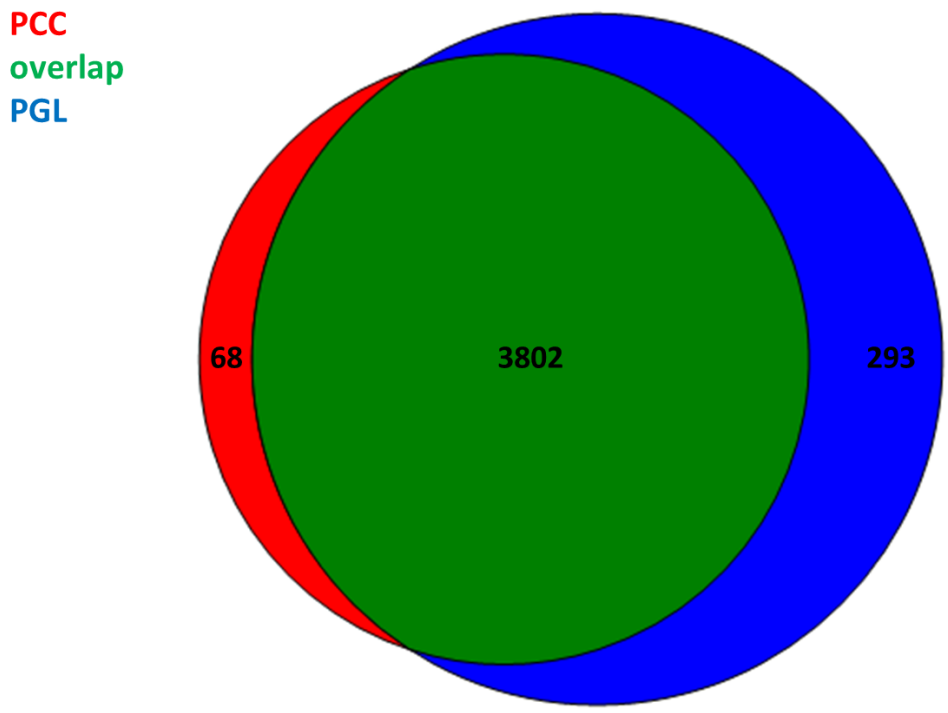

Figure 49: Analysis of MENX array data
Shown are the numbers of differently regulated genes in the MENX array data as Venn-Diagram. Differently regulated genes were determined by their expression levels compared to the wt samples. Red indicates the PCC specific genes, blue the PGL specific genes and green the commonly dysregulated genes in both PCCs and PGLs. To determine the specific genes, we positively selected genes with FC>2, FDR<0.1, Av>16. Then, genes with p<0.05 in the other tissue vs. WT were removed. Then, all genes with FC>=1.5x in the other tissue were removed. Then, only genes with FC>1.5, p<0.05, Av>16 in the PCC vs PGL comparison were kept.

We continued our approach by analyzing the genes that were PCC specific (68 genes) or PGL specific (293 genes). Our analysis revealed that these genes were involved in processes regulating extracellular matrix processes and oxygen levels (Figure 50), indicating an involvement and a different regulation of processes that are associated with ECM and oxygen saturation. Analyzing the genes involved in GOBP pathways as shown in Figure 50 revealed that genes associated with aggressiveness and invasion are upregulated in PGLs compared to PCCs. A more detailed analysis for some of these genes was done in the next section, and is indicated in Table 19.

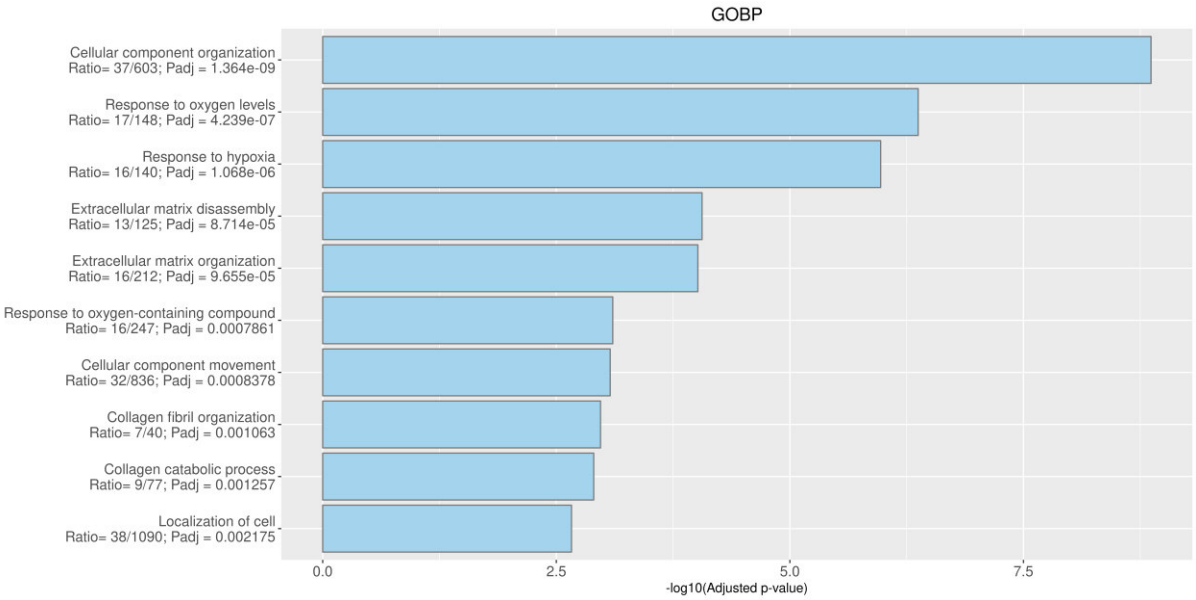

Figure 50: GOBP analysis of PCC vs PGL MENX data
Shown are are the GO Biological Processes of the 361 differently regulated genes in PCCs vs PGLs. Genes were analyzed using CANCERTOOL, an open access tool for analyzing cancer datasets. Shown are the 10 most significantly involved GOBPs in the differently regulated genes. CANCERTOOL: a visualization and representation interface to exploit cancer datasets. Cortazar AR, et al. Cancer Res. 2018 Sep 19. pii: canres.1669.2018.

3.3.3 Comparison of MENX data with human data

To increase the clinical relevance of our data, we set out to compare our MENX data with public available human data. Our aim was to find commonly dysregulated genes and pathways in the MENX and a human dataset. We used a publicly available human dataset (GSE19422), which contains transcriptional analysis data of 84 primary PCC and PGLtumors. Specifically, 61 tumors are PCCs, 23 PGLs and 6 normal adrenal tissues are included as controls. We first analyzed the dataset in the same way as our rat data (first tumors vs. control and then PCC vs. PGL). After this, we compared the differentially regulated genes in PCCs vs. PGLs from our rats with the ones from the human dataset. By doing this, we ended up with an overlap of 359 and 439 commonly dysregulated genes in PCCs and PGLs, respectively (Figure 51). Additionally, 52 genes were commonly dysregulated in PCC vs. PGL in both species.

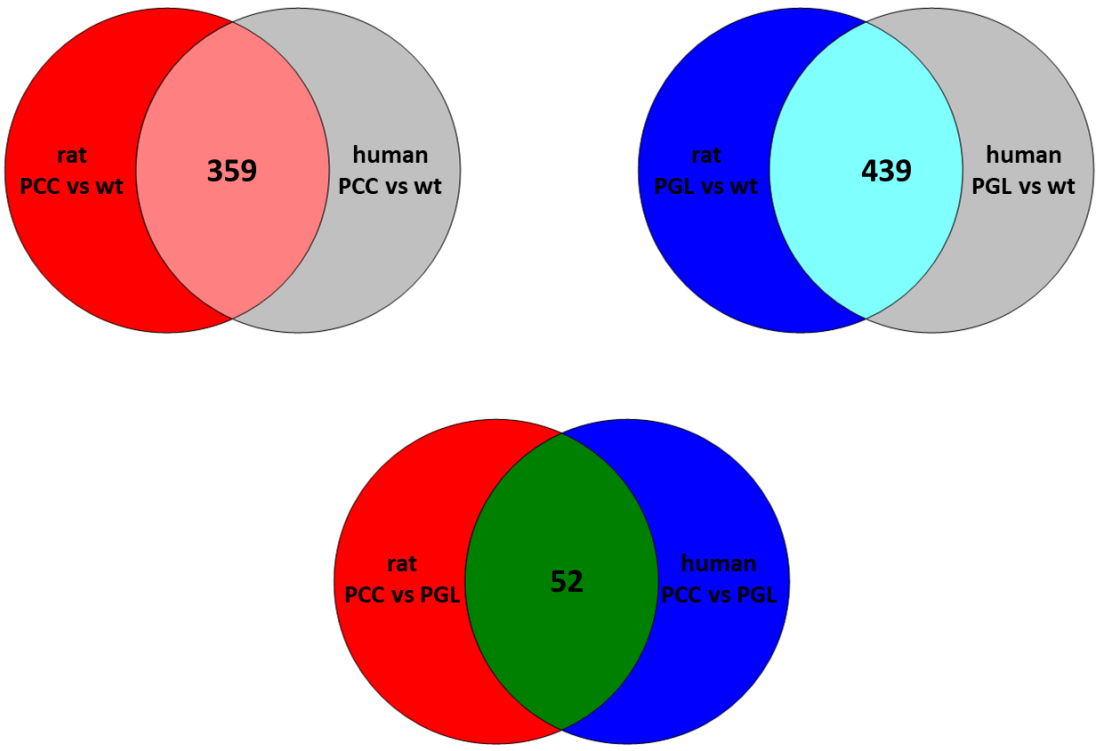

Figure 51: Comparison of human and rat data
Shown are the numbers of differently regulated genes in the tumors of rat and human data as Venn-Diagrams. A shows the differently regulated genes of PCC versus normal tissue of both species and their overlap, whereas B shows the same data for PGLs. C shows the differently regulated genes in PCC vs PGL of both species as well as the overlap between the species. Differently regulated genes of the rat data were obtained as described in Figure 49. Human data was obtained from dataset GSE19422. GSE19422 data was from Agilent arrays and contained normalized log2 ratios (Cy5/Cy3) representing test/reference. Significantly regulated genes (FC>2, FDR<0.1, Av>0.1 were matched to the MENX rat data based on gene symbols. If there were several ratios for a certain gene, only the one with the highest fold-change was used.

Then we annotated the 52 commonly dysregulated genes of PCC vs. PGL in both datasets as shown in Figure 52. Again, we could see a strong involvement of pathways regulating ECM processes and angiogenesis. In detail, commonly dysregulated genes were associated with blood vessel development, cardiovascular system development and aorta morphogenesis as well as with collagen catabolic processes, extracellular matrix disassembly, collagen fibril organization and cell morphogenesis. To gain further insight into the functions of the genes, we had a closer look at their role in the above-mentioned processes and in which tumor type they are at higher or lower levels. The details, as showed in Table 19, revealed that genes promoting angiogenic processes were upregulated in PGLs compared to PCCs. Additionally, genes involved in cell movement, reorganization of ECM and in promoting migration were also upregulated in PGLs.

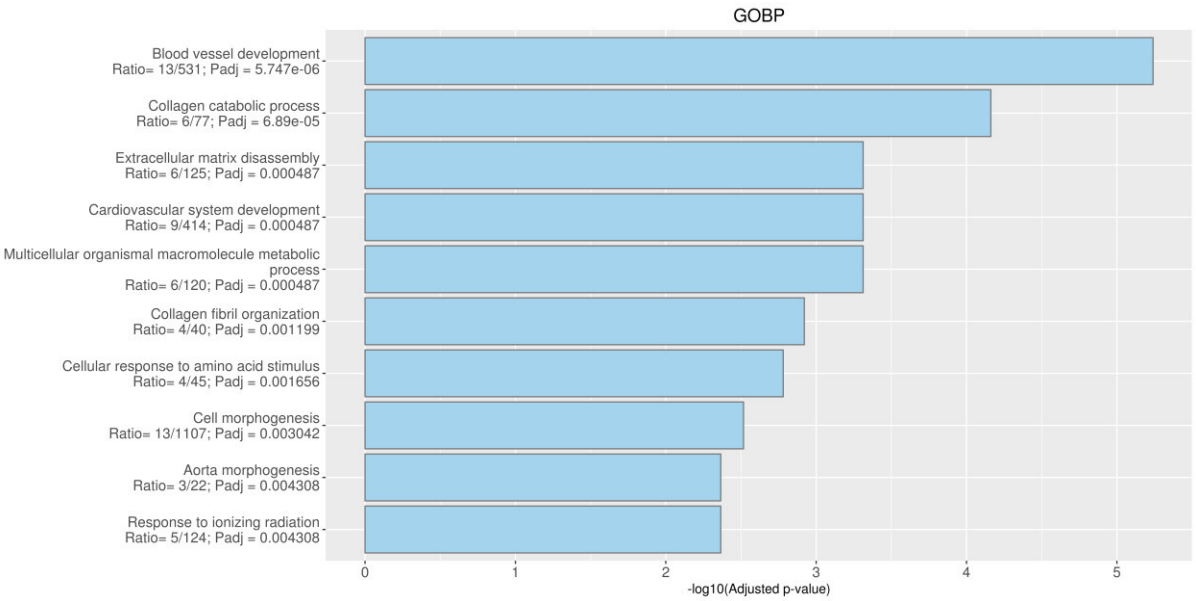

Figure 52: GOBP analysis of commonly dysregulated genes in humans and rats
Shown are the GO Biological Processes of the 52 differently regulated genes in PCCs vs. PGLs of humans and rats. Genes were analyzed using CANCERTOOL, an open-access tool for analyzing cancer datasets. Shown are the 10 most significantly involved GOBPs in the differentially regulated genes. CANCERTOOL: a visualization and representation interface to exploit cancer datasets. Cortazar AR, et al. Cancer Res. 2018 Sep 19. pii: canres.1669.2018.

Table 19: Detailed gene information of pathways shown in Figure 52
Table with the 52 single genes differentially regulated in PCCs vs. PGLs, the corresponding protein function and in which tumor type they are upregulated based on the PCC vs. PGL comparison of the rat arrays. Genes involved in blood vessel development, collagen catabolic process, extracellular matric disassembly, cardiovascular system development, collagen fibril organization and cell and aorta morphogenesis as described in Figure 52 are written in bold.

Gene	Protein function	PCC vs. PGL: upregulated in
Star	cholesterol transport protein in mitochondria	PCC
Kcnmb2	potassium channel subunit	PCC
Tfap2b	transcription factor that stimulates cell proliferation	PCC
Slc6a2	norepinephrine transporter	PCC
Mrap	melanocortin receptors	PCC
Dbh	Dopamine beta-hydroxylase	PCC
Slc31a1	copper uptake protein	PCC
Plcxd3	Phospholipases	PCC
Cryba2	Crystallin	PCC
Lpcat2	acyltransferase	PCC
Scn3a	Voltage-gated sodium channels	PCC
Eya1	phosphatase and as transcriptional coactivator for SIX1, plays an important role in hypaxial muscle development	PCC
Ldlr	lipoprotein receptor	PCC
Camk2b	role in the reorganization of the actin cytoskeleton	PCC
Tln2	links integrin to the actin cytoskeleton, may play an important role in cell adhesion	PCC
Gramd1b	Cholesterol transporter	PCC
Arhgap22	regulates endothelial cell capillary tube formation	PCC
Ica1	plays a role in neurotransmitter secretion	PCC
Coro2a	involved in actin filament binding, cell cycle progression and spoptosis	PCC
C1qtnf5	member of the C1q / TNF superfamily, involved in cell adhesion	PGL

Col15a1	collagen, connects tissues, inhibits angiogenesis	PGL
Marcks	involved in cell shape, cell motility and cell cycle progression	PGL
Fam129a	involved in the endoplasmic reticulum stress response	PGL
Gas7	involved in actin filament binding and polymerization	PGL
Tubb6	major constituent of microtubules	PGL
Pls3	Actin-bundling protein	PGL
Dmp1	Extracellular matric and calcium ion binding	PGL
Ifitm3	IFN-induced antiviral protein	PGL
Jag1	Ligand for multiple Notch receptors	PGL
Vim	ntermediate filament	PGL
Gsn	actin-modulating protein, preventing monomer exchange	PGL
S100a4	Increases cell motility and invasiveness, also involved in angio-genesis	PGL
Col5a2	minor connective tissue component	PGL
Rnase4	RNase	PGL
Col4a1	integral components of basement membranes	PGL
Fstl1	promotes migration, involved in angiogenesis	PGL
Lama4	mediates the attachment, migration and organization of cells into tissues	PGL
Mmp14	degrades various components of the extracellular matrix such as collagen	PGL
Bcl11b	regulator of T-lymphocytes	PGL
Igfbp4	IGF-binding protein	PGL
Cryab	Alpha-crystallin	PGL
Nox4	NADPH oxidase, oxygen sensor	PGL
Olfml2b	Olfactomedin-like protein	PGL
Col6a1	Collagen, ECM component	PGL
Col6a3	Collagen, ECM component	PGL
Loxl2	promotes epithelial to mesenchymal transition and angiogen-esis	PGL
Prrx1	transcriptional regulator of muscle creatine kinase	PGL

Cxcl12	positive regulator of monocyte migration and a negative regulator of monocyte adhesion	PGL
Fbln2	component of connective tissue microfibrils	PGL
Col3a1	Collagen, ECM component	PGL
Sfrp2	modulators of Wnt signaling	PGL
Postn	Induces cell attachment and spreading	PGL

3.3.4 Validation of array data

To validate our findings that were based on the array data, we selected dysregulated genes in PCCs vs. PGLs according to our array analysis as mentioned above and validated them by qRT-PCR. To this end, we selected a total number of 10 genes, namely Col6a1, Jag1, Eya1, Ang, Lama4. Loxl2, Ltbp2, Col3a1, Mmp14 and Cxcl12. Figure 53 shows the expression of these genes by qPCR. In total, we used 8 PGL and 8 PCC samples from the MENX rats. Except for Eya1, where we could only see a trend, all the genes showed a significant difference in expression between PCCs and PGLs that is in line with the array data.

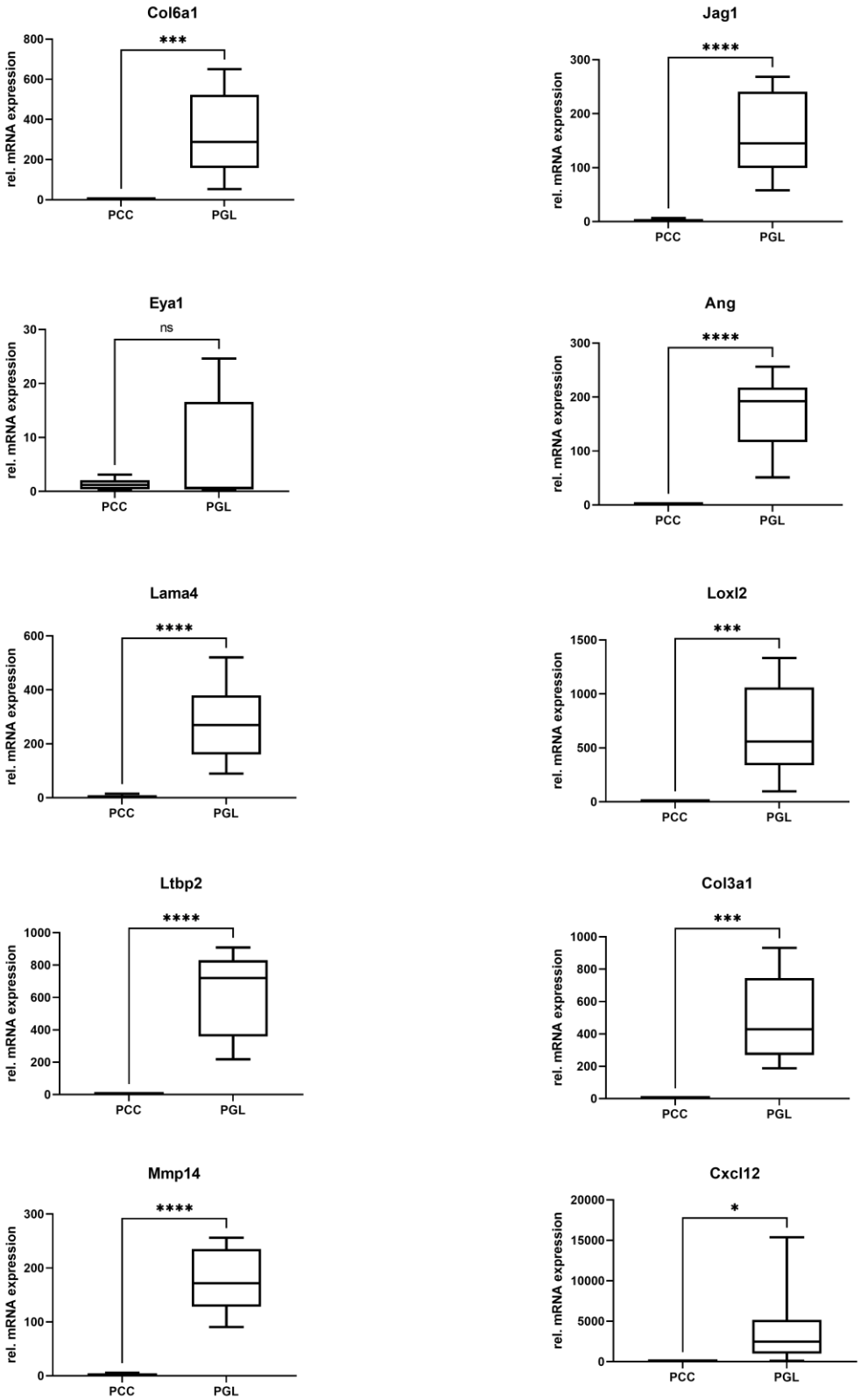

Figure 53: Validation of array data by qPCR

Shown are the relative expression levels of Col6a1, Jag1, Eya1, Ang, Lama4. Loxl2, Ltbp2, Col3a1, Mmp14 and Cxcl12 in rat PCCs (n=8) and PGLs (n=8). Data shows the min to max box plot. Unpaired t-test. ns, not significant; *, p< 0.05; **, p< 0.01; ***, p<0.001; ****, p< 0.0001

3.3.5 Summary

Our aim was to investigate the differences in PCCs and PGLs arising in our MENX rat model. Additionally, we wanted to compare this data with human data to investigate in the translational potential of our model. Our analysis revealed that, despite being of the same cell origin, PCCs and PGLs in the MENX rat model show differences in their gene expression. Especially processes involved in extracellular matrix shaping and response to oxygen levels were altered, indicating a more aggressive behavior of the PGLs. Comparison with the human data confirmed these findings and gives them further clinical relevance. Similar to the situation in human patients, the rat PGLs show a more aggressive phenotype than the PCCs. Processes are regulating extracellular membrane components, promoting epithelial-to-mesenchymal transition and angiogenesis. Our analysis shows the great potential of the MENX rat model, which can be used for future studies to further investigate the molecular characteristics of PGLs and PCCs and for future treatment studies.

4. Discussion

NETs are a heterogeneous group of tumors arising from various organs such as adrenals, pancreas, thyroid, pituitary and others [3, 4]. The focus of this thesis was on two specific types of NETs, namely PPGLs and pNETs, which arise from adrenal and extra-adrenal ganglia or pancreatic islets, respectively. On the one hand, we wanted to find novel therapies for these NETs based on their molecular characteristics, and, on the other hand, we wanted to investigate the biology of these tumors in greater detail.

Based on both preliminary studies done in our lab and extensive literature search, we found that the PI3K/AKT and the CDK4/6 pathways are dysregulated in PPGLs and pNETs. Therefore, we used a combination treatment strategy to target these two pathways, and found that it shows great anti-tumor potential in both PPGLs and pNETs. These results can potentially be translated into novel treatments for human patients.

The MENX rat model allowed us to investigate the biology of PGLs and PCCs and especially their common and specific molecular features, as these tumors can develop in the same animal. Our study showed that PGLs have a gene expression profile of more aggressive tumors when compared to PCCs in both rats and humans. The molecular characteristics presented in this thesis broaden the knowledge of the molecular pathogenesis of PPGLs, and are therefore of importance for future personalized molecular-based treatment strategies.

4.1 PI3K/AKT and CDK4/6 targeted therapy of PPGLs

The PI3K/AKT and the CDK4/6 pathways are two of the most important signaling pathways in cells and are responsible for many functions like cell cycle progression, proliferation and survival. Given their involvement in the above-mentioned processes, they are often dysregulated in cancer. This led to the development of specific inhibitors that target these pathways at various levels. Based on the high pAKT levels in PPGL cell lines, and on the involvement of p27 in PPGL tumorigenesis that we identified in preliminary studies, we hypothesized that the PI3K/AKT and the CDK4/6 pathways are dysregulated in PPGLs and could be possible therapeutic targets. To verify this hypothesis, we used BKM120, a PI3K/AKT inhibitor and LEE011, a CDK4/6 inhibitor. Our goal was not only to test the potential of these drugs as single agents, but also to combine them to investigate whether the combination would show any additional advantage. To combine different drugs for cancer treatment has become more and more frequent in the last years, as this approach showed to have a beneficial efficiency and can also bypass drug resistance in many cancer types [142]. Previous studies of our group and others have already shown that treatment of NET cells with PI3K/AKT or CDK4/6 inhibitors is effective. In detail, inhibition of the PI3K/mTOR pathway reduced proliferation and promoted apoptosis in PPGLs [129, 143, 144]. Studies have also shown the potential of CDK4/6 inhibition in NET cells, but not specifically in PPGLs [116, 119, 145].

To confirm our hypothesis, we first tested the effects of BKM120 and LEE011 as single agents on the proliferation in PPGL cell lines. Our results showed that the drugs significantly reduced proliferation of both PPGL cell lines (PC12 and MPC) using a standard 2D cell culture system. Interestingly, the combination of both drugs showed a superior effect, decreasing the proliferation even more. This can also be seen in the IC50 values that were generated for the drugs in both cell lines, as shown in Table 20 and this lead to the question if the superior effect we saw was of additive or synergistic nature. To answer this question, we calculated the Combination Index (CI) using the Chou-Talalay method, a well-established and widely used method that allows to evaluate the effect of combinatorial drug treatment [146-148]. The calculated CI value is used to determine whether between drugs there is Synergism (CI < 1), an Additive Effect (CI = 1) or Antagonism (CI > 1). As seen in Table 20, the CI for BKM120 and LEE011 in PC12 cells is 0.78, suggesting a clear synergistic effect. In contrast, in MPC cells, the CI value is 1.05, indicating an additive effect of the drugs. Looking at the IC50 values in the MPC cell

line, one can see that the BKM120 as single drug showed a much stronger effect than LEE011 alone. This suggests a lower sensitivity of the MPC cells for LEE011 that might also explain the additive but not synergistic effect of the combination.

Table 20: IC50 values and CI in PPGL cell lines
IC50 values of PC12 and MPC cells as shown in Figure 15 and Figure 16. The Combination Index (CI) was calculated based on the Chou-Talalay method using the formula CI = (IC50 BKM combination) / (IC50 BKM alone) + (IC50 LEE combination) / (IC50 LEE alone).

	IC50 [µM]				CI
	BKM120 alone	LEE011 alone	BKM120 combina-tion	LEE011 combination	
PC12	0,7473	1,604	0,2043	0,8172	0,7829
MPC	0,6268	3,678	0,3913	1,5652	1,0498

The ability of a drug to induce apoptosis is an important parameter in view of a possible implementation in clinical practice as it shows that tumor cells not only stop proliferating but also die upon treatment. Additional to a reduction in cell proliferation, we could also show that BKM120 alone and in combination with LEE011 induces apoptosis in both PC12 and MPC cells. In line with the results of cell proliferation, the combination of BKM120 and LEE011 induced significantly more apoptosis in the treated cells compared to BKM120 alone. As the CDK4/6 pathway is mainly involved in cell cycle regulation, we did not expect to see an increase in apoptosis upon LEE011 treatment [149, 150]. Also, the apoptosis induction by BKM120 was in line with our expectations, as the PI3K/AKT pathway is associated with apoptosis, and previous studies in other cell lines have shown apoptosis induction using BKM120 [151-154]. The most interesting finding is the significantly increased apoptosis in the combination group in both cell lines. This shows that LEE011 used as single drug does not have an apoptotic effect, but it has one when used in combination with BKM120. Therefore, we could also see a synergistic effect of apoptosis induction in the PPGL cell lines when using both drugs.

Next, we investigated the potential of PC12 and MPC cells to invade and migrate and whether our treatment approach would affect these processes. We could show that PC12, but not MPC cells, do migrate and invade. This suggests that PC12 cells display a more aggressive pheno-

type than MPC cells. PPGLs can be grouped into different clusters depending on their mutation status and molecular profile, as explained in section 1.2.2. Amongst the different clusters, the pseudohypoxic cluster 1 is associated with a more aggressive tumor behavior than cluster 2 [21, 155]. Indeed, MPC cells are a cell line model of cluster 2 due to their Nf1 mutation status and the lack of Hif2α, while PC12 cells have expression of the cluster 1 marker Hif2α [156-158]. These different molecular features of PC12 and MPC cells might explain their different migration and invasion potential.

Interestingly, treatment of PC12 cells with BKM120, LEE011 or a combination of both decreased both migration and invasion. In detail, all three treatments significantly reduced migration compared to the controls. While both BKM120 and the drug combination reduced migration more efficiently than LEE011, there was no difference between BKM120 alone or in combination with LEE011. This is most likely due to the fact that BKM120 alone already reduced migration to a minimum so that no additional beneficial effects of the combination could be seen. A reduction of the BKM120 dose might give different results and could show a beneficial combinatorial effect. In contrast to the reduction of migration, LEE011 did not significantly inhibit the invasion of PC12 cells even though we could observe a positive trend. Both BKM120 and the combination decreased invasion significantly compared to the controls. Additionally, the combination showed a beneficial effect, suppressing invasion significantly more than the two single drugs. This shows that the same doses of the drugs had different effects on migration and invasion, and that for complete inhibition of invasion, higher doses or the combination of both drugs are needed.

Proliferation, migration and invasion are well-known oncogenic features of tumor cells and belong to the so-called hallmarks of cancer [159, 160]. The hallmarks of cancer were initially introduced by Hanahan and Weinberg in 2000 and were updated by the same authors in 2011. The hallmarks of cancer are “distinctive and complementary capabilities that enable tumor growth and metastatic dissemination” [159] and represent important therapy target points. We could show that our treatment approach is highly effective and has an impact on the above-mentioned hallmarks.

The effects described so far were all generated using traditional 2D monolayer cell culture systems. 3D cell culture represents a more *in vivo*-like situation as cells grow in a three-dimensional structure and can more closely interact with each other. We could demonstrate that the treatment with BKM120 and LEE011 is also highly effective in 3D cell cultures of PC12

and MPC cells. Similar to the situation in 2D cultures, the combination of BKM120 and LEE011 reduced PC12 and MPC cells viability more effectively than the single drugs, proving the great potential of this drug combination. The concentrations that were used for the 3D cell culture were considerably higher compared to those used for the 2D monolayers. A higher resistance of cells growing in 3D spheroids is a well-known effect that was already observed before by us and others [161-166].

Initially, for both 2D and 3D cell cultures we investigated the effect of the drugs within the first three days post treatment. Then, we set out to determine the long-term effects of our drug treatments by measuring the 3D spheroid growth in PC12 and MPC cells longitudinally over the course of 14 days. Our results showed that in both cell lines the administration of LEE011, BKM120 and their combination reduced spheroid growth over time. In PC12 cells, BKM120 and the combination showed an effect from the start of the treatment and inhibited spheroid growth throughout the 14 days of treatment. In contrast, LEE011 only showed an effect from Day 7 onwards. A slightly different pattern was observed in the MPC cells, as both drugs caused a clear growth inhibition from the beginning of the treatment. Consequently, tumor growth was completely suppressed by the combination treatment.

We also tested the potential of PC12 and MPC cells to invade in a 3D system. Spheroids are embedded in Matrigel, and cells with invading potential can be seen penetrating through this matrix. Our experiments showed that PC12, but not MPC, cells were able to invade using the 3D system. These results are in line with the 2D experiments, where only PC12 cells showed the potential to invade. Treatment of PC12 cells with LEE011, BKM120, or the combination of both drugs significantly reduced the invasion compared to the controls. The inhibition of invasion was already very strong upon treatment with the single drugs, and no difference between the treatment with BKM120 alone or the combination could be seen. A reduction of the concentrations might give different results and would allow a better comparison of the treatment groups.

Comparing the results of 2D and 3D cell culture, it can be concluded that the results of the traditional 2D cell culture could be mostly confirmed in the 3D system. As mentioned, the concentrations of drugs used are higher in the 3D cell culture, as cells are more exposed to the drugs in a 2D monolayer compared to the dense spheroid structure. Besides the different concentrations, the overall effects on cell vitality and invasion are similar. In both systems, the combination of BKM120 and LEE011 showed superior effects compared to the single drug

treatments. Interestingly, for LEE011 there seem to be differences between the 2D and 3D cell culture and between the two cell lines. Based on the 2D data, LEE011 was more effective in PC12 than MPC cells with IC50 values of 1.6µM and 3.7µM in PC12 and MPC cells, respectively. The 3D cell growth data shows a different pattern as in PC12 cells LEE011 did not affect spheroid growth within the first days of treatment, while in MPC cells it inhibited spheroids growth starting from the beginning. MPC cells were generated from a PCC developing in a *Nf1*-heterozygous mouse as an alternative to the only available PCC cell line back then, i.e. PC12 cells [157, 167]. *Nf1* encodes a ras-GTPase-activating protein, and therefore the Ras signal transduction pathway is disturbed in MPC cells. Ras is an important member of the Ras/Raf/MEK/ERK signal transduction pathway that transmits signals upon various stimulations, ultimately leading to cell proliferation and prevention of apoptosis [168]. Additionally, the Ras/Raf/MEK/ERK signal transduction system is also part of the PI3K-AKT pathway [169]. Therefore, Ras plays a role both in the CDK4/6 pathway as it regulates cell proliferation as well as in the PI3K pathway. The disruption of the Ras signaling cascade in MPC cells could explain the different sensitivity of MPC and PC12 cells towards LEE011. However, it does not explain the differences seen between 2D and 3D. The different cell architecture and altered secretion of extracellular membrane factors in the 3D cell culture could lead to the higher sensitivity of MPC cells in the 3D spheroid system. As 3D cultures are closer to an *in vivo* situation, their value in terms of predicting drug effectiveness at the organism level is higher. Therefore, we can conclude that also the treatment with LEE011 is effective in MPC cells.

Altogether, we can conclude that our combinatorial treatment strategy proved to be efficient in 2D and 3D cell cultures. Given that 3D cultures were shown to have higher predictive value than 2D cultures in therapy studies, the efficacy of our combination may therefore extend to *in vivo* systems.

Additionally to the cell lines, we also tested our treatment strategy in primary PPGL cells from MENX rats or from human patients. As a result of a frameshift mutation in p27, MENX rats develop multiple NETs, including PCCs with full penetrance. After isolation of primary cells from the adrenal tumors, we generated 3D spheroids and treated them with LEE011, BKM120 or their combination. Assessment of cell viability showed that all treatments were efficient and reduced cell viability. While LEE011 gave the weakest effect but still reduced cell viability significantly compared to the controls, the combination of BKM120 and LEE011 showed the best effect and reduced cell viability more strongly than each single drug treatment. Similar

to the cell lines, we also saw induction of apoptosis in rat primary PCC cells treated with BKM120 or with the drug combination. This confirms that apoptosis can also be induced in primary 3D cells. We could recently show that PCCs occurring in MENX rats show a pseudo-hypoxic signature and belong to the PPGL cluster 1 [170]. The beneficial effect of the combination seen in primary MENX PCC cells suggests that our therapeutic strategy is well-suited for treatment of cluster 1 cases.

To complete our *in vitro* studies, we treated primary cells generated from freshly resected human PPGL tissues. These primary human cultures confirmed the findings obtained with both cell lines and primary rat cells. The treatments reduced the viability of the human PPGL cells, with BKM120 and the combination giving the best results. It has to be noted that there was a trend towards more reduction of cell viability in the samples treated with the combination compared to BKM120 alone, which was, however, not significant. This is most likely due to the low number of samples we could test. PPGLs are rare tumors and the number of patients being operated in Munich each year is low. As slow-freezing does not work for these tumors, tissues cannot be collected elsewhere and then shipped to the laboratory, only fresh tissues work for primary cell isolation. This greatly limits the tissue procurement from distant collaboration partners. The possibility to increase the number of patients in the future may strengthen our findings, and could enhance the trend towards a greater reduction of cell viability in the combination treatment. Unfortunately, clinical data of the patients used in this study were not available. PPGLs can be grouped into different clusters according to their mutation status, gene expression and catecholamine secretion, and a treatment in order to be effective should consider these parameters [32]. Further knowledge of the patients' mutation status would help us evaluate whether our treatment strategy can be used for patients belonging to multiple clusters or is most effective for one specific cluster.

Based on the strong effects of the selected drugs seen *in vitro* using different experimental models, we set out to evaluate our drug treatment approach *in vivo*. To this end, we engrafted PC12 cells subcutaneously in immunodeficient mice to form tumors. After tumor formation, we divided the mice into five different groups and treated them as follows: 1. Vehicle control; 2. LEE011 75mg/kg; 3. BKM120 25mg/kg; 4. BKM120 25mg/kg + LEE011 75mg/kg; 5. BKM120 12.5mg/kg + LEE011 25mg/kg. Using two different concentrations of the drugs in the combination groups allowed us to better evaluate whether the potential benefits of the combination treatment could be maintained when reducing doses and the associated side effects.

Tumor size was measured routinely during three weeks of treatment and at the end of the study, we collected the engrafted tumors for further analysis. Our results showed that BKM120 as a single drug and both combination groups reduced the tumor volume significantly when compared to the vehicle controls. Treatment with LEE011 only showed a trend towards tumor volume reduction, which was, however, not significant. Treatment with the "higher dose" drug combination was more effective at reducing the tumor volume. Interestingly, the "lower dose" combination treatment showed a significantly stronger reduction of tumor volume than either BKM120 or LEE011 alone, even though the concentrations of the drugs in the combination group were lowered by half for BKM120 as a single agent, and by two-third for LEE011. These results show that combining BKM120 and LEE011 allows to reduce the drug concentrations while still maintaining the same, or having an even better, effect when compared to the single drugs. This is especially important for possible future treatment of patients with these drugs: the use of lower doses of the drugs should significantly reduce side effects. Furthermore, the tumors in the combination group not only did grow less than the controls, but in some animals there was shrinkage of the tumor volume at the end of the treatment. This is an important parameter for a potential clinical use of these drugs as it would not only stop tumors from growing but would also induce tumor-shrinking and possibly tumor regression.

To conclude, we identified a highly effective and novel treatment approach in PPGLs. The combination of a CDK4/6 and a PI3K/AKT inhibitor has proven to have strong anti-cancer effects against PPGLs and a remarkable synergistic effect *in vivo*. While the combination of inhibitors of these two pathways has been shown to be effective in other tumor types (Malignant pleural mesothelioma and breast cancer [171-174]), to our knowledge this is the first study to show a CDK4/6 and PI3K/AKT inhibition in NETs and especially in PPGLs.

It has been shown that the PI3K/AKT pathway is upregulated in primary human PPGL cell cultures and the upregulation was stronger in cluster 1, SDHB-related samples [143]. SDHB mutations are specific for PPGLs belonging to the pseudohypoxia cluster, which is associated with a more aggressive tumor behavior and poor overall survival [32, 155]. Given the promising results we saw in terms of reducing both tumor growth and aggressive tumor features such as migration and invasion, the combination of CDK4/6 and PI3K/AKT pathway inhibition could be well suited for the treatment of aggressive, cluster 1-related PPGLs. As the cluster 1 cases

are the most aggressive ones, the need to find novel therapeutic strategies is very high. Metastatic cases occur most frequently in cluster 1 patients and our treatment strategy showed great potential in reducing migration and invasion. Furthermore, combining BKM120 and LEE011 not only allows for a dose reduction, potentially reducing the associated side effects, but may also prevent tumor cells from acquiring resistance, which is seen in longer-lasting single drug treatments for both PI3K/mTOR and CDK4/6 inhibitors [32, 117, 175-178].

4.2 PI3K/AKT and CDK4/6 targeted therapy of pNETs

As described above, the PI3K/AKT and the CDK4/6 pathway are two major signaling cascades that are often dysregulated in cancer cells. Literature research and results obtained in previous studies of our group have shown that both pathways are not only changed in PPGLs but also in pNETs. Based on the promising data we have seen for the treatment of PPGLs with BKM120 and LEE011, we set out to investigate whether this treatment approach would also prove effective for pNETs.

To this end, we first treated two pNET cells lines, INS-1E and NT3, with BKM120, LEE011 or their combination and assessed cell proliferation in 2D culture systems. Our data showed that both drugs alone and in combination reduced the proliferation of the two cell lines. In both INS-1E and NT3 cells, the combination showed significantly better results than the single drugs. Interestingly, the proliferation in INS-1E cells was twice as much inhibited as that of NT3 cells over all treatment conditions. The NT3 cell line is one of the only available human pNET lines and displays important characteristics of these tumors such as the expression of multiple NET-specific markers [140]. Therefore, it is better suited as a pNET model than other available cell lines, e.g. BON1 and QGP1 cells, that do not show a high expression of these NET-specific markers [140]. One feature of NT3 cells is their low proliferation rate (they have a doubling time of 11 days), which explains the low reduction in proliferation we observed when we evaluated the drug treatments after 72h. As the assessment of proliferation in the slower-growing pNET cells is not the best readout to evaluate our treatment, we decided to use a 3D cell culture system to assess cell viability and spheroid size after treatment. 3D cell cultures have proven to better recapitulate the involvement of the tumor microenvironment and represent a system between traditional 2D monolayer cell culture and *in vivo* experiments. In both cell lines, we saw a reduction of spheroid cell viability upon treatment. The combination of BKM120 and LEE011 reduced the cell viability significantly more than the single drug treatments, and BKM120 alone worked better than LEE011. This pattern holds true for both cell lines when evaluating mid-ranged drug concentrations up to 5µM BKM120 and 20µM LEE011. Higher drug concentrations lead to a maximum cell viability reduction already in the single drug groups. In INS-1E cells, LEE011 reduced spheroid growth compared to the controls but did not completely inhibit it as spheroids were still growing during 14 days of

treatment. On the other hand, BKM120 and the drug combination completely inhibited spheroid growth over the 14 day drug treatment.

As expected, the size of NT3 spheroids was increasing at a slower rate vs. INS-1E cells, but still showed a 2-3 fold increase after 14 days when compared with the controls. In NT3 cells, LEE011 showed a stronger effect compared to INS-1E cells as it completely inhibited spheroid growth. Interestingly, BKM120 and the combination not only stopped spheroid growth in NT3 cells but additionally elicited a reduction of spheroid size already after three days of treatment. Altogether, our results showed a reduction of both cell proliferation and cell viability in INS-1E and NT3 cells and a beneficial effect of the drug combination. Furthermore, BKM120 as well as the combination, were able to completely inhibit and even reduce the spheroid growth of INS-1E cells and NT3 cells, respectively.

Besides parameters of cell health, we also investigated the induction of apoptosis in pNET cells upon our treatment. We could see the induction of apoptosis with the BKM120 and the combination treatment but not with LEE011. This was expected as previous studies have shown an involvement for the PI3K/AKT pathway in cell death, whereas CDK4/6 is mainly involved in cell cycle progression [149, 150]. In line with this, multiple studies could show apoptosis induction using BKM120, which is not reported for LEE011 [151-154]. A closer look at our results showed significantly more apoptosis induction upon combination treatment compared to BKM120 in NT3 but not in INS-1E cells. This might be due to the fact that NT3 cells carry a homozygous missense mutation of *MEN1*. *MEN1* is a known tumor suppressor and is associated with NET development. It has been shown that in *Men1* deficient mice, CDK4 is required for tumorigenesis [124]. Thus, targeting CDK4 with LEE011 in NT3 cells should be highly effective and could explain the increased apoptosis in the BKM120 + LEE011 treatment compared to BKM120 alone, with LEE011 acting as a sensitizing agent towards the BKM120-mediated apoptosis.

We also set out to see if our treatment would affect migration and invasion in INS-1E and NT3 cells. Unfortunately, both cell clines did not show any potential to migrate or invade in 2D or in 3D systems. Literature research confirmed that no studies exist that show migration or invasion in INS-1E or NT3 cells. NT3 cells originate from a well-differentiated human tumor, which might explain their non-aggressive character [140]. A slow proliferation rate and thereby a non-aggressive nature has also been reported for INS-1 cells [179].

Comparing the results obtained in 2D monolayer cell culture and 3D spheroids, both pNET cell lines showed a similar behavior in terms of migration and invasion. In none of the systems pNET cells were able to migrate or invade. Looking at cell viability and proliferation, a different pattern can be observed. While the drug treatment showed comparable effects using 2D and 3D cell culture in INS-1E cells, it differs in NT3 cells. INS-1E cells show a clear effect of reduced 2D proliferation and 3D viability and a beneficial effect of the combination. In NT3 cells, however, only the 3D spheroids showed a clear difference between treatment groups and a beneficial effect of the drug combination. Since the NT3 cells are slow growing, differences in the metabolic rate are more clearly distinguishable than the cell proliferation assay based on DNA replication. Additionally, cell growth in a spheroid structure can be seen as more *in vivo* like and positively influences long-term cell growth. Therefore, it is best suited for slow-growing cells like NT3s, as seen over the 14 day drug treatment and the corresponding spheroid volumes.

To support our cell line data, we also treated primary cells from *Men1*-deficient mice. The Men1 mouse model is well described and often used in neuroendocrine research as it recapitulates the human MEN1 syndrome phenotype. These mice are heterozygous for *Men1* deficiency and develop multiple NETs, including pNETs. It has been reported that the mouse pNETs resemble the human disease and that most mouse pNETs are insulinomas, arising from the insulin-secreting beta cells of the pancreas [130]. We isolated the pancreatic islets of *Men1* heterozygous knockout and wild-type mice and used them for our treatment studies. As islets, in general, differ in size, we trypsinized the isolated islets to obtain a single-cell solution and then generated spheroids using ULA plates. With this approach, we ensured to have spheroids of the same cell number and size, which is essential to evaluate drug treatment effects on cell growth. In total, we treated primary pNET spheroids of 9 *Men1* heterozygous and 5 wild-type mice. Our results showed that the treatment with LEE011, BKM120 or their combination reduced the cell viability of spheroids obtained from *Men1* heterozygous mice. Comparing the treatments groups, BKM120 combined with LEE011 worked significantly better than the single drug treatments. This is in line with the cell proliferation data on the cell lines, and again shows the beneficial effect of the drug combination. Interestingly, treatment of wild-type spheroids showed a trend for a reduction in cell viability (not significant) when compared to the controls, and no beneficial effect of the combination. Even though the

number of wild-type samples was lower, this data shows that wild-type islets are not as affected by the treatment as islet tumor cells. This proves that not only the combination works better than the single drug treatments but also that our treatment approach is in general highly effective against tumor cells and shows only a very mild effect on wild-type tissue. Especially for *in vivo* studies and potential clinical applications, it is important to find treatment strategies that do not greatly impact non-tumor tissues.

Insulin secretion by the beta-cells is one of the most important pancreatic islet functions. Insulin secretion upon glucose stimulation is essential to maintain glucose homeostasis, a function that is perturbed in patients with diabetes but also in those having pNETs (insulinomas) arising from beta cells. Thus, we evaluated whether the drug treatments affect insulin secretion of both tumor and wild-type beta cells. We generated spheroids from isolated primary cells from *Men1* heterozygous and wild-type mice, and we performed a glucose-stimulated insulin secretion assay on treated and non-treated spheroids.

We found that wild-type islets have a low baseline insulin secretion which is elevated upon glucose stimulation, as expected. In contrast, tumor spheroids had a very high baseline insulin secretion level that did not change following glucose stimulation. Thus, insulin-secretion in *Men1*-deficient pNETs is altered. This is reminiscent of the situation in patients with insulinomas who can also present with high insulin levels and hypoglycemia [180]. Due to the high baseline insulin levels in tumor spheroids, we did not observe an effect of the drug treatments on insulin secretion. The only exception was BKM120 alone, which seems to further increase the baseline insulin secretion of the spheroids. Considering the wild-type spheroids, we could see no effect of the drug treatments on both baseline and stimulated insulin secretion. Based on these results, we can conclude that our treatment does not affect the insulin secretion of normal islets and therefore can be used *in vivo* studies without disturbing the physiological insulin secretion function of the pancreas. In patients with insulinomas, the drug treatment has the potential to suppress tumor growth (and possibly leading to a normalization of insulin secretion) without affecting the functionality of the residual unaffected islets. Interestingly, the combination of BKM120 and LEE011 did not affect insulin secretion in the tumor spheroids and therefore shows a good safety profile regarding insulin secretion. While the combination treatment does not directly affect insulin secretion and therefore cannot immediately address tumor-induced hypoglycemia in insulinoma patients, it reduces pNET cell proliferation and induces apoptosis.

All in all, our novel PI3K/AKT and CDK4/6 treatment strategy for pNETs showed good results *in vitro* by decreasing cell growth and inducing apoptosis. To further evaluate the effectiveness of our treatment, an *in vivo* study using tumor xenografts could give valuable results. In addition to observing the effects of the drugs on the engrafted tumors, this model would also allow monitoring glucose, insulin and other pancreatic hormone levels during treatment. By doing this, not only direct anti-tumor effects but also the effects on pancreatic secretion could be observed. This is relevant for hormonal control in patients as overproduction of pancreatic hormones by the tumor leads to severe side effects like hypoglycemia. Therefore, ensuring that a possible treatment would not further dysregulate these hormone levels is of great importance.

Similar to the situation in PPGLs, to our knowledge, this is the first study combining PI3K and CDK4/6 inhibition in pNETs providing a novel therapeutic option for non-operable cases. Mutations in the PI3K/mTOR pathway have been shown to be a frequent event in pNETs, further supporting the relevance of our therapy approach [57, 181]. Additionally, CDK4/6 inhibition has already shown effectiveness in pNET cells, but it could not prolong progression-free survival when used as a single agent [182]. Therefore, our treatment approach of combining PI3K and CDK4/6 inhibition could help in overcoming current treatment limitations.

4.3 Molecular characterization of PCCs and PGLs in the MENX rat model

As outlined in paragraph 1.2, PCCs develop in the adrenal medulla, whereas PGLs develop in extra-adrenal sympathetic ganglia. Given the fact that both tumor entities arise from chromaffin cells, PCCs and PGLs share many common features and are often grouped together and referred to as PPGLs. Despite their commonalities, these tumors do develop in different locations of the body, and show differences in their genetics and behavior. There is no clear distinction between PCCs and PGLs in terms of treatment. In fact, currently available therapies are mainly established for PCCs and then also used for PGLs. Therefore, it is important to investigate the molecular differences of PCCs and PGLs to eventually achieve a molecular-based personalized therapy approach.

The MENX rat model is a well-established animal model for the study of NETs. Heterozygous mutant MENX rats develop PCCs with full penetrance, and PGLs with a lower penetrance. This gave us the unique opportunity to collect PCCs and PGLs arising in the same animal. Our aim was to investigate the similarities and differences of matched PCCs and PGLs in the MENX model and to compare them to their cognate human tumors. Ultimately, we wanted to determine how different these tumors are in their molecular profile and how well the MENX rat model represents the human disease.

Overall, we collected PCCs and PGLs from eight MENX rats and obtained their gene expression profile. Our results showed that most of the genes dysregulated in tumors vs. wild-type tissues were shared between PCCs and PGLs (3802 genes). Only a lower number of genes was dysregulated only in one of the two tumor types (vs. normal tissue). Specifically, we found 68 genes that were dysregulated in PCCs but not in PGLs, and 293 genes that were dysregulated in PGLs but not in PCCs. Given that both tumor types derive from chromaffin cells and both developed in the same animals, the high number of commonly dysregulated genes is no surprise. Concentrating on the genes that were differentially regulated in PCCs vs. PGLs, a GOBP analysis revealed that these genes are involved in processes associated with the extracellular membrane, motility and oxygen response. Looking at the individual genes, we found that those promoting cell motility, ECM reorganization and ultimately migration and invasion were upregulated in PGLs compared to PCCs. This suggests that MENX PGLs have a signature sug-

gestive of a more aggressive behavior, and this is comparable to the situation in human patients, where PGLs are more often associated to [183]. MENX rats die before developing metastases due to the occurrence of other tumors, e.g. pituitary adenomas. Therefore, it is not possible determine whether metastasis may originate from PCCs or PGLs in this model.

To add another level of information, we set out to compare our rat dataset to a commonly available human dataset of PPGLs. We wanted to compare the global genetic signature and also investigate whether the regulation of single genes would be the same in rats and humans. Comparing the two datasets, we found genes commonly dysregulated between rats and humans. First, we looked at the two tumor entities separately by comparing the dysregulated genes in tumor vs. control in the two species. For PCCs, this analysis showed 359 commonly dysregulated genes in humans and rats, and for PGLs we found 439 genes. This shows that both tumor types share common features in rats and humans. As the aim of our study was to investigate the differences between PCCs and PGLs, we compared the genes dysregulated in PCC vs. PGL in both species and identified 52 differentially expressed genes. Pathway analysis showed that these genes play a role in blood vessel development, cardiovascular system development and aorta morphogenesis, as well as in collagen catabolic processes, extracellular matrix disassembly, collagen fibril organization and cell morphogenesis, implying a different regulation of angiogenesis and migration/invasion. These processes have been extensively associated with a more aggressive behavior in a variety of human cancers [159, 160]. Analyzing the expression of individual genes, we could see that those promoting angiogenesis and ETM transformation were upregulated in rat and human PGLs vs. PCCs. Therefore, we can conclude that PGLs in MENX rats and human patients show a signature comparable with a more aggressive phenotype when compared with PCCs. Additionally, rat and human tumors share the dysregulation of 52 genes that are involved in the above-mentioned disease-promoting processes. Further analysis of these genes can be an important step toward elucidating the molecular mechanisms underlying PGL disease progression and might give new therapeutic targets for a more individualized patient management.

5. References

1. Gore, A.C., *Chapter 38 - Neuroendocrine Systems*, in *Fundamental Neuroscience (Fourth Edition)*, L.R. Squire, et al., Editors. 2013, Academic Press: San Diego. p. 799-817.
2. Klöppel, G., *Neuroendocrine Neoplasms: Dichotomy, Origin and Classifications.* Visceral Medicine, 2017. 33(5): p. 324-330.
3. Rindi, G. and F. Inzani, *Neuroendocrine neoplasm update: toward universal nomenclature.* Endocr Relat Cancer, 2020. 27(6): p. R211-r218.
4. Das, S. and A. Dasari, *Epidemiology, Incidence, and Prevalence of Neuroendocrine Neoplasms: Are There Global Differences?* Curr Oncol Rep, 2021. 23(4): p. 43.
5. Alwan, H., et al., *Incidence trends of lung and gastroenteropancreatic neuroendocrine neoplasms in Switzerland.* Cancer Med, 2020. 9(24): p. 9454-9461.
6. Clift, A.K., et al., *Neuroendocrine Neoplasms of the Small Bowel and Pancreas.* Neuroendocrinology, 2020. 110(6): p. 444-476.
7. Dodic, M., et al., *Effect of steroid hormones on blood pressure.* Clin Exp Pharmacol Physiol, 1999. 26(7): p. 550-2.
8. Barnes, P.J., *Anti-inflammatory actions of glucocorticoids: molecular mechanisms.* Clin Sci (Lond), 1998. 94(6): p. 557-72.
9. Kuo, T., et al., *Regulation of Glucose Homeostasis by Glucocorticoids.* Adv Exp Med Biol, 2015. 872: p. 99-126.
10. Exton, J.H., *Regulation of gluconeogenesis by glucocorticoids.* Monogr Endocrinol, 1979. 12: p. 535-46.
11. Baulieu, E.E., et al., *AN ADRENAL-SECRETED "ANDROGEN": DEHYDROISOANDROSTERONE SULFATE. ITS METABOLISM AND A TENTATIVE GENERALIZATION ON THE METABOLISM OF OTHER STEROID CONJUGATES IN MAN.* Recent Prog Horm Res, 1965. 21: p. 411-500.
12. Smith, M.R., et al., *A radioimmunoassay for the estimation of serum dehydroepiandrosterone sulphate in normal and pathological sera.* Clin Chim Acta, 1975. 65(1): p. 5-13.
13. Vogel, K.S., *Origin of Adrenal Chromaffin Cells from the Neural Crest*, in *Genetic Mechanisms in Multiple Endocrine Neoplasia Type 2*. 1996, Springer Berlin Heidelberg: Berlin, Heidelberg. p. 99-118.
14. Lam, A.K.-y., *Update on Adrenal Tumours in 2017 World Health Organization (WHO) of Endocrine Tumours.* Endocrine Pathology, 2017. 28(3): p. 213-227.
15. Pacak, K. and S. Tella. *Pheochromocytoma and Paraganglioma*. Updated 2018 Jan 4 [cited 2020 05.10.2020]; Available from: https://www.ncbi.nlm.nih.gov/books/NBK481899/.
16. Lenders, J.W.M. and G. Eisenhofer, *Update on Modern Management of Pheochromocytoma and Paraganglioma.* Endocrinol Metab (Seoul), 2017. 32(2): p. 152-161.
17. Patel, D., et al., *Update on Pheochromocytoma and Paraganglioma from the SSO Endocrine/Head and Neck Disease-Site Work Group. Part 1 of 2: Advances in Pathogenesis and Diagnosis of Pheochromocytoma and Paraganglioma.* Annals of Surgical Oncology, 2020. 27(5): p. 1329-1337.
18. Amar, L., et al., *Genetic testing in pheochromocytoma or functional paraganglioma.* J Clin Oncol, 2005. 23(34): p. 8812-8.
19. King, K.S., et al., *Metastatic pheochromocytoma/paraganglioma related to primary tumor development in childhood or adolescence: significant link to SDHB mutations.* J Clin Oncol, 2011. 29(31): p. 4137-42.
20. O'Riordain, D.S., et al., *Clinical spectrum and outcome of functional extraadrenal paraganglioma.* World J Surg, 1996. 20(7): p. 916-21; discussion 922.
21. Crona, J., D. Taïeb, and K. Pacak, *New Perspectives on Pheochromocytoma and Paraganglioma: Toward a Molecular Classification.* Endocr Rev, 2017. 38(6): p. 489-515.

22. Bausch, B., et al., *Long-term prognosis of patients with pediatric pheochromocytoma.* Endocr Relat Cancer, 2014. 21(1): p. 17-25.
23. Goffredo, P., J.A. Sosa, and S.A. Roman, *Malignant pheochromocytoma and paraganglioma: a population level analysis of long-term survival over two decades.* J Surg Oncol, 2013. 107(6): p. 659-64.
24. Turkova, H., et al., *CHARACTERISTICS AND OUTCOMES OF METASTATIC SDHB AND SPORADIC PHEOCHROMOCYTOMA/PARAGANGLIOMA: AN NATIONAL INSTITUTES OF HEALTH STUDY.* Endocr Pract, 2016. 22(3): p. 302-14.
25. Lenders, J.W., et al., *Pheochromocytoma and paraganglioma: an endocrine society clinical practice guideline.* J Clin Endocrinol Metab, 2014. 99(6): p. 1915-42.
26. Björklund, P., K. Pacak, and J. Crona, *Precision medicine in pheochromocytoma and paraganglioma: current and future concepts.* J Intern Med, 2016. 280(6): p. 559-573.
27. La Salvia, A., et al., *Targeted Cancer Therapy: What's New in the Field of Neuroendocrine Neoplasms?* Cancers (Basel), 2021. 13(7).
28. Patel, M., et al., *Somatostatin Receptors and Analogs in Pheochromocytoma and Paraganglioma: Old Players in a New Precision Medicine World.* Front Endocrinol (Lausanne), 2021. 12: p. 625312.
29. Eisenhofer, G., et al., *Pheochromocytoma catecholamine phenotypes and prediction of tumor size and location by use of plasma free metanephrines.* Clin Chem, 2005. 51(4): p. 735-44.
30. Pamporaki, C., et al., *Characteristics of Pediatric vs Adult Pheochromocytomas and Paragangliomas.* J Clin Endocrinol Metab, 2017. 102(4): p. 1122-1132.
31. Favier, J., L. Amar, and A.P. Gimenez-Roqueplo, *Paraganglioma and phaeochromocytoma: from genetics to personalized medicine.* Nat Rev Endocrinol, 2015. 11(2): p. 101-11.
32. Fishbein, L., et al., *Comprehensive Molecular Characterization of Pheochromocytoma and Paraganglioma.* Cancer Cell, 2017. 31(2): p. 181-193.
33. Astuti, D., et al., *Gene mutations in the succinate dehydrogenase subunit SDHB cause susceptibility to familial pheochromocytoma and to familial paraganglioma.* Am J Hum Genet, 2001. 69(1): p. 49-54.
34. Baysal, B.E., et al., *Mutations in SDHD, a mitochondrial complex II gene, in hereditary paraganglioma.* Science, 2000. 287(5454): p. 848-51.
35. Burnichon, N., et al., *SDHA is a tumor suppressor gene causing paraganglioma.* Hum Mol Genet, 2010. 19(15): p. 3011-20.
36. Hao, H.X., et al., *SDH5, a gene required for flavination of succinate dehydrogenase, is mutated in paraganglioma.* Science, 2009. 325(5944): p. 1139-42.
37. Letouzé, E., et al., *SDH mutations establish a hypermethylator phenotype in paraganglioma.* Cancer Cell, 2013. 23(6): p. 739-52.
38. Niemann, S. and U. Müller, *Mutations in SDHC cause autosomal dominant paraganglioma, type 3.* Nat Genet, 2000. 26(3): p. 268-70.
39. Fliedner, S.M., et al., *Hypoxia-Inducible Factor 2α Mutation-Related Paragangliomas Classify as Discrete Pseudohypoxic Subcluster.* Neoplasia, 2016. 18(9): p. 567-76.
40. Hes, F.J., et al., *Frequency of Von Hippel-Lindau germline mutations in classic and non-classic Von Hippel-Lindau disease identified by DNA sequencing, Southern blot analysis and multiplex ligation-dependent probe amplification.* Clin Genet, 2007. 72(2): p. 122-9.
41. Jochmanová, I., et al., *Hypoxia-inducible factor signaling in pheochromocytoma: turning the rudder in the right direction.* J Natl Cancer Inst, 2013. 105(17): p. 1270-83.
42. Latif, F., et al., *Identification of the von Hippel-Lindau disease tumor suppressor gene.* Science, 1993. 260(5112): p. 1317-20.
43. Pacak, K., et al., *New syndrome of paraganglioma and somatostatinoma associated with polycythemia.* J Clin Oncol, 2013. 31(13): p. 1690-8.
44. Zhuang, Z., et al., *Somatic HIF2A gain-of-function mutations in paraganglioma with polycythemia.* N Engl J Med, 2012. 367(10): p. 922-30.

45. Burnichon, N., et al., *Integrative genomic analysis reveals somatic mutations in pheochromocytoma and paraganglioma.* Hum Mol Genet, 2011. 20(20): p. 3974-85.
46. Castro-Vega, L.J., et al., *Multi-omics analysis defines core genomic alterations in pheochromocytomas and paragangliomas.* Nat Commun, 2015. 6: p. 6044.
47. Schlisio, S., et al., *The kinesin KIF1Bbeta acts downstream from EglN3 to induce apoptosis and is a potential 1p36 tumor suppressor.* Genes Dev, 2008. 22(7): p. 884-93.
48. Toledo, R.A., et al., *Recurrent Mutations of Chromatin-Remodeling Genes and Kinase Receptors in Pheochromocytomas and Paragangliomas.* Clin Cancer Res, 2016. 22(9): p. 2301-10.
49. Welander, J., et al., *Rare germline mutations identified by targeted next-generation sequencing of susceptibility genes in pheochromocytoma and paraganglioma.* J Clin Endocrinol Metab, 2014. 99(7): p. E1352-60.
50. Halfdanarson, T.R., et al., *Pancreatic neuroendocrine tumors (PNETs): incidence, prognosis and recent trend toward improved survival.* Ann Oncol, 2008. 19(10): p. 1727-33.
51. Ohmoto, A., H. Rokutan, and S. Yachida, *Pancreatic Neuroendocrine Neoplasms: Basic Biology, Current Treatment Strategies and Prospects for the Future.* Int J Mol Sci, 2017. 18(1).
52. Yao, J.C., et al., *Population-based study of islet cell carcinoma.* Ann Surg Oncol, 2007. 14(12): p. 3492-500.
53. Yao, J.C., et al., *One hundred years after "carcinoid": epidemiology of and prognostic factors for neuroendocrine tumors in 35,825 cases in the United States.* J Clin Oncol, 2008. 26(18): p. 3063-72.
54. Ehehalt, F., et al., *Neuroendocrine tumors of the pancreas.* Oncologist, 2009. 14(5): p. 456-67.
55. Cives, M. and J.R. Strosberg, *Gastroenteropancreatic Neuroendocrine Tumors.* CA Cancer J Clin, 2018. 68(6): p. 471-487.
56. Gorelik, M., et al., *Nonfunctioning Incidental Pancreatic Neuroendocrine Tumors: Who, When, and How to Treat?* Surg Clin North Am, 2018. 98(1): p. 157-167.
57. Jiao, Y., et al., *DAXX/ATRX, MEN1, and mTOR pathway genes are frequently altered in pancreatic neuroendocrine tumors.* Science, 2011. 331(6021): p. 1199-203.
58. Partelli, S., et al., *ENETS Consensus Guidelines for Standard of Care in Neuroendocrine Tumours: Surgery for Small Intestinal and Pancreatic Neuroendocrine Tumours.* Neuroendocrinology, 2017. 105(3): p. 255-265.
59. Fendrich, V., et al., *An aggressive surgical approach leads to long-term survival in patients with pancreatic endocrine tumors.* Ann Surg, 2006. 244(6): p. 845-51; discussion 852-3.
60. Chandrasekharappa, S.C., et al., *Positional cloning of the gene for multiple endocrine neoplasia-type 1.* Science, 1997. 276(5311): p. 404-7.
61. Kamilaris, C.D.C. and C.A. Stratakis, *Multiple Endocrine Neoplasia Type 1 (MEN1): An Update and the Significance of Early Genetic and Clinical Diagnosis.* Front Endocrinol (Lausanne), 2019. 10: p. 339.
62. Lemmens, I., et al., *Identification of the multiple endocrine neoplasia type 1 (MEN1) gene. The European Consortium on MEN1.* Hum Mol Genet, 1997. 6(7): p. 1177-83.
63. Heppner, C., et al., *The tumor suppressor protein menin interacts with NF-κB proteins and inhibits NF-κB-mediated transactivation.* Oncogene, 2001. 20(36): p. 4917-4925.
64. Hughes, C.M., et al., *Menin associates with a trithorax family histone methyltransferase complex and with the hoxc8 locus.* Mol Cell, 2004. 13(4): p. 587-97.
65. Jin, S., et al., *Menin associates with FANCD2, a protein involved in repair of DNA damage.* Cancer Res, 2003. 63(14): p. 4204-10.
66. Kaji, H., et al., *Inactivation of menin, a Smad3-interacting protein, blocks transforming growth factor type beta signaling.* Proc Natl Acad Sci U S A, 2001. 98(7): p. 3837-42.
67. Lin, S.Y. and S.J. Elledge, *Multiple tumor suppressor pathways negatively regulate telomerase.* Cell, 2003. 113(7): p. 881-9.

68. Mulligan, L.M., et al., *Genetic events in tumour initiation and progression in multiple endocrine neoplasia type 2.* Genes Chromosomes Cancer, 1993. 6(3): p. 166-77.
69. Sizemore, G.W., H. Health, 3rd, and J.A. Carney, *Multiple endocrine neoplasia type 2.* Clin Endocrinol Metab, 1980. 9(2): p. 299-315.
70. Norton, J.A., G. Krampitz, and R.T. Jensen, *Multiple Endocrine Neoplasia: Genetics and Clinical Management.* Surg Oncol Clin N Am, 2015. 24(4): p. 795-832.
71. Moline, J. and C. Eng, *Multiple endocrine neoplasia type 2: an overview.* Genet Med, 2011. 13(9): p. 755-64.
72. Norton, J.A., et al., *Multiple endocrine neoplasia type IIb: the most aggressive form of medullary thyroid carcinoma.* Surg Clin North Am, 1979. 59(1): p. 109-18.
73. Pellegata, N.S., et al., *Germ-line mutations in p27^{Kip1} cause a multiple endocrine neoplasia syndrome in rats and humans.* Proceedings of the National Academy of Sciences, 2006. 103(42): p. 15558-15563.
74. Lee, M. and N.S. Pellegata, *Multiple endocrine neoplasia type 4.* Front Horm Res, 2013. 41: p. 63-78.
75. Pardi, E., et al., *Functional characterization of a CDKN1B mutation in a Sardinian kindred with multiple endocrine neoplasia type 4 (MEN4).* Endocr Connect, 2015. 4(1): p. 1-8.
76. Marinoni, I. and N.S. Pellegata, *p27kip1: a new multiple endocrine neoplasia gene?* Neuroendocrinology, 2011. 93(1): p. 19-28.
77. Fero, M.L., et al., *The murine gene p27Kip1 is haplo-insufficient for tumour suppression.* Nature, 1998. 396(6707): p. 177-80.
78. Georgitsi, M., *MEN-4 and other multiple endocrine neoplasias due to cyclin-dependent kinase inhibitors (p27(Kip1) and p18(INK4C)) mutations.* Best Pract Res Clin Endocrinol Metab, 2010. 24(3): p. 425-37.
79. Alrezk, R., F. Hannah-Shmouni, and C.A. Stratakis, *MEN4 and CDKN1B mutations: the latest of the MEN syndromes.* Endocr Relat Cancer, 2017. 24(10): p. T195-t208.
80. Jiang, N., et al., *Role of PI3K/AKT pathway in cancer: the framework of malignant behavior.* Molecular Biology Reports, 2020. 47(6): p. 4587-4629.
81. Cantley, L.C., *The phosphoinositide 3-kinase pathway.* Science, 2002. 296(5573): p. 1655-7.
82. Yuan, T.L. and L.C. Cantley, *PI3K pathway alterations in cancer: variations on a theme.* Oncogene, 2008. 27(41): p. 5497-510.
83. Zhang, M., H. Jang, and R. Nussinov, *PI3K inhibitors: review and new strategies.* Chem Sci, 2020. 11(23): p. 5855-5865.
84. Liu, R., et al., *PI3K/AKT pathway as a key link modulates the multidrug resistance of cancers.* Cell Death Dis, 2020. 11(9): p. 797.
85. Leslie, Nick R., et al., *The PTEN protein: cellular localization and post-translational regulation.* Biochemical Society Transactions, 2016. 44(1): p. 273-278.
86. Chow, J.T. and L. Salmena, *Recent advances in PTEN signalling axes in cancer.* Fac Rev, 2020. 9: p. 31.
87. Czech, M.P., *PIP2 and PIP3: complex roles at the cell surface.* Cell, 2000. 100(6): p. 603-6.
88. Arcaro, A. and A.S. Guerreiro, *The phosphoinositide 3-kinase pathway in human cancer: genetic alterations and therapeutic implications.* Curr Genomics, 2007. 8(5): p. 271-306.
89. Hers, I., E.E. Vincent, and J.M. Tavaré, *Akt signalling in health and disease.* Cell Signal, 2011. 23(10): p. 1515-27.
90. Carnero, A., et al., *The PTEN/PI3K/AKT signalling pathway in cancer, therapeutic implications.* Curr Cancer Drug Targets, 2008. 8(3): p. 187-98.
91. Kashiwada, M., P. Lu, and P.B. Rothman, *PIP3 pathway in regulatory T cells and autoimmunity.* Immunologic Research, 2007. 39(1): p. 194.
92. Burger, M.T., et al., *Identification of NVP-BKM120 as a Potent, Selective, Orally Bioavailable Class I PI3 Kinase Inhibitor for Treating Cancer.* ACS Med Chem Lett, 2011. 2(10): p. 774-9.

93. Alvarez-Tejado, M., et al., *Hypoxia induces the activation of the phosphatidylinositol 3-kinase/Akt cell survival pathway in PC12 cells: protective role in apoptosis.* J Biol Chem, 2001. 276(25): p. 22368-74.
94. Adler, J.T., et al., *Inhibition of the PI3K Pathway Suppresses Hormonal Secretion and Limits Growth in Pheochromocytoma Cells.* World Journal of Surgery, 2009. 33(11): p. 2452.
95. Fassnacht, M., et al., *AKT Is Highly Phosphorylated in Pheochromocytomas But Not in Benign Adrenocortical Tumors.* The Journal of Clinical Endocrinology & Metabolism, 2005. 90(7): p. 4366-4370.
96. Fritz, A., et al., *Recessive Transmission of a Multiple Endocrine Neoplasia Syndrome in the Rat.* Cancer Research, 2002. 62(11): p. 3048-3051.
97. Pellegata, N.S., et al., *Human pheochromocytomas show reduced p27Kip1 expression that is not associated with somatic gene mutations and rarely with deletions.* Virchows Archiv, 2007. 451(1): p. 37-46.
98. Robbins, H.L. and A. Hague, *The PI3K/Akt Pathway in Tumors of Endocrine Tissues.* Front Endocrinol (Lausanne), 2015. 6: p. 188.
99. Fankhauser, M., et al., *Synergistic Highly Potent Targeted Drug Combinations in Different Pheochromocytoma Models Including Human Tumor Cultures.* Endocrinology, 2019. 160(11): p. 2600-2617.
100. Perren, A., et al., *Mutation and expression analyses reveal differential subcellular compartmentalization of PTEN in endocrine pancreatic tumors compared to normal islet cells.* Am J Pathol, 2000. 157(4): p. 1097-103.
101. Missiaglia, E., et al., *Pancreatic Endocrine Tumors: Expression Profiling Evidences a Role for AKT-mTOR Pathway.* Journal of Clinical Oncology, 2010. 28(2): p. 245-255.
102. François, R.A., et al., *Targeting Focal Adhesion Kinase and Resistance to mTOR Inhibition in Pancreatic Neuroendocrine Tumors.* J Natl Cancer Inst, 2015. 107(8).
103. Ghayouri, M., et al., *Activation of the serine/theronine protein kinase Akt in enteropancreatic neuroendocrine tumors.* Anticancer Res, 2010. 30(12): p. 5063-7.
104. Yao, J.C., et al., *Everolimus for Advanced Pancreatic Neuroendocrine Tumors.* New England Journal of Medicine, 2011. 364(6): p. 514-523.
105. Wolin, E.M., *PI3K/Akt/mTOR pathway inhibitors in the therapy of pancreatic neuroendocrine tumors.* Cancer Letters, 2013. 335(1): p. 1-8.
106. Lamberti, G., et al., *The Role of mTOR in Neuroendocrine Tumors: Future Cornerstone of a Winning Strategy?* Int J Mol Sci, 2018. 19(3).
107. Knudsen, E.S., et al., *Cell Cycle and Beyond: Exploiting New RB1 Controlled Mechanisms for Cancer Therapy.* Trends Cancer, 2019. 5(5): p. 308-324.
108. Presti, D. and E. Quaquarini, *The PI3K/AKT/mTOR and CDK4/6 Pathways in Endocrine Resistant HR+/HER2- Metastatic Breast Cancer: Biological Mechanisms and New Treatments.* Cancers (Basel), 2019. 11(9).
109. Piezzo, M., et al., *Targeting Cell Cycle in Breast Cancer: CDK4/6 Inhibitors.* Int J Mol Sci, 2020. 21(18).
110. Ren, B., et al., *E2F integrates cell cycle progression with DNA repair, replication, and G(2)/M checkpoints.* Genes Dev, 2002. 16(2): p. 245-56.
111. Burkhart, D.L. and J. Sage, *Cellular mechanisms of tumour suppression by the retinoblastoma gene.* Nat Rev Cancer, 2008. 8(9): p. 671-82.
112. Johnson, J., et al., *Targeting the RB-E2F pathway in breast cancer.* Oncogene, 2016. 35(37): p. 4829-35.
113. de Groot, A.F., C.J. Kuijpers, and J.R. Kroep, *CDK4/6 inhibition in early and metastatic breast cancer: A review.* Cancer Treat Rev, 2017. 60: p. 130-138.
114. Raj, N., et al., *Ribociclib and everolimus in well-differentiated foregut neuroendocrine tumors.* Endocr Relat Cancer, 2021. 28(4): p. 237-246.

115. van Caloen, G., et al., *Preclinical Evaluation of the Association of the Cyclin-Dependent Kinase 4/6 Inhibitor, Ribociclib, and Cetuximab in Squamous Cell Carcinoma of the Head and Neck.* Cancers (Basel), 2021. 13(6).
116. Jin, X.F., et al., *Antitumoral Activity of the MEK Inhibitor Trametinib (TMT212) Alone and in Combination with the CDK4/6 Inhibitor Ribociclib (LEE011) in Neuroendocrine Tumor Cells In Vitro.* Cancers (Basel), 2021. 13(6).
117. Sobhani, N., et al., *Targeting Aberrant FGFR Signaling to Overcome CDK4/6 Inhibitor Resistance in Breast Cancer.* Cells, 2021. 10(2).
118. Shi, Y., et al., *Cell Cycle Protein Expression in Neuroendocrine Tumors: Association of CDK4/CDK6, CCND1, and Phosphorylated Retinoblastoma Protein With Proliferative Index.* Pancreas, 2017. 46(10): p. 1347-1353.
119. Du, Q., et al., *The application and prospect of CDK4/6 inhibitors in malignant solid tumors.* Journal of Hematology & Oncology, 2020. 13(1): p. 41.
120. Chando, R.K., et al., *CDK4 as a phytochemical based anticancer drug target.* bioRxiv, 2019: p. 859595.
121. Pellegata, N.S., *MENX and MEN4.* Clinics (Sao Paulo), 2012. 67 Suppl 1(Suppl 1): p. 13-8.
122. Tang, L.H., et al., *Attenuation of the Retinoblastoma Pathway in Pancreatic Neuroendocrine Tumors Due to Increased Cdk4/Cdk6.* Clinical Cancer Research, 2012. 18(17): p. 4612-4620.
123. Wiedemann, T., et al., *Obesity in MENX Rats Is Accompanied by High Circulating Levels of Ghrelin and Improved Insulin Sensitivity.* Diabetes, 2016. 65(2): p. 406-20.
124. Gillam, M.P., et al., *MEN1 tumorigenesis in the pituitary and pancreatic islet requires Cdk4 but not Cdk2.* Oncogene, 2015. 34(7): p. 932-8.
125. Molatore, S., et al., *Characterization of a naturally-occurring p27 mutation predisposing to multiple endocrine tumors.* Molecular Cancer, 2010. 9: p. 116.
126. Molatore, S., et al., *Characterization of neuroendocrine tumors in heterozygous mutant MENX rats: a novel model of invasive medullary thyroid carcinoma.* Endocr Relat Cancer, 2018. 25(2): p. 145-162.
127. Lee, M., et al., *Levels of p27 sensitize to dual PI3K/mTOR inhibition.* Mol Cancer Ther, 2011. 10(8): p. 1450-9.
128. Lee, M., et al., *Secretin receptor promotes the proliferation of endocrine tumor cells via the PI3K/AKT pathway.* Mol Endocrinol, 2012. 26(8): p. 1394-405.
129. Leinhäuser, I., et al., *Oncogenic features of the bone morphogenic protein 7 (BMP7) in pheochromocytoma.* Oncotarget, 2015. 6(36).
130. Bertolino, P., et al., *Heterozygous Men1 mutant mice develop a range of endocrine tumors mimicking multiple endocrine neoplasia type 1.* Mol Endocrinol, 2003. 17(9): p. 1880-92.
131. Bertolino, P., et al., *Genetic ablation of the tumor suppressor menin causes lethality at mid-gestation with defects in multiple organs.* Mech Dev, 2003. 120(5): p. 549-60.
132. Aygun, N. and M. Uludag, *Pheochromocytoma and Paraganglioma: From Treatment to Follow-up.* Sisli Etfal Hastan Tip Bul, 2020. 54(4): p. 391-398.
133. Granberg, D., C.C. Juhlin, and H. Falhammar, *Metastatic Pheochromocytomas and Abdominal Paragangliomas.* J Clin Endocrinol Metab, 2021. 106(5): p. e1937-e1952.
134. Wei, M., et al., *From the Immune Profile to the Immunoscore: Signatures for Improving Postsurgical Prognostic Prediction of Pancreatic Neuroendocrine Tumors.* Front Immunol, 2021. 12: p. 654660.
135. Calissendorff, J., et al., *Characteristics, Treatment, Outcomes, and Survival in Neuroendocrine G1 and G2 Pancreatic Tumors: Experiences From a Single Tertiary Referral Center.* Front Endocrinol (Lausanne), 2021. 12: p. 657698.
136. Tomayko, M.M. and C.P. Reynolds, *Determination of subcutaneous tumor size in athymic (nude) mice.* Cancer Chemother Pharmacol, 1989. 24(3): p. 148-54.
137. Euhus, D.M., et al., *Tumor measurement in the nude mouse.* J Surg Oncol, 1986. 31(4): p. 229-34.

138. Raemaekers, T., et al., *NuSAP, a novel microtubule-associated protein involved in mitotic spindle organization.* J Cell Biol, 2003. 162(6): p. 1017-29.
139. Lee, M., et al., *Transcriptome analysis of MENX-associated rat pituitary adenomas identifies novel molecular mechanisms involved in the pathogenesis of human pituitary gonadotroph adenomas.* Acta Neuropathol, 2013. 126(1): p. 137-50.
140. Benten, D., et al., *Establishment of the First Well-differentiated Human Pancreatic Neuroendocrine Tumor Model.* Mol Cancer Res, 2018. 16(3): p. 496-507.
141. Molatore, S., et al., *Pheochromocytoma in rats with multiple endocrine neoplasia (MENX) shares gene expression patterns with human pheochromocytoma.* Proc Natl Acad Sci U S A, 2010. 107(43): p. 18493-8.
142. Bayat Mokhtari, R., et al., *Combination therapy in combating cancer.* Oncotarget, 2017. 8(23): p. 38022-38043.
143. Du, J., et al., *The Roles of PI3K/AKT/mTOR and MAPK/ERK Signaling Pathways in Human Pheochromocytomas.* Int J Endocrinol, 2016. 2016: p. 5286972.
144. Lee, M., et al., *Targeting PI3K/mTOR signaling exerts potent antitumor activity in pheochromocytoma in vivo.* Endocr Relat Cancer, 2017. 24(1): p. 1-15.
145. Aristizabal Prada, E.T., et al., *The Novel Cyclin-Dependent Kinase 4/6 Inhibitor Ribociclib (LEE011) Alone and in Dual-Targeting Approaches Demonstrates Antitumoral Efficacy in Neuroendocrine Tumors in vitro.* Neuroendocrinology, 2018. 106(1): p. 58-73.
146. Chou, T.-C., *Drug Combination Studies and Their Synergy Quantification Using the Chou-Talalay Method.* Cancer Research, 2010. 70(2): p. 440-446.
147. Chou, T.-C., *The combination index (CI < 1) as the definition of synergism and of synergy claims.* Synergy, 2018. 7: p. 49-50.
148. Chou, T.C. and P. Talalay, *Quantitative analysis of dose-effect relationships: the combined effects of multiple drugs or enzyme inhibitors.* Adv Enzyme Regul, 1984. 22: p. 27-55.
149. Zhou, H., et al., *Akt regulates cell survival and apoptosis at a postmitochondrial level.* J Cell Biol, 2000. 151(3): p. 483-94.
150. Baker, S.J. and E.P. Reddy, *CDK4: A Key Player in the Cell Cycle, Development, and Cancer.* Genes Cancer, 2012. 3(11-12): p. 658-69.
151. Anisuzzaman, A.S.M., et al., *In Vitro and In Vivo Synergistic Antitumor Activity of the Combination of BKM120 and Erlotinib in Head and Neck Cancer: Mechanism of Apoptosis and Resistance.* Molecular Cancer Therapeutics, 2017. 16(4): p. 729-738.
152. Sadeghi, S., et al., *PI3K Abrogation Using Pan-PI3K Inhibitor BKM120 Gives Rise to a Significant Anticancer Effect on AML-Derived KG-1 Cells by Inducing Apoptosis and G2/M Arrest.* Turk J Haematol, 2020. 37(3): p. 167-176.
153. Bashash, D., et al., *Inhibition of PI3K signaling pathway enhances the chemosensitivity of APL cells to ATO: Proposing novel therapeutic potential for BKM120.* Eur J Pharmacol, 2018. 841: p. 10-18.
154. Yuan, Y., et al., *Combination therapy with BYL719 and LEE011 is synergistic and causes a greater suppression of p-S6 in triple negative breast cancer.* Sci Rep, 2019. 9(1): p. 7509.
155. Choi, Y.M., et al., *Mutation Profile of Aggressive Pheochromocytoma and Paraganglioma with Comparison of TCGA Data.* Cancers (Basel), 2021. 13(10).
156. Bayley, J.-P. and P. Devilee, *Advances in paraganglioma–pheochromocytoma cell lines and xenografts.* Endocrine-Related Cancer, 2020. 27(12): p. R433-R450.
157. Powers, J.F., et al., *Pheochromocytoma cell lines from heterozygous neurofibromatosis knockout mice.* Cell Tissue Res, 2000. 302(3): p. 309-20.
158. Bechmann, N., et al., *Impact of Extrinsic and Intrinsic Hypoxia on Catecholamine Biosynthesis in Absence or Presence of Hif2α in Pheochromocytoma Cells.* Cancers (Basel), 2019. 11(5).
159. Hanahan, D. and R.A. Weinberg, *Hallmarks of cancer: the next generation.* Cell, 2011. 144(5): p. 646-74.

160. Hanahan, D. and R.A. Weinberg, *The hallmarks of cancer.* Cell, 2000. 100(1): p. 57-70.
161. Imamura, Y., et al., *Comparison of 2D- and 3D-culture models as drug-testing platforms in breast cancer.* Oncol Rep, 2015. 33(4): p. 1837-1843.
162. Breslin, S. and L. O'Driscoll, *The relevance of using 3D cell cultures, in addition to 2D monolayer cultures, when evaluating breast cancer drug sensitivity and resistance.* Oncotarget, 2016. 7(29): p. 45745-45756.
163. de la Puente, P., et al., *3D tissue-engineered bone marrow as a novel model to study pathophysiology and drug resistance in multiple myeloma.* Biomaterials, 2015. 73: p. 70-84.
164. Lovitt, C.J., T.B. Shelper, and V.M. Avery, *Evaluation of chemotherapeutics in a three-dimensional breast cancer model.* J Cancer Res Clin Oncol, 2015. 141(5): p. 951-9.
165. Melissaridou, S., et al., *The effect of 2D and 3D cell cultures on treatment response, EMT profile and stem cell features in head and neck cancer.* Cancer Cell International, 2019. 19(1): p. 16.
166. Jensen, C. and Y. Teng, *Is It Time to Start Transitioning From 2D to 3D Cell Culture?* Frontiers in Molecular Biosciences, 2020. 7(33).
167. Ullrich, M., et al., *Targeting Cyclooxygenase-2 in Pheochromocytoma and Paraganglioma: Focus on Genetic Background.* Cancers (Basel), 2019. 11(6).
168. Chang, F., et al., *Signal transduction mediated by the Ras/Raf/MEK/ERK pathway from cytokine receptors to transcription factors: potential targeting for therapeutic intervention.* Leukemia, 2003. 17(7): p. 1263-1293.
169. Dienstmann, R., et al., *Picking the Point of Inhibition: A Comparative Review of PI3K/AKT/mTOR Pathway Inhibitors.* Molecular Cancer Therapeutics, 2014. 13(5): p. 1021-1031.
170. Mohr, H., et al., *Mutation of the Cell Cycle Regulator p27kip1 Drives Pseudohypoxic Pheochromocytoma Development.* Cancers (Basel), 2021. 13(1).
171. Bonelli, M., et al., *Dual Inhibition of CDK4/6 and PI3K/AKT/mTOR Signaling Impairs Energy Metabolism in MPM Cancer Cells.* Int J Mol Sci, 2020. 21(14).
172. Gul, A., et al., *A combination of the PI3K pathway inhibitor plus cell cycle pathway inhibitor to combat endocrine resistance in hormone receptor-positive breast cancer: a genomic algorithm-based treatment approach.* Am J Cancer Res, 2018. 8(12): p. 2359-2376.
173. Muranen, T., F. Meric-Bernstam, and G.B. Mills, *Promising rationally derived combination therapy with PI3K and CDK4/6 inhibitors.* Cancer Cell, 2014. 26(1): p. 7-9.
174. Teo, Z.L., et al., *Combined CDK4/6 and PI3Kα Inhibition Is Synergistic and Immunogenic in Triple-Negative Breast Cancer.* Cancer Res, 2017. 77(22): p. 6340-6352.
175. Vandamme, T., et al., *Long-term acquired everolimus resistance in pancreatic neuroendocrine tumours can be overcome with novel PI3K-AKT-mTOR inhibitors.* Br J Cancer, 2016. 114(6): p. 650-8.
176. Fazio, N., et al., *A Phase II Study of BEZ235 in Patients with Everolimus-resistant, Advanced Pancreatic Neuroendocrine Tumours.* Anticancer Res, 2016. 36(2): p. 713-9.
177. Passacantilli, I., et al., *Combined therapy with RAD001 e BEZ235 overcomes resistance of PET immortalized cell lines to mTOR inhibition.* Oncotarget, 2014. 5(14): p. 5381-91.
178. Liu, Z., et al., *[CDK4/6 signaling pathway and its targeted therapeutic agents in cancer therapy: a review].* Sheng Wu Gong Cheng Xue Bao, 2021. 37(7): p. 2232-2239.
179. Asfari, M., et al., *Establishment of 2-mercaptoethanol-dependent differentiated insulin-secreting cell lines.* Endocrinology, 1992. 130(1): p. 167-78.
180. Okabayashi, T., et al., *Diagnosis and management of insulinoma.* World J Gastroenterol, 2013. 19(6): p. 829-37.
181. Pipinikas, C.P., et al., *The evolving (epi)genetic landscape of pancreatic neuroendocrine tumours.* Endocrine-Related Cancer, 2019. 26(9): p. R519-R544.

182. Shaik Amjad US, K.C., Maharjan CK, *Efficacy of combined MEK and CDK targeted therapies for pancreatic neuroendocrine tumors*, in *North American Neuroendocrine Tumor Society 2020 Annual Symposium*.
183. Fliedner, S.M., H. Lehnert, and K. Pacak, *Metastatic paraganglioma.* Semin Oncol, 2010. 37(6): p. 627-37.

Publications

Gulde, S.*, T. Wiedemann*, M. Schillmaier, I. Valença, A. Lupp, K. Steiger, H. Y. Yen, S. Bäuerle, J. Notni, R. Luque, H. Schmid, S. Schulz, D. P. Ankerst, F. Schilling and N. S. Pellegata (2021). "Gender-Specific Efficacy Revealed by Head-to-Head Comparison of Pasireotide and Octreotide in a Representative In Vivo Model of Nonfunctioning Pituitary Tumors." Cancers (Basel) 13(12).

Mohr, H., S. Ballke, N. Bechmann, **S. Gulde**, J. Malekzadeh-Najafabadi, M. Peitzsch, V. Ntziachristos, K. Steiger, T. Wiedemann and N. S. Pellegata (2021). "Mutation of the Cell Cycle Regulator p27kip1 Drives Pseudohypoxic Pheochromocytoma Development." Cancers (Basel) 13(1).

Bogner, E. M., A. F. Daly, **S. Gulde**, A. Karhu, M. Irmler, J. Beckers, H. Mohr, A. Beckers and N. S. Pellegata (2020). "miR-34a is upregulated in AIP-mutated somatotropinomas and promotes octreotide resistance." Int J Cancer 147(12): 3523-3538.

Gigantism and Acromegaly, 1st Edition; Editor: Constantine Stratakis; CHAPTER 8 CDKN1B (p27) defects leading to pituitary tumors, **Sebastian Gulde** and Natalia S. Pellegata; Imprint: Academic Press; Published Date: 1st June 2021; Paperback ISBN: 9780128145371; eBook ISBN: 9780128145388

Manuscript including data from Chapter 3.1 *Molecular based therapy of PPGLs by targeting PI3K and CDK4/6* and manuscript including data from Chapter 3.2 *Molecular based therapy of pNETs by targeting PI3K and CDK4/6* are in preparation.